Skolkovo Institute of Science and Technology

MULTIFUNCTIONAL INTERLEAVES FOR COMPOSITE LAMINATE

Doctoral Thesis

by
BILTU MAHATO

DOCTORAL PROGRAM IN MATHEMATICS AND MECHANICS

Supervisor
Dr. Sergey G. Abaimov

Co-supervisor
Prof. Stepan V. Lomov

Moscow - 2023

I hereby declare that the work presented in this thesis was carried out by myself at Skolkovo Institute of Science and Technology, Moscow, except where due acknowledgment is made and has not been submitted for any other degree.

Candidate (Biltu Mahato)
Supervisor (Dr. Sergey G. Abaimov)
Co-supervisor (Prof. Stepan V. Lomov)

Abstract

Fiber-reinforced polymer (FRP) composites are widely used in various applications because of their high in-plane properties. However, they suffer from poor out-of-plane properties, leading to failure of composite laminate by delamination. To address the problem of delamination, several methods at the micro- and nano-level are suggested; however, they come at the cost of compromise in the in-plane properties, increased complexity, or cost.

In this research, we propose an interlaminar region modification method that would not only improve the out-of-plane property like fracture toughness but also make the composite laminate electrically conductive, such that it can further serve as a toughening phase as well as provide the possibility of structural health monitoring. Such laminates are known as multifunctional laminates. With this goal, the first modification method was interleaving the polymeric veil produced by the electrospinning of polymers. Usually, these polymeric veils are electrically insulative, so multi-walled carbon nanotubes (MWCNTs) were added. Polyacrylonitrile (PAN) with up to 5 wt% of MWCNTs polymeric veils was successfully manufactured however, the electrical conductivity was not achieved because of the absence of a percolation network within the nanofibers or amongst the nanofibers of PAN veil.

This was followed by the production of single-walled carbon nanotubes (SWCNTs) interleave produced by diluting the industrially available masterbatch. Two interleaves containing 0.6 wt% and 7.5 wt% of SWCNTs were produced and interleaved in the composite laminate. The 0.6 wt% interleaved laminate shows a ~80% drop in Mode I fracture toughness because the interleave was rich in epoxy, which debonded earlier blocking the prevalent fiber bridging. However, the 7.5 wt% interleaved laminate shows a 27% improvement in initiation and unchanged propagation energy. The fracture toughness was improved because of the introduction of a hierarchical toughening mechanism by the SWCNTs along with

the fiber bridging noted in the baseline laminates. Irrespective of the toughening effect, both interleaves showed electrical conductivity and the capability of damage sensing and monitoring. A linear model is developed and experimentally verified to show that damage monitoring can be done using such SWCNTs interleaves and is suitable for structural monitoring applications.

Similarly, in the third application of multifunctional laminate, the ability of SWCNTs dispersed thermoset polymer for cure monitoring was studied. Thermoset polymers, which are widely used as binding materials in FRP composite manufacturing, need to be cured at high temperatures so that the epoxy and its binders form the near-perfect chemical bond for high strength. A degree of cure of over 90% is desired for high strength, so monitoring degree of cure development during the manufacturing of composites is crucial. There are several cure monitoring methods, but most of them are sampling methods which are destructive and time-consuming. In alternate with these destructive methods, some *in-situ* non-destructive methods are also used in the production line. But these *in-situ* methods also come at the cost of introducing poor regions suitable for damage initiation, or increased cost or complexity. Hence, in alternative to this, a new *in-situ* method developed by application of SWCNTs-based nanocomposite sensor capable of measuring and monitoring the development of the degree of cure during the curing process at one or multiple locations as per the requirement is developed and presented.

In conclusion, the improvement of Mode I fracture toughness and electrical conductivity by introducing SWCNTs as interleave is demonstrated. The ability of interleaved laminate to monitor the damage condition suitable for structural health monitoring application is studied. Similarly, the SWCNTs dispersed nanocomposite sensor suitable for continuous, *in-situ* cure monitoring is developed and ready for commercialization.

List of Publications

A. Publications

1. [Journal publication] **B. Mahato**, S.V. Lomov, A. Shiverskii, M. Owais, and S.G. Abaimov, A Review of Electrospun Nanofiber Interleaves for Interlaminar Toughening of Composite Laminates, Polymers, 2023, doi.org/10.3390/polym15061380.

2. [Journal publication] **B. Mahato**, S.V. Lomov, M. Jafarypouria, M. Owais, S.G. Abaimov, Hierarchical Toughening and Self-diagnostic Interleave for Composite Laminates Manufactured from Industrial Carbon Nanotube Masterbatch, Composite Science and Technology, 2023, doi.org/10.1016/j.compscitech.2023.110241.

3. [Conference proceeding] **B. Mahato**, S.V. Lomov, S.G. Abaimov, Quality Control and Cure Status Monitoring Sensor based on Industrial Carbon Nanotube Masterbatch, IEEE Xplore, 2023, doi.org/10.1109/NANO58406.2023.10231314.

B. Patents

1. [Russia – granted] **B. Mahato**, S.G. Abaimov, S.V. Lomov, Method for Determining or Monitoring the Degree of Hardening of Thermosetting Polymers, patent no. RU 2 796 241 C1, granted on May 18, 2023.

2. [China – granted] **B. Mahato**, S.G. Abaimov, S.V. Lomov, The Method for Determining or Monitoring the Degree of Cure of Thermoset Polymers, patent no. CN 117233243 A, published on December 15, 2023.

C. Conference presentations

1. [Oral] **B. Mahato,** S.V. Lomov, S.G. Abaimov, Quality Control and Cure Status Monitoring Sensor based on Industrial Carbon Nanotube Masterbatch, 23rd IEEE International Conference on Nanotechnology, IEEE-NANO, Jeju Island, South Korea, 2023.

2. [Oral] **B. Mahato**, S.V. Lomov, S.G. Abaimov, Multifunctional Interleave Manufactured from Industrial Carbon Nanotubes Masterbatch, 13th International Conference on Key Engineering Materials (ICKEM2023), Istanbul, Türkiye, 2023.

3. [Poster] **B. Mahato**, S.V. Lomov, S.G. Abaimov, Toughening and Self-diagnostic Carbon Nanotubes Interleave Manufactured from Industrial Masterbatch, 4th International Online Conference on Nanomaterials (IOCN2023), Online, 2023.

D. Non-thesis publications relevant to the field

1. [Journal publication] M. Jafarypouria, **B. Mahato**, S.G. Abaimov, Separating Curing and Temperature Effects on the Temperature Coefficient of Resistance for a Single-Walled Carbon Nanotube Nanocomposite, Polymers, 2023, doi.org/10.3390/polym15020433.

2. [Conference proceeding + Oral] **B. Mahato**, S.V. Lomov, S.G. Abaimov, Computationally Efficient Methodology to Compute Virtual Permeability of Fibrous Laminates, 23rd International Conference on Composites Materials (ICCM23), Belfast, United Kingdom, 2023.

3. [Journal publication] E. Syerko, T. Schmidt, D. May, C. Binetruy, S.G. Advani, S. Lomov, L. Silva, S. Abaimov, N. Aissa, I. Akhatov, M. Ali, N. Asiaban, G. Broggi, J. Bruchon, B. Caglar, H. Digonnet, J. Dittmann, S.

Drapier, A. Endruweit, A. Guilloux, R. Kandinskii, A. Leygue, **B. Mahato**, P. Martínez-Lera, M. Matveev, V. Michaud, P. Middendorf, N. Moulin, L. Orgéas, C.H. Park, S. Rief, M. Rouhi, I. Sergeichev, M. Shakoor, O. Shishkina, Y. Swolfs, M. Tahani, R. Umer, K. Vanclooster, R. Vorobyev, Benchmark exercise on image-based permeability determination of engineering textiles: Microscale predictions, Composites Part A: Applied Science and Manufacturing, 2023, doi.org/10.1016/j.compositesa.2022.107397.

4. [Conference proceeding + Oral] **B. Mahato**, S.V. Lomov, I.S. Akhatov, S.G. Abaimov, F, Jung, N. Grigat, B. Vollbrecht, M. Kolloch, T. Gries, Micro-CT based assessment of 3D braided Al_2O_3 reinforcement uniformity and permeability of all-oxide ceramic matrix composites production processes, Proceedings of the 20th European Conference on Composite Materials (ECCM20), v. 1, pp. 408-414, doi.org/10.5075/epfl-298799_978-2-9701614-0-0, ISBN 978-2-9701614-0-0.

Acknowledgments

I am profoundly grateful to my supervisor Prof. Sergey G. Abaimov and co-supervisor Prof. Stepan V. Lomov for their guidance, support, and suggestion during my PhD research. I especially appreciate their attention to detail in polishing my papers and conference presentations and fruitful discussions to tackle the research problems. I have learned a lot from the interactions and discussions, which helped me to become a better scientist and ask better questions.

I would like to express my sincere gratitude to Prof. Iskander S. Akhatov and Prof. Ivan Sergeichev for providing an opportunity to join the Center of Materials Technologies and guiding me with constructive feedback throughout the PhD research as a member of my individual doctoral committee.

I am very thankful to Prof. Albert Nasibulin, Prof. Dmitry Kolomenskiy, and Prof. Dmitry Krasnikov from Skolkovo Institute of Science and Technology, Moscow, Prof. Amit Rawal from Indian Institute of Technology, Delhi, and Prof. Qiang Liu from Nanjing University of Aeronautics and Astronautics, Nanjing for accepting to be PhD jury members for final defense.

This research would not have been possible without the support of my collaborators. I acknowledge and thank Prof. Kolos Molnar and Dr. He Heijun from the Budapest University of Engineering and Technology, Hungary, for providing the electrospun polymeric veil. I acknowledge and thank Prof. Alexander Safonov, Prof. Ivan Sergeichev, Sergey Gusev, Kamil Yusupov, Stepan Konev, Artem Sulimov, Oleg Dubinin, and colleagues from the Center of Materials Technologies and Laboratory of Micro- and Nanomechanics for their help and support with experimental works. I acknowledge and thank Georgy Klushin, Viktoria Kryakovskaya, and Aleksandr Loskutov for their assistance with filing and submitting patent applications in Russia and China.

The third part of the research on cure monitoring was funded by the Skoltech Transitional Research and Innovation Program (STRIP) grant no. 4-STRIP2022-2023.

Finally, and most importantly, my heartfelt thanks to my parents, siblings, and family; without them, this work would not be possible.

Moscow, 7 September 2023
Biltu Mahato

Dedicated to my parents.

Table of Contents

List of Acronyms

0D	Zero-dimensional
1D	One-dimensional
2D	Two-dimensional
3D	Three-dimensional
5H	5-harness
$AgNO_3$	Silver nitrate
AgNW	Silver nanowire
Al_2O_3	Aluminum oxide
ASTM	American Society for Testing and Materials
CC	Compliance calibration
CD	Cross-direction
CF	Carbon fiber
CFRP	Carbon fiber reinforced polymer
CNC	Computerized numerical control
CNT	Carbon nanotube
DC	Direct current
DCB	Double cantilever beam
DETA	Dynamic dielectric thermal analysis
DGEBA	Bisphenol A diglycidyl ether
DMA	Dynamic mechanical analysis
DMF	Dimethyl-formamide
DMM	Digital multimeter
DSC	Differential scanning calorimetry
EDX	Energy dispersive X-ray
ENF	End notch flexure
FM	Fiber modification
FRP	Fiber-reinforced polymer

FT	Fracture toughness
FTIR	Fourier transform infrared
GFRP	Glass fiber reinforced polymer
G1i	Mode I initiation [J/m^2]
G1p	Mode I propagation [J/m^2]
G2i	Mode II initiation [J/m^2]
G2p	Mode II propagation [J/m^2]
GF	Glass fiber
GNP	Graphene nanoparticles
HC interleave	High concentration interleave
IRM	Interlaminar region modification
LC interleave	Low concentration interleave
m	Mode ratio
MB	Masterbatch
MBT	Modified beam theory
MCC	Modified compliance calibration
MD	Manufacturing direction
MHz	Megahertz
MsM	Microscale modification
MWCNT	Multi-walled carbon nanotube
NCF	Non-crimp fabric
NMR	Nuclear magnetic resonance
NsM	Nanoscale modification
PA	Polyamide
PAI	Polyamide-imide
PAN	Polyacrylonitrile
PCL	Polycaprolactone
PES	Polyethersulfone
PET	Polyethylene terephthalate
PM	Prepreg/Fabric modification

PPS	Polyphenylene sulfide
PVB	Polyvinyl butyral
r	Correlation coefficient
RM	Resin modification
RPM	Rotation per minute
SAM	Scanning acoustic microscope
SEM	Scanning electron microscopy
SWCNT	Single-walled carbon nanotube
TBA	Torsional braid analysis
TEM	Transmission electron microscopy
TiO_2	Titanium dioxide
UD	Unidirectional
VARTM	Vacuum-assisted resin transfer molding
VI	Vacuum infusion

Chapter 1

Introduction

This chapter presents the motivation behind the research undertaken during PhD presenting the background and overview of the research. The chapter concludes with a brief discussion of the main content of each following chapter, presented as the structure of the thesis.

1.1 Motivation

Fiber-reinforced polymer (FRP) composites are widely used in the aerospace industry, where high strength is demanded for a low weight of the structures. With the increasing progress of the performance of composites and their manufacturing processes, the application of composite materials is widely expanding into various other industries like automotive and transport, oil and gas industry, civil infrastructures, sports, energy, offshore, etc. This popularity of the composite material is attributed to its unique combination of properties like high strength and stiffness with lightweight, improved durability, and corrosion resistance compared to conventional materials. Recently, there has been a growing trend of modification of FRP composite materials with the introduction of nano-scale reinforcements which not only enhance the primary functionality of load bearing but also offer a secondary functionality. Such materials are commonly known as multifunctional materials [1–6]. These multifunctional materials are produced by modifying the constituents (fiber or matrix or interface) with the introduction of nanoscale reinforcement, which is broadly classified into nanofillers of zero-dimensional (0D), one-dimensional (1D), two-dimensional (2D), or three-dimensional (3D) structure. 0D nanofillers include quantum dots, nanoparticles; 1D nanofillers include nanotubes, nanorods, nanofibers, nanopillars, nanowires; 2D nanofillers include nanopores, nanoplates, nanosheets, and 3D nanofillers include nanocomposites of hierarchical structures made from self-assembly of one or several 0D, 1D, or 2D nanofillers [7–10].

Carbon-based nanofillers are one of the most promising materials currently attracting a lot of interest for extensive applications in various industries. They are available in 0D (fullerenes, nano-diamonds), 1D (carbon nanotubes), 2D (graphene), and 3D (carbon black) structures [11,12]. When these carbon-based nanofillers are added to electrically insulative polymers, the electrical conductivity of the insulative polymer increases and converts it into an electrically conductive polymer. The obtained electrical conductivity depends on the concentration of nanofillers in the polymer, which initially remains constant but increases non-linearly with increasing nanofiller concentration above the percolation threshold [13]. For instance, nanocomposites produced by the addition of single-walled carbon nanotubes (SWCNT) have demonstrated metal-like electrical conductivity [14] at as low as a fraction of the weight percentage concentration of SWCNTs.

Production of the nanocomposite starts with the addition and uniform dispersion of nanofillers but when the dry form of nanofiller is added to the polymer, the nanofiller agglomerates because of its large surface area and van der Waals force. Such agglomeration areas are not desired for useful mechanical and functional properties of the nanocomposite, so they must be dispersed uniformly throughout the nanocomposite, which is a tedious process. Hence, the concept of masterbatch was introduced to address this problem.

Masterbatch is the concentrated form of nanofillers that are produced to ensure that the nanofillers in dry form are mixed uniformly with the polymer and mixing consistency is maintained throughout the material. These masterbatches offer several advantages over the conventional dry form of nanofillers. Some advantages are as,

(a) High quality: Masterbatch provides easier mixing to get uniformity and consistency, ensuring high-quality dispersion compared to dry form.
(b) Cheaper: No need for expensive mixing machinery, which is necessary when the dry forms of nanofillers are used.
(c) Easier handling: The dry form of nanofillers is already mixed in the polymer, removing the health-related effects and concerns.

Now such masterbatches are industrially produced and available in the market for various carbon-based nanofillers with high throughput capability. Hence, the application of masterbatch-based manufacturing is scalable manufacturing suitable for large composite structures.

Given this background, this research focuses on the application of carbon nanotubes (CNTs) firstly dispersed in the polymeric solution for veil and secondly dispersed in the epoxy resin in the form of interleave for the development of multifunctional FRP composite material. Interleave is a thin layer of material introduced as an additional layer between the laminae (or interlaminar region) of a composite laminate. The method of introducing the veil/interleave is known as interleaving. Three functionalities of FRP are studied, namely, hierarchical toughening, structural health monitoring, and cure monitoring function.

1.2 State of the art

1.2.1 Hierarchical toughening and structural health monitoring

High-performance structural FRP composite laminates are commonly produced either by autoclave technology or by liquid composite molding, based on preforms as layups of 2D plies with fibrous reinforcement. These laminates offer high in-plane mechanical properties, determined by the fibers; however, they suffer from poor out-of-plane properties because interlaminar fracture toughness

(FT) is provided by matrix and only a partial fibrous involvement in the form of the fiber-bridging effect. It makes a composite laminate highly susceptible to failure by delamination under either through-the-thickness loads, out-of-plane impacts, external loadings, environmental factors, or manufacturing defects [15,16]. Three modes of fracture by delamination include Mode I (crack opening), Mode II (crack in-plane shear), and Mode III (crack out-of-plane shear). Common sites of delamination in composite structures are internal and external ply drop sites, corners and T-joints, solid-sandwich transition zones, curved or straight free edges, etc. [17]. Delamination reduces the strength and stiffness of the composite laminate and affects the overall performance of the composite structure, especially in compression, possibly leading to catastrophic failure [18–20]. Due to this, a lot of interest has been received in developing a modification method to not only address the delamination problem but also to offer an additional possibility of *in-situ* monitoring of the delamination process in-service. These modification methods may be microscale modification (MsM) or nanoscale modification (NsM).

The most common MsM include 3D modification by Z-pinning [21], 3D weaving [22], stitching [22], fiber hybridization [23], short fiber in the interlaminar region, or matrix modified by short fiber [24], etc. These methods are effective in enhancing the interlaminar properties but come with associated disadvantages and limitations. For example, 3D modification methods create resin pockets, leading to a decrease in in-plane properties and interleaving polymeric veil drastically reduces the conductivity of laminate. Likewise, none of these MsM offers an opportunity to monitor the delamination in-service.

Hence, in this direction of research, the goal was to develop a multifunctional composite that not only improves the FT of composite laminate but also provides the possibility of monitoring the condition of damage suitable for structural health monitoring applications. Two methods were proposed as:

A. Polymeric veil/interleave

In this method, the thin mat is introduced as an additional layer between the laminae of a composite laminate. The fiber diameter in the fibrous veil/interleave ranges from tens of nanometers to a few micrometers. The fine diameter and evenly distributed fibers ensure low areal density and low thickness of the veil [25]. Hence, the impact of introducing a veil/interleave on the laminate thickness and mass is negligible. The overall fiber volume fraction in the composite laminate is not affected much, guaranteeing a least compromise on the in-plane mechanical properties of the laminate. Similarly, the veil/interleaves are highly porous and thus do not disrupt the resin flow during impregnation or curing [26]. The effectiveness of the veil/interleave for toughening composite laminates is demonstrated without a doubt [27–29]. Several polymeric material choices can be considered for the polymeric veil, so a review was done for selecting the polymer, as detailed in the analysis presented in Chapter 2 (Section 2.1 - Section 2.4).

So, a polymeric veil consisting of CNTs in the nonwoven nanofibers veil/interleave was proposed. CNTs were added to convert the insulative polymeric nonwoven nanofiber interleave into an electrically conductive interleave so that it can be used for structural health monitoring purposes, along with its primary functionality of toughening. Polyacrylonitrile (PAN) modified with CNTs veil was produced successfully however, the electrical conductivity of veil was not achieved (result detailed in Section 2.5). Hence, another alternative NsM method of interleave produced from CNTs masterbatch is proposed.

B. Carbon nanotube interleave

Alternatively, the NsM includes nano-stitching [30], matrix toughening by carbon-based nanoparticles [31] such as graphene, carbon nanotubes (CNT), metal oxides based nanoparticles [32] such as alumina, silica, polymer-based nanoparticles [33] like poly butyl acrylate, poly methyl methacrylate in the form of solid or core/shell structure, modification of reinforcing fibers with CNTs forest on the fiber surface and/or interface region [33]. Unlike the MsM mentioned above, these NsM, at proper replacement of fiber-bridging effect with nanoscale bridging, do not compromise in-plane properties and, depending on the modification type, show improvement in fracture toughness. Additionally, these NsM add multiscale hierarchical toughening mechanisms [34,35] which are not noted in case of MsM. Compared to MsM, a NsM offers a higher surface-to-volume ratio, which presents the possibility of increasing the amount of energy dissipated during fracture. An exponential relation between the filler size and total energy dissipated during fracture was observed and reported [36]. Despite such advantages over MsM, NsM suffers from several limitations which must be addressed. The limitations are linked, among other problems, to: (a) filtration [37] - nanoparticles in matrix filtered on fibrous reinforcement during manufacture; (b) scalability [38] - growing CNTs forest on the reinforcing fibers is not a scalable solution for large composite parts like aircraft fuselage or wing; (c) handling [39] - difficulty in handling dry nano-powders because of their health effects. Despite these drawbacks, this approach provides many desired benefits. For example, the NsM with carbon-based nanoparticles makes the interleave electrically conductive and provides a possibility of monitoring the state of damage of the laminate, presenting a self-diagnostic ability. The NsM can be applied in a few ways, such as modification of reinforcing fiber, matrix, prepreg or textile, and interlaminar region.

Wicks et al. [40] modified the reinforcing alumina fibers by growing aligned CNTs on their surface. The modified fibers were called "fuzzy fibers" and the aligned CNTs extended across interlaminar and intralaminar regions. The effect of such modification of fiber on Mode I fracture toughness was mixed, depending on the epoxy used. Aerospace class epoxy showed a deteriorating effect up to 61% whereas marine class epoxy showed improvement up to 43%.

Burkov et al. [41] modified the epoxy with SWCNTs, impregnating and hot-pressing carbon fabrics to fabricate composite laminates. The Mode I fracture toughness of baseline and modified laminates was studied. It was noted that the Mode I fracture toughness of the modified laminate decreased by up to 46% compared to the baseline laminate, and damage sensing was not studied.

Zhang et al. [42] modified carbon fiber prepregs with CNTs deposition by applying the spray coating technique. An improvement of 46% in Mode I fracture toughness was noted with a capability to monitor the structural health by *in-situ* damage sensing capability. Wan et al. [43] modified the reinforcing woven glass fibers by immersing them in a multi-walled carbon nanotubes (MWCNTs) solution. The laminate was noted to become conductive and was used to monitor the *in-situ* damage growth in the Mode I fracture toughness test. The effect of such modification of reinforcing fiber on the Mode I fracture toughness was not studied. Similarly, Tzounis et al. [44] modified the reinforcing unidirectional glass fibers by blade coating wet-chemical deposition process. The modified laminates were highly conductive and were demonstrated to be capable of damage sensing. The effect on Mode I fracture toughness was not studied.

Liu et al. [45] inserted multifunctional polyethersulfone-carbon black film into the interlaminar region of carbon fiber-reinforced polymer to improve the Mode I fracture toughness and delamination monitoring sensitivity. Improvement in Mode I fracture toughness value of 222 J/m^2 for baseline laminate to 414 J/m^2 (~1.9×) for modified laminate was noted. The *in-situ* delamination monitoring was also achieved. A film with no carbon black displayed the best sensitivity to damage monitoring. It was possible because the conductivity measured was given by the reinforcing carbon fiber rather than the carbon black. Garcia et al. [30] modified the interlaminar region with vertically aligned CNTs by “transfer-printing” the CNTs on a carbon fiber prepreg. This method improved the Mode I fracture toughness of laminate from 210 J/m^2 to 530 J/m^2 (~2.5×). Besides these investigations, other studies on how adding CNTs affects the Mode I fracture toughness of composite laminates are summarized in Table 3.1.

In view of this, CNTs in the form of interleave manufactured from industrially available masterbatch and introduced in the interlaminar region of the composite laminate was identified as a method to meet the set goal. CNTs interleave showed improvement in FT and the electrical conductivity as desired for structural health monitoring was also achieved. The detailed results are presented and discussed in Chapter 3.

1.2.2 Cure monitoring

Thermoset polymers are one of the most widely used binding matrix materials in FRP composite, ranging from aerospace and alternative energy generation to automotive manufacturing. They are lightweight, provide good wetting and adhesion to reinforcement, and are relatively inexpensive to produce while providing good mechanical properties. However, these properties are very much dependent on how well the matrix cures.

The curing cycles of thermoset polymers, like epoxy, dictate the degree of cure and subsequent material properties. Monitoring the degree of cure for composite industries, where both in- and out-of-autoclave curing cycles are run, is critical. These cycles are often changed during the manufacturing process to ensure an acceptable degree of cure while balancing manufacturing time. It is essential for out-of-autoclave, on the one hand, and for fast curing systems (automotive industry) on the other hand. Currently, expensive testing techniques such as dielectric, acoustic, ultrasonic, thermal monitoring, and fiber optical strain gauge are used to ascertain how well the epoxy has been cured. These on-line methods are widespread on the production line but require costly equipment. Besides the costly associated hardware and software, specialized technicians must operate and interpret results. Similarly, the introduction of fiber optics sensors in the composite creates weak sites for future damage initiation due to the mismatch between the diameter of reinforcing fiber, which is ~7-15 µm however, the thinnest fiber optic sensor is ~120-150 µm. Such a compromise on mechanical property could be catastrophic and is not desired.

Other off-line methods include Nuclear Magnetic Resonance (NMR), Fourier Transform InfraRed (FTIR) spectroscopy, Differential Scanning Calorimetry (DSC), Rheometers, Dynamic mechanical analysis (DMA), Torsional braid analysis (TBA), and dynamic dielectric thermal analysis (DETA). These methods are sampling methods where a sample for testing is taken from the composite structure by destructive method during the curing cycle by disrupting the production line. These destructive methods not only create a weak location but also the disruption of the cure cycle is not an energy-efficient method. Similarly, these testing tools are mostly laboratory-only methods and can't be installed on the production line [46,47]. Hence, there is a need for a non-destructive, inexpensive, easy-to-operate, scalable, *in-situ,* and continuous cure determining and monitoring technique.

To meet all these needs, Lee et al. [48] proposed to monitor the degree of cure of thermoset polymers using measurements of electrical conductivity of a special sensor made of epoxy film with aligned MWCNTs in it, co-cured with the composite prepreg. Unlike this expensive and unscalable method, in this research, we present and introduce a carbon nanotube masterbatch-based nanocomposite sensor as a randomly dispersed SWCNTs configuration from a commercially available masterbatch. The details of the materials, methodology, and results are presented and discussed in Chapter 4.

1.3 Research objectives

The research objectives are listed below as,

- To modify the constituents of FRP composite to make them multifunctional.
- To use carbon-based nanofillers in the form of masterbatch so that it can be a scalable solution applicable for large composite structures.
- To address the delamination problem by improving interlaminar fracture toughness with an additional possibility of *in-situ* monitoring of delamination suitable for structural health monitoring.

- To create a non-destructive, inexpensive, easy-to-operate, scalable, *in-situ,* and continuous cure determining and monitoring technique using the functional property of nanocomposite.

1.4 Novelty

The novelty of this PhD thesis is listed below as,

- The idea of multifunctional composite with the introduction of CNTs particularly for hierarchical toughening with a capability of damage sensing and monitoring suitable for structural health monitoring existed for a long time now. Several methods were proposed and tested but most of those methods are lab-scale methods not suitable for scalability. However, using masterbatch which is now produced at an industrial scale with high throughput is a scalable solution for large composite structures like aircraft fuselage or wings.
- There is a need for an *in-situ* cure monitoring technique as the final property of the composite structure depends on the degree of cure. The existing methods are either sampling methods or existing *in-situ* methods are either complex, expensive, require expensive tools, or weaken the mechanical performance. To meet these requirements, a SWCNTs-based nanocomposite sensor is developed, presented, patented, and ready for commercialization.

1.5 Structure of the thesis

This PhD thesis comprises 5 chapters contributing to the research of the application of industrially available CNTs for multifunctional composite laminate. The details of each chapter are presented below as,

Chapter 1: Introduction

This chapter starts with the introduction of the research topic, presents motivation, state-of-the-art, and ends with the details of the structure of the thesis. The state-of-the-art in the three broadly studied functionalities of hierarchical toughening, self-diagnostic, and cure monitoring are reviewed.

Chapter 2: Electrospun Polymeric Interleave

This chapter deals with the production of an electrospun polymeric veil. There are numerous choices of polymeric material available for electrospinning. Hence, a suggestive method is presented to select the material for electrospinning based on the criteria of achievable FT. The experimental results obtained for the PAN veil produced by the introduction of CNTs are also presented. The publications on the topic and the authors' contributions to the publications are mentioned at the end of the chapter.

Chapter 3: Carbon Nanotubes Masterbatch Interleave

This chapter presents the details of the materials used in the experiments, the methodology used to produce samples, experiments performed to quantify and demonstrate the hierarchical toughening effect, and a discussion of results obtained for CNTs interleaved laminate. It is followed by the self-diagnostic test scheme, tests, results, and discussion. The publications on the topic and the authors' contributions to the publications are mentioned at the end of the chapter.

Chapter 4: Cure Monitoring Property

The materials, methodology, result, and discussion for cure monitoring property of CNTs in the form of nanocomposite sensors are detailed in Chapter 4. The applicability of this property as a sensor is also discussed. The publications on the topic and the authors' contributions to the publications are mentioned at the end of the chapter.

Chapter 5: Conclusion and Outlook

This chapter summarizes the results and concludes the research performed during the PhD. An outlook for future researchers working with industrially available CNTs masterbatch is also discussed briefly at the end of the chapter.

Chapter 2

Electrospun Polymeric Interleave

2.1 Electrospinning

Electrospinning is a flexible, simple, and cost-effective technology to produce extremely fine fibers of diameters ranging from tens of nanometers to a few micrometers for a wide range of materials [49]. It is a top-down technique of manufacturing [50] where the millimeter-sized polymer pellets are dissolved in an organic solvent, and then electrospun. Electrospun nanofibers are long, continuous, easily aligned, and inexpensive. These nanofibers have unique properties like high surface-area-to-volume ratios, high aspect ratios (length/diameter), and high mechanical properties (stiffness and strength) because of the high molecular orientation along the fiber axis. Electrospinning can easily be scaled for mass production in industrial applications [49–51]. Figure 2.1a shows the schematic representation of electrospinning used to manufacture the electrospun veil. The major parts of the setup include a syringe with a nozzle at its tip, a conducting collector plate, and a high-voltage source that connects the collector and the nozzle. The syringe with the nozzle tip holds the polymer solution. When high voltage is applied, the polymeric solution in the syringe is pulled out of the syringe. Liquid droplets are formed at the tip of the nozzle, which are further converted into a jet of polymeric liquid, finally being collected on the conducting collector plate, resulting in the formation of the continuous polymeric fiber. After collecting layers of such a continuous fiber, one over the other, it forms a nonwoven, porous nano-fiber veil (Figure 2.1b). The diameter of fiber depends on the applied voltage and polymeric solution. Similarly, the veil areal density and thickness depend on the time of manufacturing. Once the desired thickness is achieved, the electrospun veil can be separated from the collector and transferred onto a substrate.

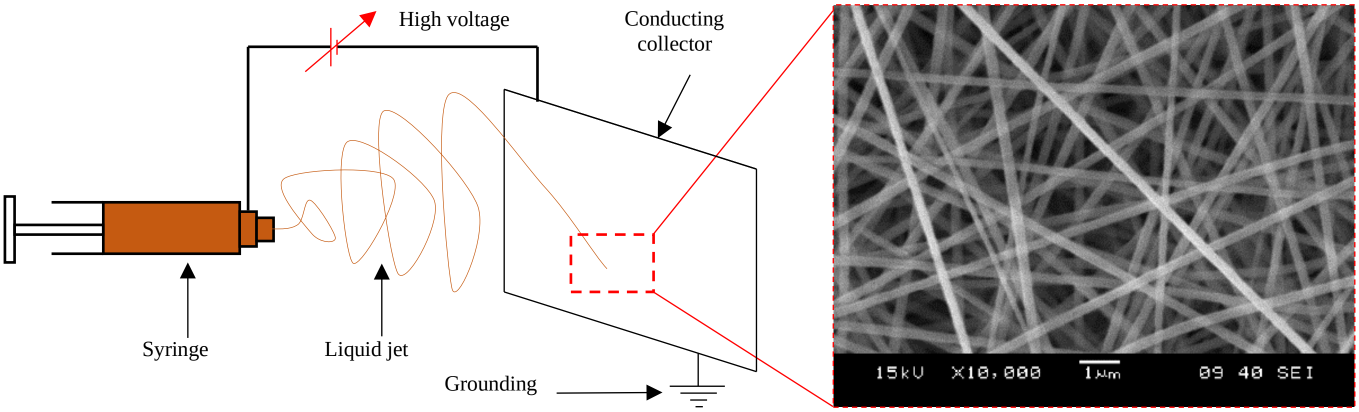

(a) (b)

Figure 2.1. Schematic representation of (a) electrospinning, and (b) a typical PAN veil produced by electrospinning. Details of manufacturing of PAN and its modified veils are discussed in Section 2.5.

The electrospun veils are placed between two plies of fibrous reinforcement at desired locations in the laminate layup. Then the FRP laminate is manufactured as per the standard manufacturing procedure. Manufacturing methods include vacuum infusion, compression molding or press-clave, autoclave, hand wet-layup, and vacuum bagging, to name a few. The veil thickness under the processing pressure is sufficiently small. Hence, the laminate fiber volume fraction is not affected much, and laminate in-plane mechanical properties are preserved [25].

Depending on the test procedure, the samples to measure toughness are manufactured with the interleaves placed at the laminate mid-plane or every ply-ply interface. In particular, to measure the Mode I initiation and propagation energy, the double cantilever beam (DCB) test is conducted as per the American Society for Testing and Materials (ASTM) D5528 standard [52]. Similarly, the end notch flexure (ENF) test measures the Mode II initiation and propagation fracture toughness (FT) per ASTM D7905 standard [53].

2.2 Polymeric materials for veil

The FT values reported in the literature are analyzed based on the veil materials and their modifications, and a comparative analysis of attainable FT with veil is discussed as:

2.2.1 Polyethylene terephthalate

Tzetzis et al. [54,55], Kuwata et al. [56,57], Quan et al. [29,58,59], Fitzmaurice et al. [60], Del Saz-Orozco et al. [61] studied the effect of interleaving polyethylene terephthalate (PET) veil on Mode I and Mode II toughening for glass- and carbon fibers laminate composite. A general trend of improvement on all FT parameters was observed, with an exception noted in Mode I properties by Del Saz-Orozco et al. [61].

a. Neat PET veil

Tzetzis et al. [54,55] explored the possibility of using the veil as an interleave for repair purposes (to attach patches) for glass fiber-reinforced polymer (GFRP) laminates [54,55]. Significant improvements in Mode I initiation fracture toughness (G1i) and Mode I propagation fracture toughness (G1p) were reported to increase with the veil areal density, reaching up to 740% and 770%, respectively, for the veil areal density of around 25-40 g/m^2. However, it should be noted that these significant improvements are given relative to the values reported for the "as-received" in-service GFRP surfaces. When these "as received" in-service laminates were treated using hand abrasing and grit blasting, the toughness increased significantly compared to “as received” even in the absence of interleaves. The improvement due to veil interleaved can be re-calculated relative to “treated” surfaces to become only a moderate of 16-49%.

In contrast, Kuwata et al. [56,57] explored the effect of the PET veil as an interleave in the newly manufactured carbon fiber reinforced polymer (CFRP) laminate. The study investigates veil’s effect on various epoxy matrices (civil and aerospace applications) and carbon fiber (CF) reinforcement architectures (unidirectional (UD), satin weave, plain weave). For the UD-reinforced composite, a stable but moderate increase of 15-56% is observed almost independent of resin type. The low value of the increment is probably explained because the interleave replaces the intrinsic UD fiber bridging effect with tough thermoplastic bridging of nanofibers replacing strong UD plies bridging. For woven composites, the effect of PET interleaves is stronger as expected due to the weak fiber-bridging of original reinforcement. For satin weave composites, PET veils have a moderately positive effect (up to 94% for epoxy; up to 33% for vinyl ester) on Mode I toughness and a very pronounced effect on Mode II toughness, bringing values to 3100-3630 J/m^2 for initiation and 3750-4760 J/m^2 for propagation, with the effect being stronger for epoxy comparing to vinyl ester. For plain weave composites, veils’ introduction generated a significant positive effect only for epoxy resin (Mode I up to 175%, Mode II up to 88%), while for vinyl ester, the effect, although always positive, was less significant. A similar effect of moderate improvement in UD CF reinforcement but a stronger improvement in the weave CF reinforcement (5-harness (5H) and non-crimp fabric (NCF) weave) was also noted in Quan et al. [29,59]. The values of FT noted by Kuwata et al. [56,57] and Quan et al. [29,59] are in a comparable range despite a slight difference in weave architectures (satin, plain weave vs. 5H, NCF weave).

Similarly, Fitzmaurice et al. [60] studied the effect of multiple veil layers in the laminate (one vs two veil layers in-between each pair of plies) for weave glass fiber (GF) reinforcement and noted the crack deviation from veil region to fiber-matrix interface region. A similar crack deviation was also noted by Del Saz-Orozco et al. [61] for UD GF reinforcement. The phenomenon of crack deviation was attributed to the strong interaction between the PET veil and the matrix. Despite crack deviation, Fitzmaurice et al. [60] noted a moderate improvement in FT but Del Saz-Orozco et al. [61] noted a decrease in FT because of the difference in the GF reinforcement architectures (weave vs. UD).

b. PET-CF hybrid veil

Tzetzis et al. [55] repaired the in-service FRP structure by grit blasting the surface before the CF or PET-CF hybrid veil was inserted as an interleave. It was inserted in between the repaired structure and the patch, followed by infusion. Grit blasting of in-service FRP structure induces many new sites for stronger bonding between the structure and patch material. The implemented veil does not impede the repair and enhances the fiber-bridging effects. Notable improvements (up to 600% for initiation and 1100% for propagation) were reported for Mode I toughness but attributed mainly to grit blasting.

The use of CF or PET-CF hybrid veils in newly manufactured laminates had a mixed effect [56,57]. For satin weave composites, the detrimental effect of the CF implementation was masked by PET improving toughness. Still, the tendency is clear: the higher CF's share was implemented, the poorer the results were. Pure CF interleave led to a decrease in all values of FT. For plain weave laminate, the tendency was not pronounced but still present. CF interleaves improved Mode II toughness for UD laminates, but its use cannot be recommended because of the degradation of the Mode I toughness properties.

c. Nano-modified PET veil

PET veil demonstrated its toughening capabilities; however, introducing PET veil decreases the laminate electric conductivity [58]. To address this problem, two different concentrations of MWCNTs were airbrushed on the PET veil surface. It was found that airbrushing as low as 0.4 g/m^2 of MWCNTs on the veil improves the laminate FT (up to 65% for Mode I and 100% for Mode II) and overall electrical conductivity (up to 65%). It is a significant improvement in FT and electrical conductivity compared to the baseline laminate properties, whereas a neat PET veil improves FT only. Airbrushing a higher concentration of MWCNTs increases the electrical conductivity further but decreases the FT.

Summarizing, the PET veil has a positive impact on the toughening mechanism for both modes, for both epoxy and vinyl ester resins, for both UD and weave CF reinforcement and for weave GF reinforcement architectures. The effects with epoxy are typically much more pronounced than with vinyl ester. PET-CF hybrid veil shows mixed results. Airbrushing a lower concentration of nano-reinforcement on the veil surface is enough to improve the FT and electrical conductivity. Based on these results, the PET veil and its nano-modified counterpart are recommended for structural delamination control applications.

2.2.2 Polyphenylene sulfide

Quan et al. [29,59,62], Ramirez et al. [63], and Ramji et al. [64] reported the application of polyphenylene sulfide (PPS) veil to improve the fracture performance of a CFRP composite. No study was reported for GFRP. Quan et al. studied the effect of interleaving neat PPS veil [29,59] and nano-modified PPS veil [62] veil on FT. Neat PPS veil interleaved for different CF reinforcement architectures (UD vs weave), whereas nano-modified PPS veil interleaved for UD CF only. Ramirez et al. [63] explored the impact of manufacturing directionality (compared to reinforcing UD CF) of the veil on FT. Ramji et al. [64] focused on the combined effect of interleaving the PPS veil and interfacial orientation of CF on delamination migration and FT.

a. Neat PPS veil

Interleaving neat PPS veil in CF laminate showed a clear trend of high FT for weave CF reinforcement in comparison to UD CF reinforcement [29,59]. A similar trend was also observed for neat PET veils. This trend is observed moderately for Mode I (up to ~75% increase) and profoundly for Mode II loading, bringing the value of FT to 2200-2600 J/m^2 for initiation and 3000-3200 J/m^2 for propagation.

Ramirez et al. [63] manufactured CF laminates with PPS veil oriented in the manufacturing direction (MD) and cross-direction (CD) perpendicular to MD. A significant change (up to ~2×) in Mode I FT was noted for a thick veil of 38 g/m^2 irrespective of veil orientation. It is necessary to note that mechanical anisotropy of PPS veil showed no impact on achievable FT because the PPS veil is a nonwoven structure with randomly oriented fibers.

Ramji et al. [64] observed delamination migration when an element of 90° or 45° plies was present in the midplane. Delamination migration adds additional crack propagation sites leading to high FT. It can be noted that the highest FT value was reported for 90°/90° compared to all other combinations of 0°, 45°, and 90° interfacial orientation.

b. Nano-modified PPS veil

A higher improvement in the FT was noted when the neat PPS veil was modified by doping a lower concentration (up to 0.6 g/m^2) of MWCNTs for both Mode I and Mode II. However, when MWCNTs concentration was increased to 1.45 g/m^2, the Mode I FT decreased, becoming worse than for baseline laminates. The Mode II FT also decreased only moderately but still was better than the baseline. Irrespective of concentration, doping graphene nanoparticles (GNPs) on neat PPS veil showed detrimental effects on Mode I FT. A lower concentration of

GNPs showed a good improvement in Mode II FT, which decreased slightly for higher concentrations.

Such behavior of MWCNTs and GNPs can be attributed to their 1D and 2D shape, respectively. The addition of a small wt% of MWCNTs introduced additional interactions like MWCNT pull-out and breakage between the PPS nanofibers and epoxy matrix. It resulted in an improved PPS fiber/epoxy adhesion and subsequently led to additional PPS fiber breakage and an improved nanofiber bridging mechanism as a toughening mechanism during the fracture process. For these reasons, the fracture energy was further increased by doping a small amount of MWCNTs on the PPS veils. However, at high wt% of MWCNTs, the PPS nanofiber/epoxy adhesion increased to a sufficient level to prevent the PPS nanofiber pull-out and fiber bridging (the primary toughening mechanism). It caused a considerable drop in fracture energy. In contrast, the 2D-structured GNPs were significantly agglomerated and attached to the PPS nanofibers. It resulted in a decline in the PPS nanofiber/epoxy adhesion [62].

To sum up, interleaving a neat veil improves laminate fracture performance irrespective of the fiber architecture, however, a higher improvement was noted in weave CF compared to UD CF. Airbrushing of lower concentrations of MWCNTs on veil surface improves the fracture performance and electrical conductivity of laminate. Airbrushing GNPs increase electrical conductivity but decreases the FT. Noteworthy, higher concentrations of MWCNTs and all concentrations of GNPs also cause a drastic drop in FT. Based on these results, neat and low concentrations of MWCNTs doping PPS interleave are recommended for delamination control in structural applications. Doping nano-reinforcement like MWCNTs and GNPs improves the electrical conductivity hence it can be recommended in lightning strike protection, electro-magnetic shielding, and damage detection applications.

2.2.3 Polyamide

Beckermann et al. [26], Meireman et al. [27], Garcia-Rodriguez et al. [28], Quan et al. [29], Kuwata et al. [56,57], Del Saz-Orozco et al. [61], Saghafi et al. [65,66], Nash et al. [67,68], Guo et al. [69], Chen et al. [70], Ognibene et al. [71], Pozegic et al. [72], Beylergil et al. [73–75], Alessi et al. [76], Barjasteh et al. [77], Monteserin et al. [78,79], Daelemans et al. [80–82], De Schoenmaker et al. [83], O'Donovan et al. [84], and Hamer et al. [85] reported polyamide (PA) veil as interleave for FRP composite laminate applicable for either carbon or glass fiber reinforcement. PAs of different classes were used in these studies such as PA 6 (sometimes brand name Nylon is used), PA 11, PA 12, PA 66, and PA 69. PA is the most popular material for veils amongst the presented materials as noted by a higher number of studies on PA veils. It has been considered as interleaves for composites manufactured by not only vacuum infusion (VI) and vacuum-assisted resin transfer molding (VARTM) but also compression molding and autoclave manufacturing methods extensively.

a. Neat PA veil

A general trend of improvement in the overall fracture performance of an FRP laminate was observed for both CF and GF, with some exceptional decrease in Mode I FT [23,24,34,39,43,47,50]. These exceptions are caused by various factors like compatibility [56,57,67], mesoscale inhomogeneity caused due to either thick veil [83] or thick veil fiber [76], and weak interface [72]. PA veil in CF reinforcement is identified as more compatible with a vinyl ester-based matrix than the epoxy-based matrix [56,57]. Amongst epoxies, the PA veil is more compatible with BZ9120 epoxy than BZ9130 epoxy reinforced with CF [67].

Quan et al. [29], Kuwata et al. [56,57], and Daelemans et al. [47] observed high FT for weave CF reinforcement and low FT for UD reinforcement interleaved with the PA veil. Similar trends are also noted in PET and PPS interleaved veils.

Woven reinforcement showed promising improvements due to fabric architecture. It resulted in plastically failed PA nanofibers zones, indicating a good load transfer to the nanofibers. Comparatively, in UD reinforcement, the nanofibers blocked the formation of a carbon fiber bridging zone and the delamination propagated between the nanofibers. It resulted in relatively low improvements in FT.

b. Metal modified PA veil

PA veils are modified with different metal-based chemicals for various purposes, which include altering the stiffness and hardness of nanofibers [26], adding antibacterial effects [78], and developing electrically conductive laminate [69,86]. Modification techniques include precipitating silver nitrate ($AgNO_3$) throughout the nanofibrous veil [26], dispersing titanium dioxide (TiO_2) nanoparticles on nanofiber veil [78], painting silver nanowires (AgNWs) solution on veil surface [69], coating Ag (silver-based salt) by electroless plating of the veil [86].

Interleaving modified PA veil with $AgNO_3$ coating [26], AgNWs painting [69], pure Ag paste coating [86], and TiO_2 nanoparticles dispersing [78] demonstrated some improvement in the fracture performance. These studies show that the improvement in modified conditions is comparatively lower than the neat PA interleaved, however, still being higher than the baseline laminate. Such a slight deterioration of FT improvement for modified veil is caused by a weak interface formed by the metal surface. However, it should be noted that AgNWs have the strongest interface among them.

Ag-modified veil adds the multifunctionality of improved conductivity to the laminate. For instance, an AgNWs-painted veil improves laminate conductivity by up to 100× in-plane and 10× in the thickness direction [69]. Similarly, an Ag-plated veil improves conductivity by 1500× in-plane and 25× in the thickness direction [86]. TiO_2 adds antibacterial functionality, making the laminate suitable for marine applications [78]. A strong interest is growing in developing multifunctional interleaves. Metal-modified veil can be used as a multifunctional interleave, but slight deterioration in FT must be considered. Multifunctionality of the upgraded conductivity and the improved antibacterial property is successfully achieved; however, altering the stiffness and hardness of PA nanofiber with $AgNO_3$ coating has not been achieved [26].

To sum up, interleaving of the PA veil always increases the Mode II FT irrespective of reinforcement type or binding matrix. However, for Mode I FT, improved fracture performance depends on various factors like the compatibility of the PA veil with the binding matrix, crack path, reinforcement type, and areal density or thickness of veil. Based on these results, the PA veil is recommended for delamination control in FRP laminates for structural applications. Similarly, metal-modified PA veils are also recommended for the multifunctionality of laminates.

2.2.4 Polyacrylonitrile

VanderVennet et al. [87], Zhang et al. [88], Chiu et al. [89], Razavi et al. [90], Molnar et al. [91], and Eskizeybek et al. [92] studied polyacrylonitrile (PAN) interleave effect in the CFRP laminates and its effect on FT. Zhang et al. compared PAN veil to other veils, whereas others studied PAN veil and its nano modifications.

a. Neat PAN veil

The neat PAN interleaved laminates showed a significant depreciating effect up to -70% on G1i compared to the baseline laminate [87–89,92]. They were outperformed by other material veils, including doped PAN [92]. This reduction in toughness was mainly attributed to problematic impregnation in the presence of a dense veil. A minor positive effect of 18% on G1i was observed only in two cases: for VARTM [90] with very low veil areal density of 1 g/m^2 and autoclaving [87] of prepregs, where, for both cases, impregnation does not present a problem. The effect of neat PAN interleave on G1p was explored, and a mixed result of 15% deprecation [88] and 22% improvement [92] was found.

b. Nano-modified PAN veil

Nano-modifications included nanoparticles of aluminum oxide (Al_2O_3) [90] and CNTs [91,92], mixed in PAN's electrospinning solution, i.e., incorporated into the veil fiber. Compared to the baseline laminate, nano-modified PAN veils showed better overall performance depending on wt% of nano-reinforcement. Al_2O_3 nanoparticles improved FT by up to 47%, CNTs improved 6-27% in G1i and 45-77% in G1p [92]. Similarly, introducing CNTs in electrospun PAN fiber also improved the electrical conductivity (up to 50%) and thermal conductivity (~3×) of the laminate [91].

To summarize, neat PAN interleaves generally show a minor improvement but can be detrimental if impregnated with viscous resin. However, doping nano-reinforcements like Al_2O_3 or CNTs demonstrate a significant improvement as well as provide multifunctionality. This merit can probably be attributed to the nano-reinforcement delivered to the ply/ply interface by veil placement rather than PAN direct involvement.

2.2.5 Polycaprolactone

Beckermann et al. [26], Saghafi et al. [32], Cohades et al. [93], and Heijden et al. [94] reported the effect of polycaprolactone (PCL) veil for GFRP and CFRP laminates. A similar trend of higher FT for woven reinforcement is also noted for PCL interleaves.

Beckermann et al. studied several veil materials and found a correlation between Mode I FT and the ultimate elongation of the bulk polymer used to make the veil. Polyethersulfone (PES), polyamide-imide (PAI), PA66, and polyvinyl butyral (PVB) followed the trend, but PCL did not, despite its highest ultimate elongation (679-948%). Upon further investigation, it was found that the PCL veils melted during oven curing of laminate due to its low melting temperature. Thus, the primary toughening mechanism (plastic deformation-identified) was replaced by a phase-separated microstructure, leading to a slight improvement in toughness (up to 14%). Similarly, phase-separated microstructure where epoxy particles are surrounded by PCL matrix was identified as a toughening mechanism by Saghafi et al. and Cohades et al. Similarly, Beckermann et al. also noted a correlation between the Mode II FT and the tensile strength of the bulk polymer used to manufacture the veil. This correlation was followed by all the veils investigated. The tensile strength of PCL is low compared to PA66 (9 MPa vs. 85 MPa); hence, a minor improvement of 7% in Mode II toughness is noted in the PCL veil interleaved laminate (compared to 29-69% for PA66 veil). Similarly, a 24% improvement for PCL (vs. 68% of PA66) is also noted by [65]. It is noteworthy that the authors did not describe the effect of PCL melting in Mode II toughness.

Such an atypical behavior of the PCL veil was further investigated and obtained up to 94% improvement in Mode I fracture toughening [94]. It was noted that a room temperature pre-cure (before oven curing at 80°C) of laminate eliminates such atypical behavior and acts as a crucial step when the PCL veil is interleaved. The impact of such a step is not explored for Mode II experiments. It is worth mentioning that Heijden et al. used single- and double-layer PCL as interleaves, increasing the net areal density of the veil.

Cohades et al. assessed the possibility of using the PCL veil for toughening and healing the cracks. Thermal treatment at 150°C was applied for 30 minutes to the cracked specimens to assess the capability of PCL to bleed, flow, and bridge the cracked faces, thus healing the cracked laminate. However, such healing was not observed because of the high viscosity of high-molecular-weight PCL, used in this study, with the required healing time of ~100 hours for fine nanostructure of pores vs. 30 minutes applied in tests. The authors concluded that self-healing properties could be achieved either by increasing the diameters of nanofibers, which, however, may compromise the FT, or by decreasing viscosity with the application of the low molecular weight PCL. However, in this case, the electrospinning becomes unstable due to low molecular entanglement.

These analyses show that PCL interleaves provide only mild improvements compared to other polymers, so they are not recommended for structural applications. Although a room temperature pre-cure removes PCL atypical behavior, such effects are not studied for Mode II.

Summarizing the comparative analysis, the introduction of the polymeric nanofiber veil improves the overall FT, with some exceptions. The comparison of attainable FT by interleaving these veils is plotted in Figure 2.2. These are cloud point plots of four FT parameters plotted as Mode I vs Mode II for initiation FT in Figure 2.2a and Mode I vs Mode II propagation FT in Figure 2.2b. The mode lines are also added, which is discussed separately in Section 2.3.1. This plot can be used as a reference plot for material selection as per the FT requirement in the design of composite structures in engineering applications. For instance, for composite design anticipating a higher G1i and a moderate Mode II initiation fracture toughness (G2i), the PA veil is recommended. Similarly, for a higher G2i and a moderate G1i, the PET veil is recommended.

2.3 Comparative analysis

2.3.1 Mode ratio

The mode ratio $\left(\mathrm{m} = \frac{\mathrm{G2}}{\mathrm{G1}}\right)$ inherits the nature of the resin used in the composite. The introduction of an electrospun veil changes the overall behavior of the resin in the interlaminar region. For a baseline laminate, a low mode ratio close to unity is expected for ductile resins. In contrast, a much higher ratio is observed for brittle resins. Change in the ratio by interleaving depends on the change in the individual properties, which further depends on the type of veil, its areal density, and production method, as noted in Section 2.2.

Figure 2.2 shows the initiation and propagation FT of the baseline and interleaved composite laminates. The scatter of points for baseline vs. interleaved laminates indicates the change in resin at the interlaminar region due to the addition of an electrospun veil in the interlaminar region of the laminate. The FT of baseline laminates concentrates near the bottom left corner of the plot in contrast to the FT of interleaved laminates which is distributed throughout. The highest Mode I initiation and propagation FT is noted for laminate interleaved with the PA veil, whereas the highest Mode II initiation and propagation FT is noted for laminate interleaved with PPS and PET-CF hybrid veil, respectively.

Similarly, adding mode ratio (m = 1…32) lines shows some other characteristic behaviors. For instance, the initiation FT of baseline laminates lies between mode ratios of 1 to 16 and most of the values concentrate around a mode ratio of 4, whereas the propagation FT of baseline laminates lies between mode ratios of 1 to 8 and most of the values concentrate between mode ratios of 2 and 4. Similarly, with interleaved laminates, the mode ratio reaches up to more than 32 for initiation FT and more than 16 for propagation FT.

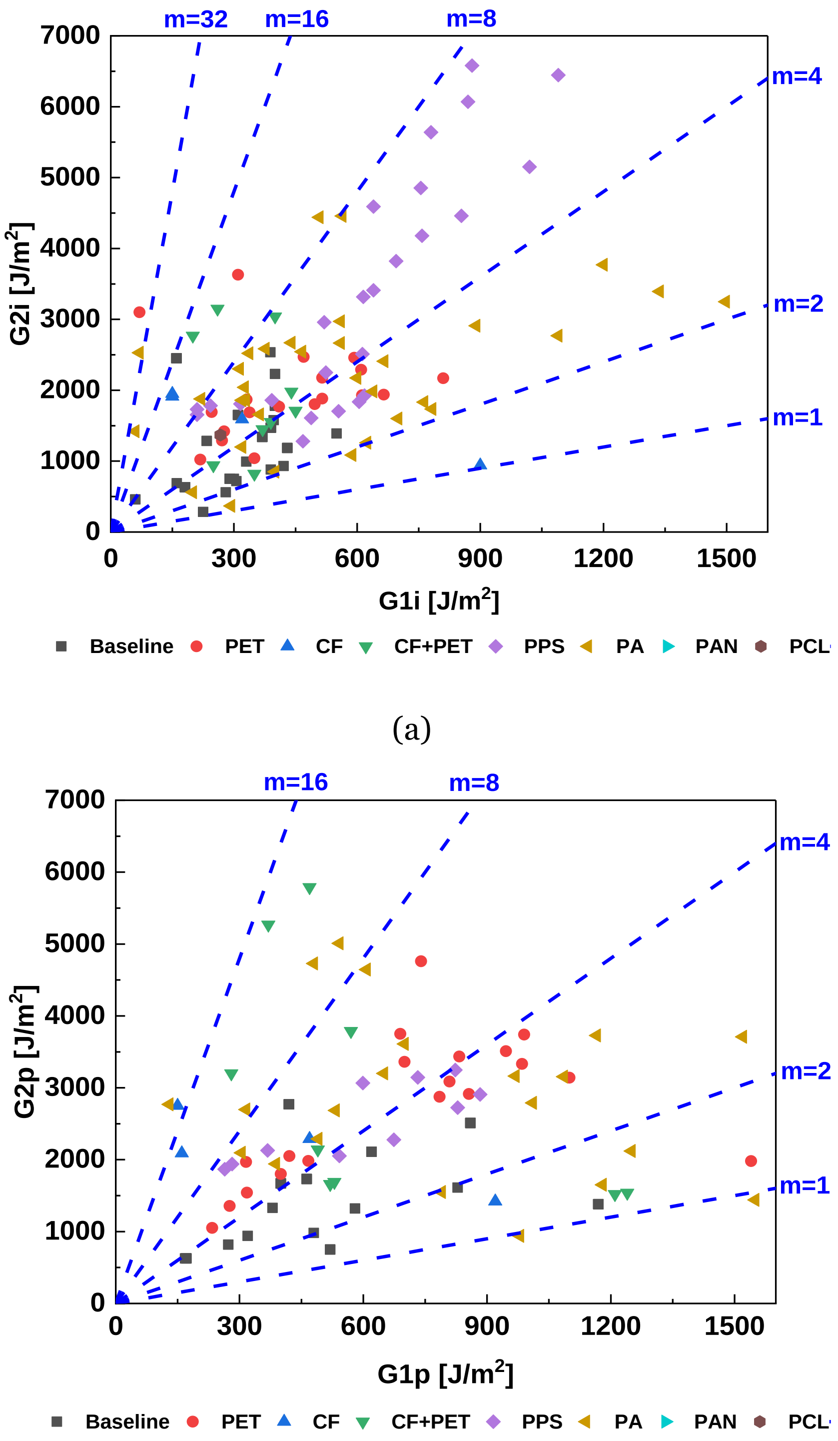

(a)

(b)

Figure 2.2. Mode ratio for (a) initiation and (b) propagation FT for baseline vs. interleaved laminate.

2.3.2 Areal density

Further, the zero areal density indicates the baseline laminate, and the non-zero areal density indicates the laminate is interleaved with a veil. The minimal, mean, and maximal areal density values are 0, 10, and 40 g/m², respectively. The correlation between veil areal density and FT, as presented in Table 2.1, shows a positive correlation between the four FT parameters and areal density. Mode II FT is more strongly correlated with the areal density ($r > 0.5$) than Mode I FT ($r < 0.5$). Figure 2.3 plots the cloud of points of initiation and propagation FT for Mode I and Mode II for UD CF laminates when interleaved with an electrospun veil produced with various materials and areal densities. The denser cloud of points in Figure 2.3a and Figure 2.3c shows an extensive research has been carried out to study the interleaving effect on initiation energy. However, only limited research focused on measuring propagation FT (applicable to both modes). The maximal attainable value of G1i is ~1600 J/m², G1p is ~1600 J/m², G2i is ~7000 J/m², and Mode II propagation fracture toughness (G2p) is ~6000 J/m².

PA has been identified as the most common choice of polymeric material for interleaving based on the reported number of data points shown in Figure 2.3. The various variants of modification of these materials are also used. These modifications include coating/doping with nano-reinforcement like CNT, GNP, metal modification/plating, and mixing one with other polymeric materials or CF. Such modifications of the veil add a new feature, making the veil multifunctional. A broad range of areal density has been investigated for PA interleaves, which shows a stable interleaving effect on improving FT. However, such a wide range of studies are missing for other veil materials.

Table 2.1 Correlation between areal density and FT

	G1i	**G1p**	**G2i**	**G2p**
Correlation coefficient (*r*)	0.44	0.34	0.59	0.58

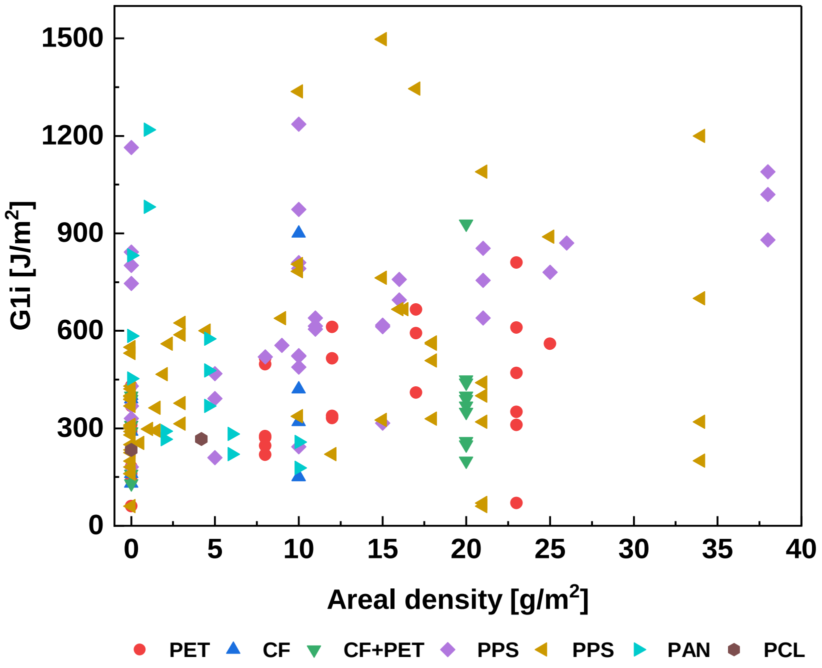
G1i [J/m^2]
1500
1200
900
600
300
0
0
5
10
15
20
25
30
35
40
Areal density [g/m^2]
PET
CF
CF+PET
PPS
PPS
PAN
PCL

(a)

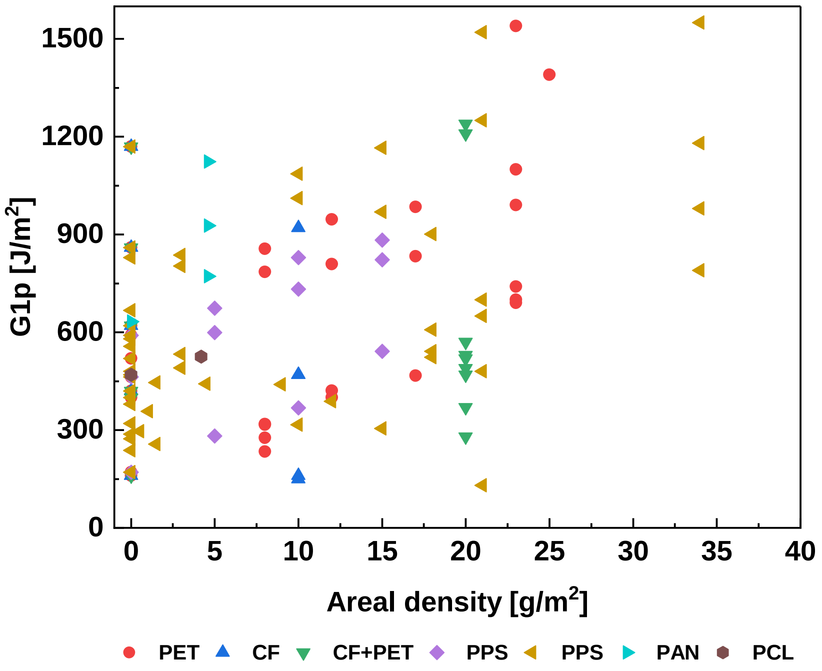
G1p [J/m^2]
1500
1200
900
600
300
0
0
5
10
15
20
25
30
35
40
Areal density [g/m^2]
PET
CF
CF+PET
PPS
PPS
PAN
PCL

(b)

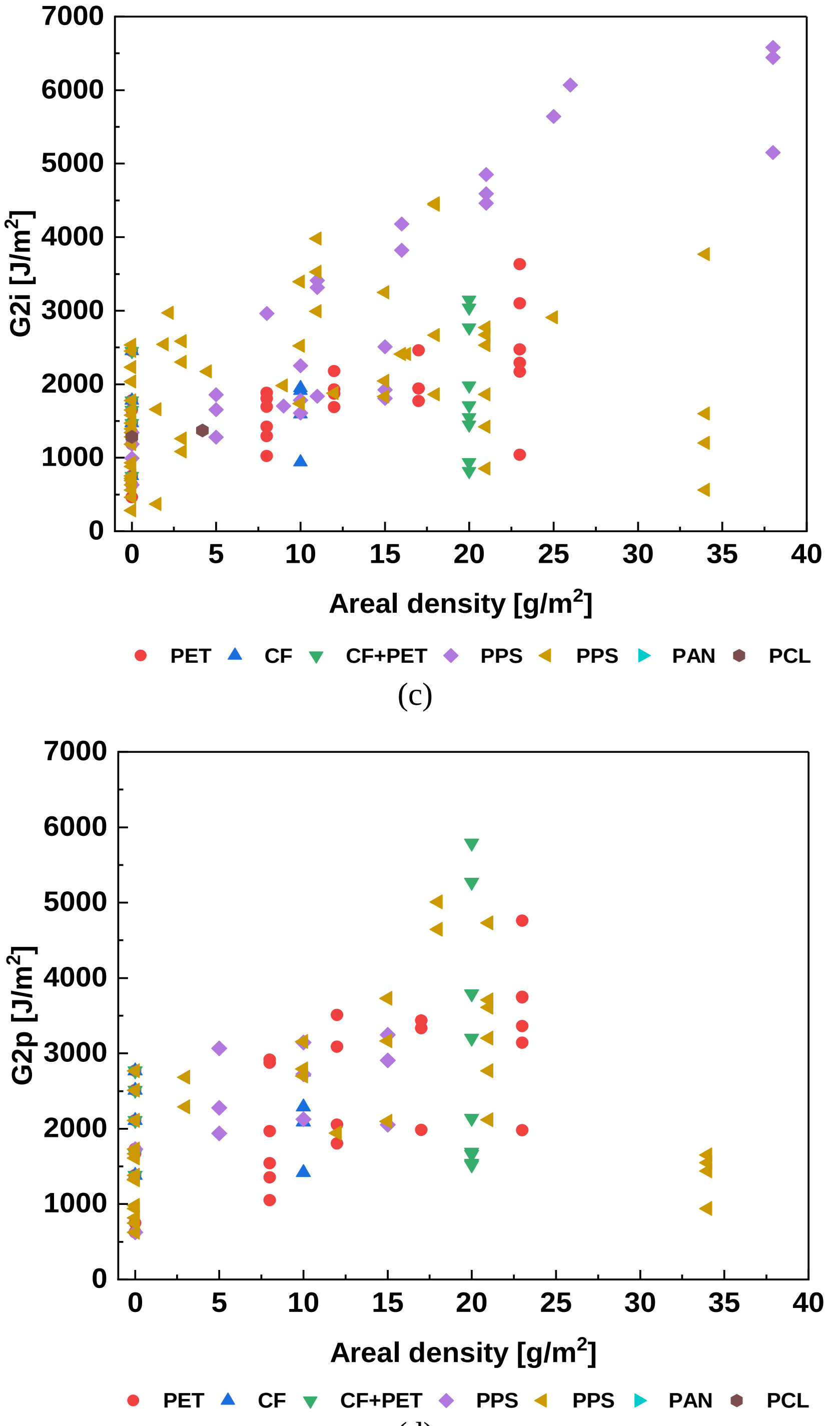

(c)

(d)

Figure 2.3. Dependence of (a) G1i, (b) G1p, (c) G2i, and (d) G2p on areal density for various veils.

2.4 Toughening mechanism

Cracks propagate in FRP laminates through the epoxy-rich areas, like the interlaminar region, resin pockets, etc. The brittle nature of the epoxy aids such crack propagation. However, interleaving the laminates with veils results in non-linear fracture patterns. This change is brought on by several toughening mechanisms added by the veil to the resulting laminates. Nanofiber bridging or crossings, nanofiber pull out and debonding, nanofiber plastic deformation and breakage, crack pinning, crack deflection, strong adhesion bond between the resin and veil due to compatibility or by melting the veil, and fusion bonded dots are the toughening mechanisms identified. (Fusion-bonded dots are semi-spherical dots formed by melting the veil at regular locations within the veil, which resists the crack propagation and improves the FT.) Some of these toughening mechanisms are shown in Figure 2.4. Doping veils with nano-reinforcements complicates the aforementioned behavior mostly by changing veil/resin adhesion, delivering nano-reinforcement to the fracture zone, and modifying functional properties of the laminate, like conductivity.

The nanofiber bridging or crossing formed by the nanofibers composing the veil is identified as the most common toughening mechanism. The nanofibers bridge the two laminae on the opposite sides of the veil, resisting the crack initiation and delaying propagation. Upon further loading, the nanofiber is pulled out of the epoxy, inducing the debonding. It is followed by nanofiber plastic deformation and nanofiber breakage. These toughening mechanisms consume a lot of energy, resulting in an increase in the overall FT of interleaved laminates. The effectiveness of the nanofiber bridging toughening mechanism depends on proper load transfer to the nanofibers. Crack propagation under Mode II loading resulted in much higher improvements than under Mode I loading due to the alignment of the loading with the nanofiber direction in the veil plane. In Mode I crack propagation, the loading of the nanofibers is less optimal and is shown to be dependent on both the primary reinforcement fabric architecture and the presence of a reinforcement fiber bridging zone.

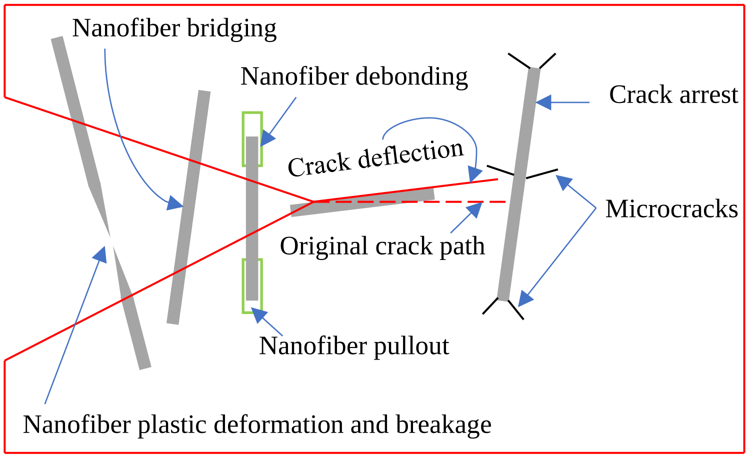

Figure 2.4. Schematic diagram of the toughening mechanism identified in interleaved laminates.

Crack pinning and crack deflection are also observed as the toughening mechanism that consumes energy, improving the toughness. Crack deflection and delamination migration occur when a strong adhesion bond is formed between the lamina and the veil due to material compatibility or plies orientations. Materials compatibility can be observed in its neat form or by phase change noted during curing for meltable veils.

2.5 Experiments

The production of the PAN veil loaded with various CNTs weight percentages and scanning electron microscopy (SEM) characterization, as presented in Section 2.5.1 and Section 2.5.2, were conducted at the Faculty of Mechanical Engineering, Budapest University of Technology and Economics by our collaborators (Prof. Kolos Molnar and Dr. He Heijun). The areal density and conductivity tests, as presented in Section 2.5.3 and Section 2.5.4, were performed at the laboratory of micro- and nano-mechanics, Skolkovo Institute of Science and Technology, Russia.

2.5.1 Production of CNTs modified PAN veil

PAN powder was dissolved in dimethyl-formamide (DMF) (Molar Chemicals, Hungary) to prepare a polymer solution for electrospinning. Bayer Baytubes C 150 HP MWCNTs were used as an additive to increase the conductivity of nanofibers. Before preparation of MWCNTs loaded PAN solution, 2 wt% MWCNTs (relative to PAN) were added into the DMF, and the mixture was sonicated for 15 minutes with an ultrasonic homogenizer (Bandelin Sonoplus HD 2200, Bandelin, Germany) to make MWCNTs dispersed homogeneously dispersed in DMF. Following that, PAN and extra DMF were added into the MWCNTs dispersion to prepare a solution loaded with different MWCNTs contents (i.e. 0.5, 1.0, 2.0, 4.0, 5.0%). At last, the prepared solutions were placed onto the oscillating board of a laboratory shaker and shaken with a speed of 120 rotations per minute (RPM) for 10 hours at ambient temperature for perfect dissolution. Before the solutions were to be used for electrospinning, they were sonicated again for 30 sec.

Figure 2.5. Baking paper used for collecting nanofibers (left), and 5 wt% MWCNTs loaded PAN veil collected on baking paper (right).

Electrospinning was performed by a vertical single needle (inner diameter 1.2 mm) setup, as shown in Figure 2.1. A drum with a rotation speed of 100 RPM was used as a collector. MA2000 NT 65/P (Hungary) type high voltage power supply was used for the experiments. The applied voltage and the distance between the grounded collector, and the spinneret were set to 25,000 volts and 190 mm, respectively. The polymer solution was supplied by a syringe pump (Aitecs SEP-10S plus, Lithuania) with a constant feeding rate of 0.8 ml/h. The nanofibers veils were collected for 15 minutes on baking paper glued on the drum for easy peeling off, as shown in Figure 2.5. The produced veils are characterized as detailed in Section 2.5.2 – Section 2.5.4.

2.5.2 SEM images

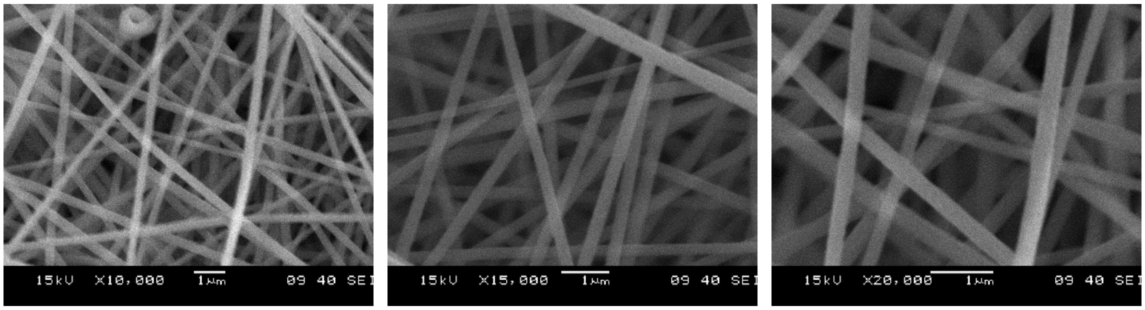

(a) (b) (c)

Figure 2.6. SEM image of PAN veil with 0.5 wt% MWCNTs at (a) 10K, (b) 15K, and (c) 20K resolution.

The PAN veils produced by electrospinning were observed under scanning electron microscopy (SEM) and the uniformity and continuity of the nanofibers were noted. The PAN veil without any addition of MWCNTs is presented in Figure 2.1 whereas, Figure 2.6, Figure 2.7, Figure 2.8, Figure 2.9, and Figure 2.10 show the SEM images of PAN loaded with different concentrations of MWCNTs at higher magnifications of 10,000×, 15,000×, and 20,000×. However, it should be noted that the nanofiber's constituents can't be distinguished even at a magnification of

20,000×. The diameter of nanofibers in the veil varied from ~200-500 nm with random nanofibers orientation.

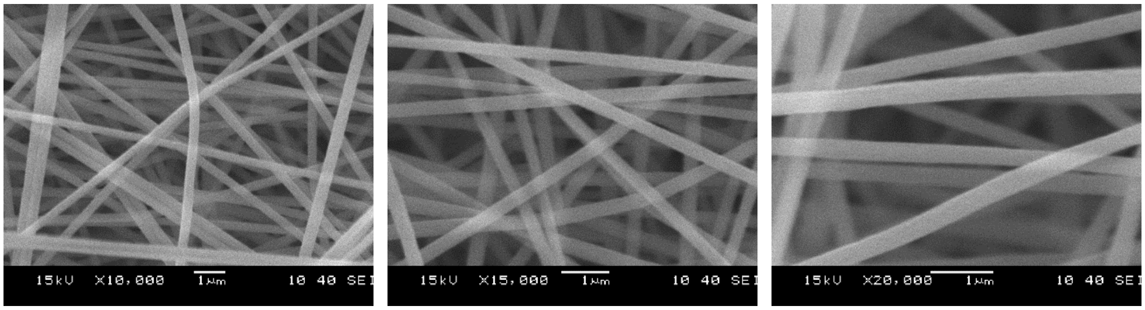

(a) (b) (c)

Figure 2.7. SEM image of PAN veil with 1 wt% MWCNTs at (a) 10K, (b) 15K, and (c) 20K resolution.

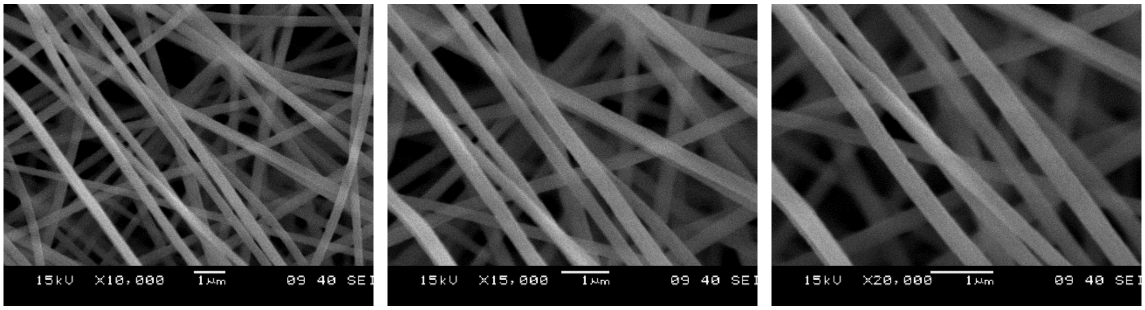

(a) (b) (c)

Figure 2.8. SEM image of PAN veil with 2 wt% MWCNTs at (a) 10K, (b) 15K, and (c) 20K resolution.

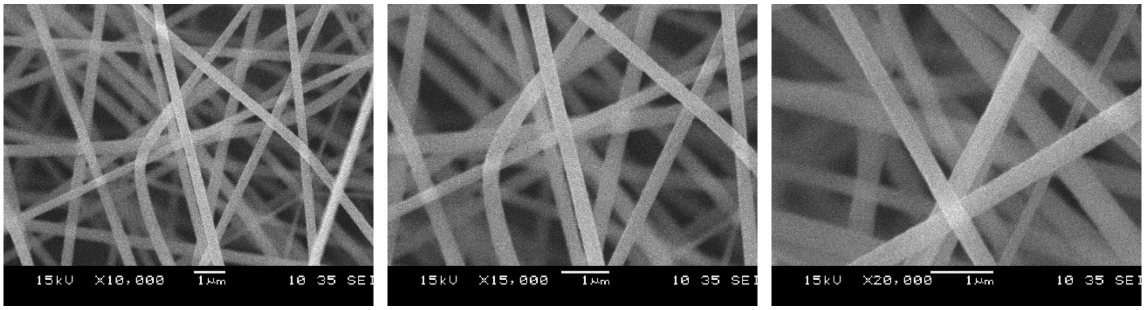

(a) (b) (c)

Figure 2.9. SEM image of PAN veil with 4 wt% MWCNTs at (a) 10K, (b) 15K, and (c) 20K resolution.

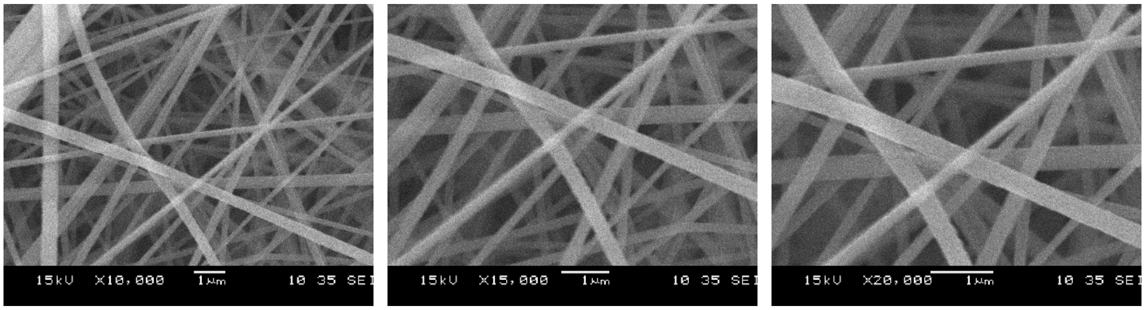

(a) (b) (c)

Figure 2.10. SEM image of PAN veil with 5 wt% MWCNTs at (a) 10K, (b) 15K, and (c) 20K resolution.

2.5.3 Areal density

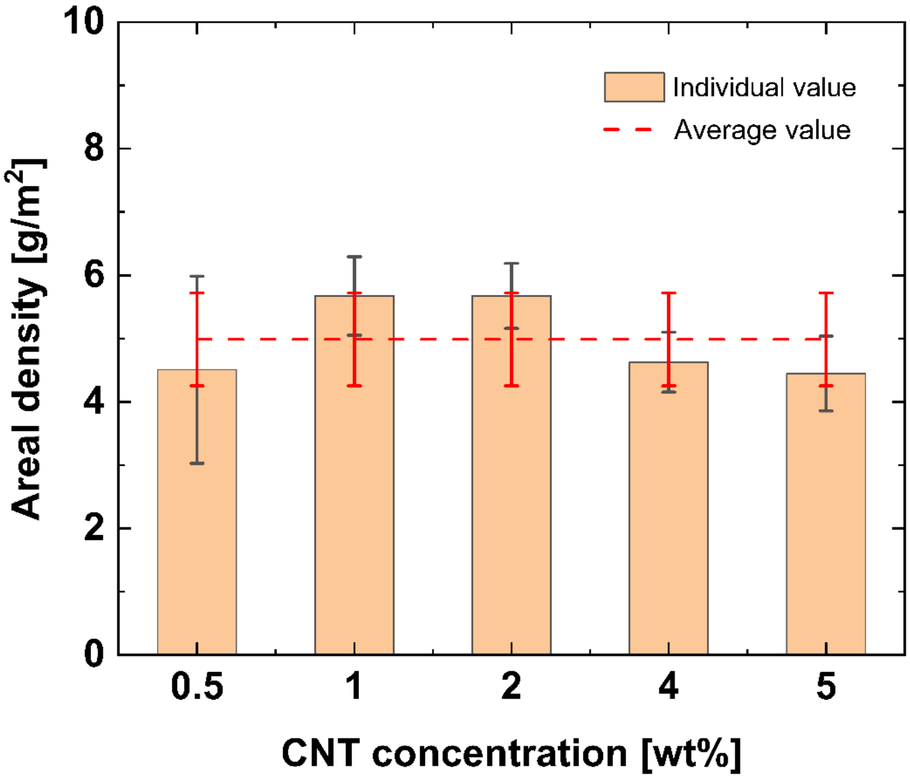

Figure 2.11. Areal density of PAN veil with different MWCNTs concentration and average value for comparison.

$$\text{Areal density} = \frac{\text{mass}}{\text{surface area}} \tag{2.1}$$

The mass of the PAN veil with baking paper and the mass of baking paper were measured to find the mass of the PAN veil. The surface area of the veil was measured before the veil was separated from the paper to maintain the initial form of the veil. Thus obtained mass of the PAN veil and surface area were considered to calculate the areal density of the veils using Equation (2.1). Figure 2.11 shows the areal density of different PAN veils and the global average value. The plot shows the average of each PAN veil is a close match with the global average of areal density of all veils.

Keeping manufacturing conditions constant, the nanofibers collection time of 15 min was used for all the veils, hence, the areal density is expected to remain the same for all the veils irrespective of MWCNTs wt%. As expected, the areal density of all veils is almost the same (~5 g/m^2), as shown in Figure 2.11.

2.5.4 Conductivity

Figure 2.12 shows the schematic diagram of the electrical conductivity test. The test was performed to measure the electrical conductivity of the veil obtained after the addition of MWCNTs in the PAN solution during its production. The electrical resistivity and surface electrical resistivity are defined as presented by Equation (2.2) – Equation (2.5). The surface electrical resistivity is defined as the ratio of electrical resistivity per unit thickness of the veil. Such measurements are useful when determining thickness is challenging because of non-uniformity or lower thickness value.

$$R = \frac{\rho l}{A} = \frac{\rho l}{wt} = \frac{\rho' l}{w} \tag{2.2}$$

$$\rho' = \frac{\rho}{t} = \frac{Rw}{l} \tag{2.3}$$

$$\sigma = \frac{1}{\rho} = \frac{l}{Rwt} \tag{2.4}$$

$$\sigma' = \frac{1}{\rho'} = \frac{l}{Rw} \tag{2.5}$$

where R is electrical resistance, ρ is electrical resistivity of material, ρ' is surface resistivity, σ is electrical conductivity, σ' is surface electrical conductivity, and the geometrical parameter (l, w, t, A) are defined in Figure 2.12.

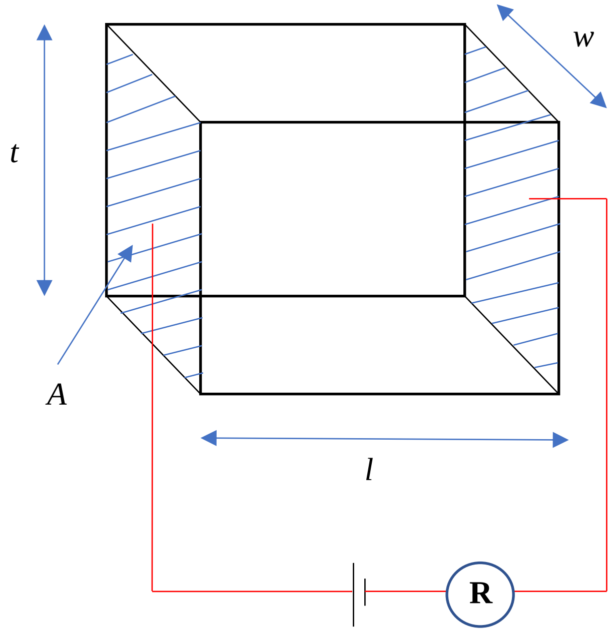

Figure 2.12. Schematic diagram of electrical conductivity test.

Four different trials were implemented to calculate the electrical conductivity of the PAN veils as,

a. Trial 1

On the surface of the PAN veils, 5 to 10 points were marked 10 mm apart in both length and width direction at the edge. The resistance between each marked point was measured using the two-point method with the help of probes connected to a Tektronix™ Keithley digital multimeter (DMM) capable of measuring resistance ranging from milli-Ohms to mega-Ohms; however, no change in electrical resistance reading was observed between any two marked points. Similarly, it was repeated for smaller distances between the marked points. These tests were repeated for all the samples (0.5…5 wt% MWCNTs); however, no sample showed any sign of electrical conductivity.

It was suspected that the conductivity was not being registered because of loose contact between the probe contact point and the veil's surface; hence, trial 2 was proposed.

b. Trial 2

In trial 2, 10 mm×10 mm samples were cut from the veil for all kinds of MWCNTs weight percentages. The silver paste was used to make contact points near the two opposite edges of the rectangular samples. It was cured at 60°C for 2 hours to dry the silver paste. It was followed by the measurement of resistance using the same method described in trial 1. The resistance of silver contact points was also measured to check if such contact points were made correctly. The resistance value of milli-Ohms was noted for each of the silver paste contact points. However, no conductivity was observed between the two silver contact points.

It was suspected that the conductivity was not being registered because of loose contact among the nanofibers; hence, trial 3 was proposed.

c. Trial 3

The veil with paper of size 40 mm×40 mm was pressed up to 5 bars using an Instron machine in compression mode to remove the loose contacts between the nanofibers in the veil, as shown in Figure 2.13. The resistance between two marked points 10 mm apart was measured using the method described in trial 1.

No electrical conductivity was noted between these marked points or any two points between the marked points.

It was suspected that the compression was not enough or paper on the bottom of the veil prevented the veil from being compressed enough, so new methods were proposed, as in trial 4.

d. Trial 4

The veil of size 40 mm×40 mm separated from the veil-baking paper system was pressed up to 5 bars using an Instron machine in compression mode. The compression load was released and with the compression metallic blocks resting on top of the veil, as shown in Figure 2.13, the resistance between the two metallic blocks was measured. No electrical conductivity was registered. However, the edges of the metallic plates touched one another, leading to a short circuit in one experiment. So, a metallic piece of thickness larger than the veil was placed in between the veil and the top metallic block, as shown in Figure 2.13. It was placed to remove the possibility of a short circuit due to edge contacts. The conductivity was measured for this configuration, resulting in no sign of electrical conductivity.

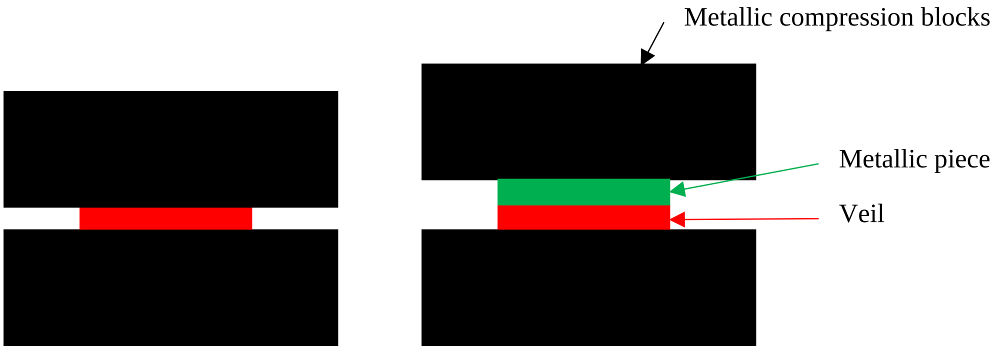

Figure 2.13. Schematic representation of compression of PAN veils for trial 3 (left) and trial 4 (right).

The desired electrical conductivity needed for damage sensing and monitoring application as detailed in Section 1.2.1 was not achieved even with 5 wt% MWCNTs. The reason could be that the MWCNTs did not form the percolating network in the nanofiber or between the nanofibers in the PAN veil. Hence, a new idea to fabricate a veil/interleave of CNTs independent of a polymeric veil was proposed and studied, as detailed in Chapter 3.

2.6 Conclusion

Interleaving polymeric veil has been proven to be one of the effective methods for improving the FT of composite laminate. There are several material choices for polymeric veil production. Amongst them, a few of the widely used materials are reviewed based on the FT they added over the baseline laminate so that the suitable material needed for the designed laminate can be chosen, as presented in Section 2.3. The toughening mechanisms are also identified and detailed in Section 2.5. This review was published as a review article and the details regarding the published paper can be seen in Section 2.7.

However, the goal set for this thesis research was not only to improve the FT but also to have an additional functionality enabling structural health monitoring. The electrical conductivity necessary for structural health monitoring was not achieved even after the addition of up to 5 wt% of MWCNTs in the PAN polymeric solution.

2.7 Publication

The research results were published as a journal article in the Polymers Journal as,

B. Mahato, S.V. Lomov, A. Shiverskii, M. Owais, and S.G. Abaimov, A Review of Electrospun Nanofiber Interleaves for Interlaminar Toughening of Composite Laminates, Polymers, 2023, doi.org/10.3390/polym15061380.

The authors’ contributions to this journal article are as follows: Conceptualization, B.M., S.V.L. and S.G.A.; methodology, B.M., S.V.L. and S.G.A.; software, B.M.; validation, B.M., S.V.L. and S.G.A.; formal analysis, B.M.; investigation, B.M.; resources, B.M.; data curation, B.M.; writing—original draft preparation, B.M.; writing—review and editing, B.M., S.V.L., A.S., M.O. and S.G.A.; visualization, B.M.; supervision, S.V.L. and S.G.A.; project administration, S.G.A.; funding acquisition, S.G.A.; corresponding authors, B.M. and S.G.A.

Chapter 3

Carbon Nanotubes Masterbatch Interleave

In this research, a nanoscale interlaminar modification by industrially available SWCNTs masterbatch is explored to solve the identified problems of microscale modifications as well as to maintain a promising result like as previously obtained, or even better, by the above-mentioned nanoscale modification methods while addressing their limitations. A CNTs interleave produced by diluting the SWCNTs masterbatch is introduced in between the plies in the interlaminar region to delay the delamination of the glass/epoxy composite laminate. The interleave is produced by painting the diluted masterbatch on the prepreg. This NsM method is expected not only to delay the delamination and improve the Mode I fracture toughness but also to improve the conductivity of the laminate. The latter changes with the change in the crack length and such self-diagnostic ability can be used to *in-situ* monitor the state of the crack in the laminate, hence giving the possibility of structural health monitoring. The interleave is applied as an additional layer to the laminate, so the nano-filler filtration problem is entirely skipped because CNTs are not mixed in the bulk matrix. Similarly, this method of introducing the CNTs layer into the laminate can be easily scaled, as the applied SWCNTs masterbatch is available on the industrial scale now. In addition, working with masterbatch grants comparatively safer handling and cleaner production, as the CNTs are pre-dispersed in epoxy. Additionally, masterbatch delivers mixing consistency, process stability through better pre-dispersion of CNTs and increases CNTs stability. Table 3.1 lists the factual data on the effect of CNTs on Mode I fracture toughness of the composite laminate, as discussed in Section 1.2.1.

Table 3.1. Effect of CNTs on Mode I fracture toughness.

Modification method	Materials	CNTs content [wt%]	Mode I Fracture toughness		Ref.
			Value [J/m^2]	Change over baseline* [%]	
Fiber modification (FM)	Short fuzzy aligned CNTs on reinforcing alumina fibers and aerospace epoxy	0.5	140 ± 10	- 61%	[40]
	Long fuzzy aligned CNTs on reinforcing alumina fibers and aerospace epoxy	2	250 ± 100	- 29%	
	Short fuzzy aligned CNTs on reinforcing alumina fibers and marine epoxy	0.5	710 ± 250	+ 22%	
	Long fuzzy aligned CNTs on reinforcing alumina fibers and marine epoxy	2	830 ± 320	+ 43%	
Resin modification (RM)	Modified epoxy with SWCNTs	0.5	396.4 ± 30	- 46%	[41]
	Modified epoxy with neat CNTs	0.5	216 ± 70	- 13%	[95]
	Modified epoxy with plasma treated CNTs	0.5	356 ± 52	+ 40%	
	Modified epoxy with MWCNTs	0.5	1175	+ 25%	[96]
		1.0	1132	+ 20%	
		1.5	1102	+ 17%	
Prepreg/Fabric modification (PM)	Spray coating CNTs on prepreg	0.02	454	+ 22%	[42]
		0.05	542	+ 46%	
	Air-brush spray of CNTs on fabric	0.05	270.9	+ 50%	[97]
		0.1	268.3	+ 48.5%	
		0.5	94.8	- 47.5%	
	3D stitching the fabric with CNTs belt	2.3	495.3	+ 129%	[98]
	Electrospray deposition of CNTs on fabric	0.4	1277.5	+ 32%	[99]
Interlaminar region modification (IRM)	Polyethersulfone-carbon black film in interlaminar region	2.5	346.2	+ 67%	[45]
		5.0	356.5	+ 72%	
		7.5	413.5	+ 99%	
		10.0	307.4	+ 48%	
	Vertically aligned CNTs in interlaminar region	1.4	530	+ 150%	[30]

	Porous interleaves of CNTs and polyethylene-comethacrylic acid	3.3	540 ± 60	+ 67%	[100]
	Highly aligned CNTs in interlaminar region	1.4	338 ± 96	+ 61%	[101]

* '+' means increase and '-' means decrease in property.

3.1 Materials

Table 3.2 Details of SWCNTs masterbatch taken from the supplier technical datasheet.

Type	Supplier	CNT			wt%	Production method	Purity	
		Length [µm]	Outer Diameter [nm]	Estimated aspect ratio (L/D)			%	Evaluation method
SWCNT	Tuball 301, OCSiAl	≥ 5	1.6 ± 0.4	2500-4200	10	Three roll milling	≥ 93	TEM, EDX, Ash residue

CP002 unidirectional glass fiber prepreg of areal density 250 g/m^2 was used for manufacturing the composite laminate. Two types of SWCNTs interleaves containing 0.6 wt% of SWCNTs and 7.5 wt% of SWCNTs were produced by diluting the industrially available SWCNTs masterbatch (MB), characteristics are given in Table 3.2. These interleaves are further designated as low-concentration (LC) interleave and high-concentration (HC) interleave for their low and comparatively higher concentration of SWCNTs in the interleave, respectively. The details of industrial masterbatches are tabulated in Table 3.2. The aspect ratio is estimated based on the datasheet offered by the suppliers. Masterbatch was diluted with a bisphenol A diglycidyl ether (DGEBA) based epoxy, EPOLAM 2031TM, to the necessary weight percentage. EPOLAM 2031 is compatible with the DGEBA-based epoxy in the masterbatch. EPOLAM 2031 offers a low viscosity, which is suitable as the net viscosity increases with the addition of nano-fillers like SWCNTs. No additional solvents or dispersants were used other than the EPOLAM 2031 hardener compatible with the epoxy in the interleave. Similarly, HC interleave was produced by mixing the masterbatch with acetone and a compatible hardener. The glass fiber prepreg, EPOLAM 2031 epoxy, and masterbatch were used as received.

Aluminum foil of thickness 13 μm played the role of a crack initiator and a cyanoacrylate-based lab superglue was used to attach the piano hinge to the DCB samples. The aluminum foil was modified by a coating of a release agent, Frekote 700.

3.2 Methodology

3.2.1 Fabrication of CNTs interleaves

The LC and HC interleaves were produced by mixing SWCNTs masterbatch with epoxy and SWCNTs masterbatch in acetone, respectively. Figure 3.1a shows the schematic representation of steps in the fabrication process. The details of the steps are available in Table 3.3. For the LC interleave, the production started with mixing the SWCNTs masterbatch with epoxy at low RPM at a slightly elevated temperature of 40°C and relative humidity of 30%. It was followed by vacuum degassing at a pressure of 0.01 mbar for 10 minutes to remove the air bubbles trapped in the materials during mixing. In step 2, the mixture was further mixed at high RPM for 60 minutes with the same temperature and humidity conditions. These steps helped to achieve uniformity in the distribution of SWCNTs in the mixture. It was followed by the second crucial vacuum degassing step to remove the air bubbles trapped during the long turbulent mixing. In step 3, the hardener was added and mixed at low RPM with no heating for 10 minutes followed by 15 minutes of vacuum degassing to remove remaining air bubbles, if any. In this step, heating is prevented from avoiding the triggering of the epoxy cure kinetics. After this, the mixture was ready to be introduced in between the plies in the composite laminate to form the LC interleave.

Similarly, for HC interleave, production started with mixing SWCNTs masterbatch in acetone at low RPM with no heating for 20 minutes in 1:1 ratio. Vacuum degassing was applied at a pressure of 0.01 mbar for 10 minutes to remove the air bubbles trapped in the materials during mixing. The obtained mixture was kept as it is for 24 hours at a room temperature of 25°C and relative humidity of 30%. To this mixture, the hardener was added and mixed at low RPM with no heating for 10 minutes and vacuum degassed for 15 minutes to remove any air bubbles trapped in the mixture. The mixture was ready to be introduced in between the plies in the composite laminate to form the HC interleave.

Table 3.3. Steps for fabrication of interleaves.

Interleave type	Materials	Step 1		Step 2		Step 3		
LC interleave	Epoxy + MB	Low RPM Heating (40°C) 20 min.	10 min of vacuum degassing	High RPM Heating (40°C) 60 min	15 min. of vacuum degassing	Add hardener	Low RPM No heating 10 min	15 min of vacuum degassing
HC interleave	MB + Acetone	Low RPM No heating 20 min		24 hours resting period at room temperature			Low RPM No heating 10 mins.	

Table 3.4. Constituents of interleaves by concentration and amount.

Interleave type	MB [g]	Epoxy [g]	Hardener [g]	Acetone* [g]	Concentration of MB in interleave [wt%]	Concentration of SWCNTs in interleave [wt%]
LC interleave	15.0	183.7	51.3	-	6	0.6
HC interleave	15.0	1.2	3.8	20	75	7.5

*Acetone was evaporated during resting time, as detailed in Section 3.2.2, so it is not considered in wt% calculation.

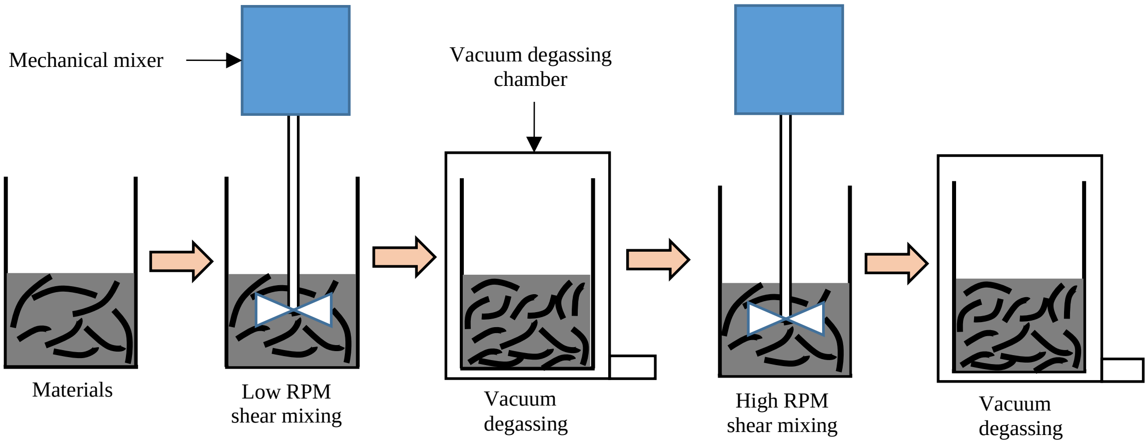

(a)

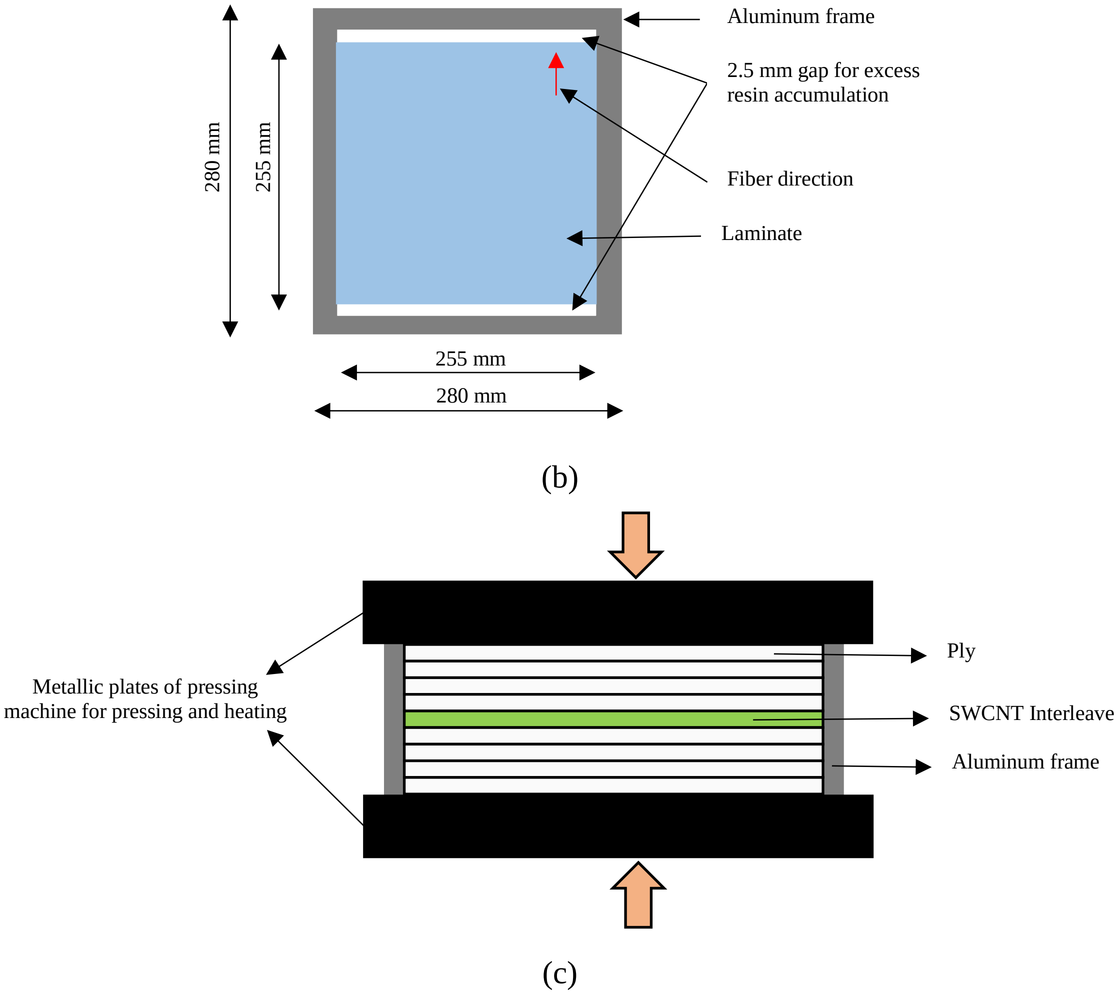

Figure 3.1. Schematic representation of (a) mixing masterbatch to produce interleaves, (b) metallic frame placement for fabricating the laminate, and (c) pressure application during manufacturing.

Table 3.4 shows the constituents of both LC and HC interleaves by their concentrations and the amount in the bulk of the interleave mixture prepared. Weights are given only for reference to how the mixture was prepared and should not be counted as applied to the laminate.

3.2.2 Fabrication of composite laminate

Composite laminates were fabricated by stacking 16 plies lay-up ($[0]_{8s}$) of unidirectional GF prepreg. The aluminum foil was placed in the middle plane between the 8th and 9th plies, which acted as the crack initiator in the DCB tests. The lay-up was covered with a polymer film (Melting point: 200°C) and hot pressed in the Collin™ pressing machine. The pressure and heat for manufacture were applied by the metallic plates of the Collin™ pressing machine, as shown in Figure 3.1c. The aluminum frame support, as shown in Figure 3.1b, was used. Section 3.2.6 shows detailed information about the aluminum frame and its effect on manufacturing.

For the fabrication of the interleaved laminates, the above method was slightly modified. Two stacks of glass fiber prepreg plies containing 8 plies each in $[0]_8$ lay-up were prepared. The interleave mixture was introduced on both prepreg stacks and distributed evenly with the help of a brush. The aluminum foil was placed on one of the prepreg stacks, followed by transferring the second stack on top of the aluminum foil. The transfer was done immediately for the LC interleaved laminate. Whereas, with HC interleaved laminate, the transfer was performed after a resting time of 3 hours at room temperature of 25°C and relative humidity of 30% under a fume hood. The resting time was chosen such that the remaining acetone in the HC interleave was evaporated. The transfer of the rest of plies was done, maintaining the continuity of unidirectionality of the prepreg.

The composite laminates were first visually inspected to see any possible physical damage. The laminate was cut into standard DCB samples of size as per ASTM D5528-01 [102] standard by the computerized numerical control (CNC) machine. The sides of the DCB sample were sandpapered to remove rough edges. The piano hinges were glued, and markings were made on the side face, painted with the white correction fluid. The markings were made with the help of a lab ruler so that the crack tip could be identified, and the crack length could be quantified easily during the DCB test. The aluminum foil remained as it was in the baseline laminate. However, in the interleaved laminates, the aluminum foil near the crocodile clip contact point was removed carefully with the help of the tweezer before the test. The aluminum foil near the crack tip remained as it was so as not to disturb the crack tip and initiation fracture toughness value measurement.

3.2.3 Manufacturing cycle choice

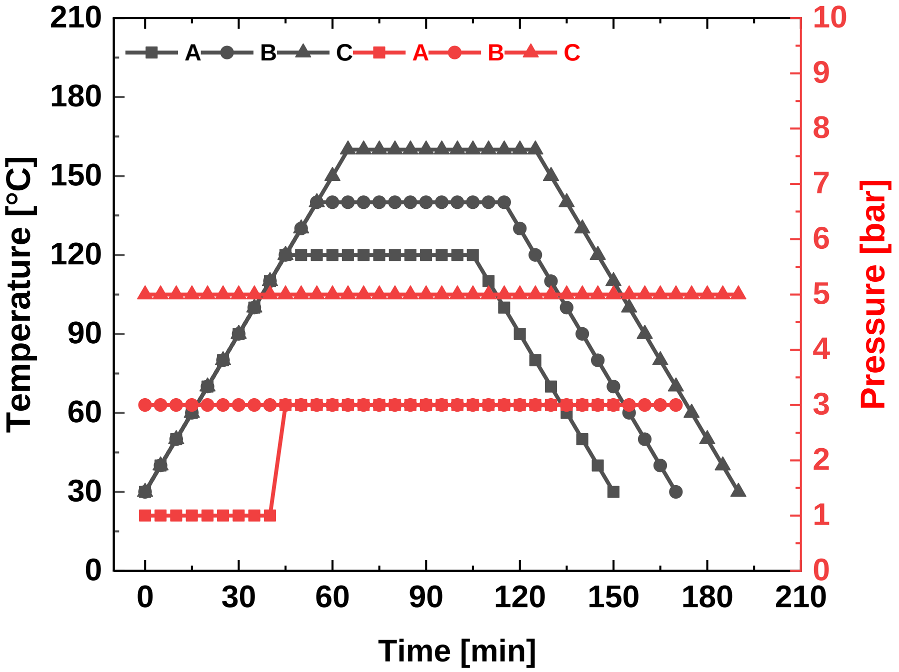

Figure 3.2. Different manufacturing cycles showing temperature and pressure for producing composite laminates.

Three combinations of maximal temperature and pressure, as shown in Figure 3.2, were considered for manufacturing of the composite laminate in the press. Three composite laminates (A, B, and C) were manufactured with the aluminum frame support with maximum temperatures of 120°C, 140°C, and 160°C and maximum average pressures of 2 bars, 3 bars, and 5 bars, respectively. The heating ramp of 2°C/min was applied in all cases until the maximum temperature was reached. It was followed by an isotherm dwell for 1 hour and cooling at a ramp of 2°C/min. Two types of pressure profiles over production time were designed.

The first pressure profile was a continuous maximal pressure applied at fabrication of laminate B and laminate C and the second pressure profile was a stepwise pressure applied at fabrication of laminate A, as shown in Figure 3.2. The effect of these manufacturing cycles (A, B, and C) on the quality of laminate is discussed in Section 3.2.4 and Section 3.2.5.

3.2.4 Effect of pressure and temperature

Laminate A manufactured by application of stepwise pressure applied during production time displays a lot of air bubbles trapped as shown on the C-scan, in Figure 3.3a, whereas such air bubbles were not observed in laminates B and C manufactured by application of continuous maximal pressure during fabrication. Henceforth, stepwise pressure cycles were discarded and continuous pressure cycle over production time was considered. Increasing the maximum applied pressure during the production of composite laminate increased the fiber volume fraction from ~48% at 2 bars to ~60% at 5 bars, as shown in Figure 3.3d. The fiber volume fractions of composite laminates were determined based on the measurement of thickness. Hence, the maximal continuous pressure of 5 bars was considered to produce laminates used in this study.

The effect of maximal operating temperature on the production of laminate can be observed in the quality of cure attained by the laminate, as detailed in Section 3.2.5. Similarly, based on the C-scan of laminates, areas of poor cure can be seen in laminates A and B, whereas such poorly cured areas are not visible in laminate C, as shown in Figure 3.3a-c. Hence, the maximal operating temperature of 160°C at a heating ramp of 2°C/min. and isotherm dwell of 1 hour, followed by a cooling ramp of 2°C/min, was selected as a temperature cycle to produce laminates.

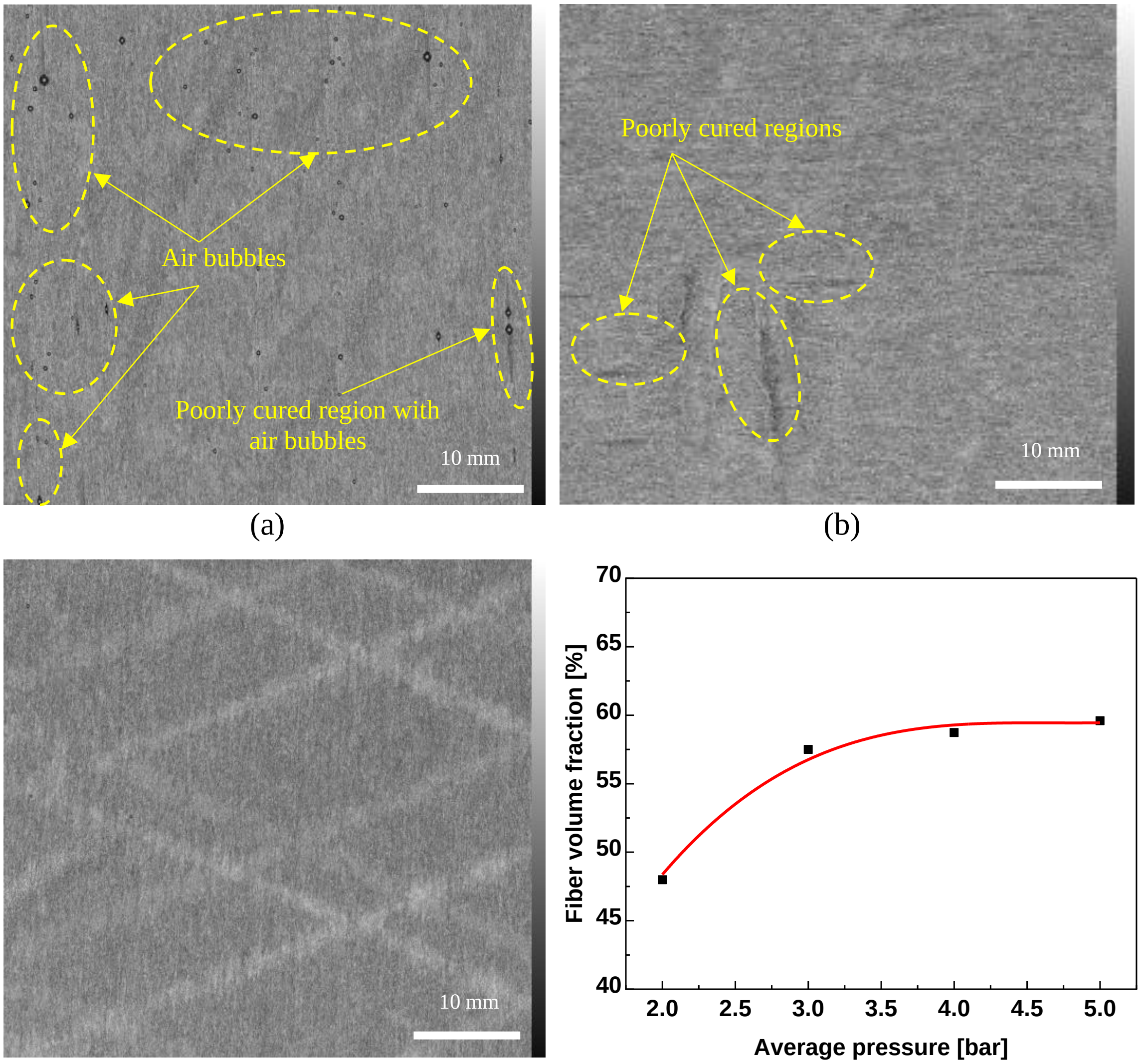

(a) (b)

(c) (d)

Figure 3.3. C-scan showing air bubbles and poorly cured regions in (a) laminate A (b) laminate B and (c) laminate C. (d) Fiber volume fraction attained at various pressures during manufacturing of composite laminate. The average value of applied pressure is considered in case of stepwise pressure.

3.2.5 Degree of cure

Figure 3.4 shows the degree of cure attained during three different manufacturing cycles (A, B, and C). The maximal degree of cure attained during curing cycle A was ~46% as compared to ~76% in curing cycle B and ~99% in curing cycle C. The way the degree of cure developed during the manufacturing cycle is plotted and shown in Figure 3.4. The common trait noted amongst all three manufacturing cycles was that the highest degree of cure was attained during the heating ramp until the maximal temperature was reached. In the isotherm dwell region, the curing is slower, and some curing takes place. The isotherm dwell region is important to set the whole laminate at the maximal isothermal temperature so that even the innermost part of the laminate reaches the set maximal temperature and cures as desired. Henceforth, cycle C was chosen to produce composite laminates.

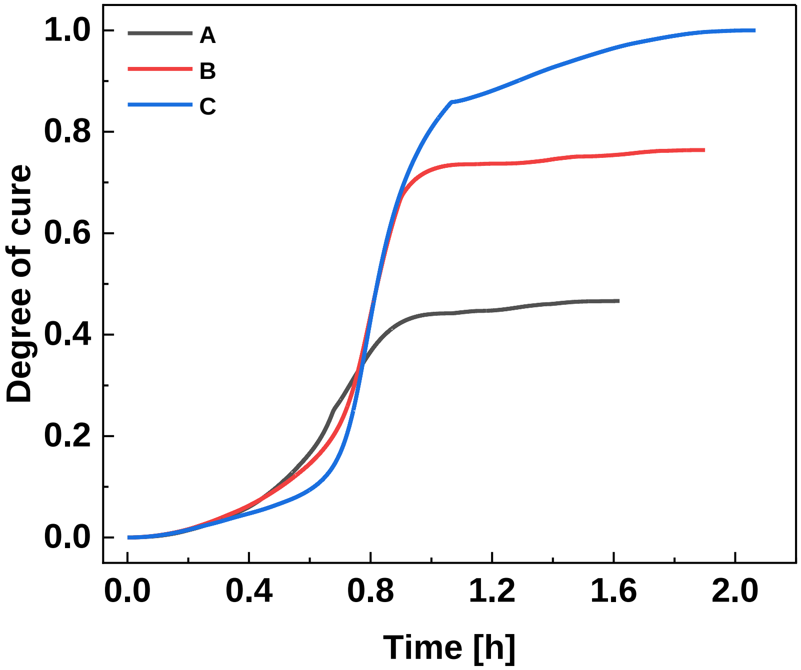

Figure 3.4. Degree of cure attained during various cure cycles.

3.2.6 Effect of the frame

The visual inspection of composite laminates manufactured with and without metallic frame support, as shown in Figure 3.5, shows the misaligned fibers on the sides of the laminate in the transversal direction for the laminate manufactured without metallic support. Such fiber misalignments were noted because the fibers were free to move (wash-out effect) when the epoxy in the prepreg reduced its viscosity during pressing. Such misalignments of fibers in laminates are not desired. Henceforth, the laminates were manufactured with the support of an aluminum frame of size 280×280×5 mm, as shown in Figure 3.1b. A gap of 2.5 mm was left between the prepreg and aluminum frame at both ends in the fiber direction, but no such gap was left in the transverse direction. The gap was designed such that the movement of fibers in the transverse direction was restricted and excess resin was collected in the fiber direction only. The thickness of laminate manufactured without aluminum frame support was ~2.0-2.3 mm, which changed to ~2.8 mm as displacement of fibers causing misalignment was restricted with aluminum frame. Hence, the selection of an aluminum frame thickness of 5 mm was suitable for the manufacture of laminates.

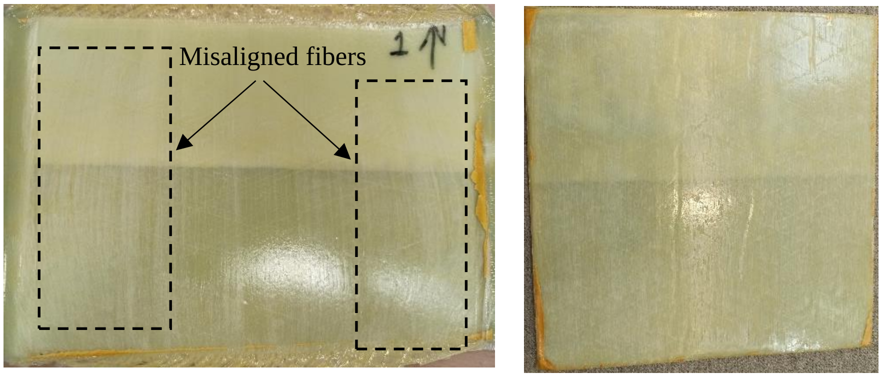

(a) (b)

Figure 3.5. Composite laminates fabricated by press molding the glass fiber prepregs (a) without frame support (laminate size: 200×300 mm), and (b) with aluminum frame support (laminate size: 255×255 mm). The arrow at the top right corner in (a) represents the fiber direction for both laminates.

3.3 Experiments

3.3.1 Scanning acoustic microscopy

The non-destructive C-scans of composite laminates, as presented in Section 3.2.4, were taken on the PVA TePla™ scanning acoustic microscope

(SAM301) to check the quality of the laminates manufactured. A transducer of frequency 20 megahertz (MHz) was used with a sample in the water medium at room temperature.

3.3.2 DSC test

Differential scanning calorimetry (DSC) tests were performed on the Shimadzu™ DSC-60 (TA instruments) to evaluate the degree of cure attained during the temperature-time heating cycles. To calculate the degree of cure, two DSC scanning cycles were run. In the first DSC scanning cycle, the uncured epoxy from the prepreg was subjected to the same temperature-time cycle to measure the isothermal heat flux. It included a heating ramp of 2°C/min reaching the maximal temperature of 120°C, 140°C, or 160°C, respectively, followed by the isotherm dwell of 1 hour. In the second DSC scanning cycle, the cured neat epoxy samples were considered and taken from the cured composite laminates for dynamic DSC scanning from 30°C to 300°C at a heating ramp of 10°C/min. The degree of cure growth with time, as presented in Section 3.2.5, was calculated using Equation (3.1), where α is the degree of cure, $\mathrm{H_{iso.}}$ is the heat of reaction measured during isothermal DSC scanning, $\mathrm{H_{total}}$ is the total heat of reaction considering the $\mathrm{H_{iso.}}$ as well as the residual heat measured in the dynamic DSC scanning, and t is time.

$$\alpha\ (\mathrm{t}) = \frac{\mathrm{H_{iso.}(t)}}{\mathrm{H_{total}}} \tag{3.1}$$

3.3.3 Mode I interlaminar fracture toughness test

The Mode I interlaminar fracture toughness test was conducted as the DCB test as per ASTM D5528-01 standard [102]. The displacement rate was 1 mm/min on Instron™ 5969 with a load cell of 1 kN. Five specimens were tested for each case. The test specimen was photographed using a Grasshopper™ GRAS-50SM-C camera at 6 frames per minute to determine the crack length. All three methods (modified beam theory (MBT), compliance calibration (CC), and modified compliance calibration (MCC)) of data reduction were considered for calculating the Mode I interlaminar fracture toughness in accordance with:

$$G_1^{MBT} = \frac{3P\delta}{2b(a + |\Delta|)} \tag{3.2}$$

$$G_1^{CC} = \frac{nP\delta}{2ba} \tag{3.3}$$

$$G_1^{MCC} = \frac{3P^2C^{\frac{2}{3}}}{2A_1bh} \tag{3.4}$$

where P is load in [N], δ is displacement in [mm], b is width in [mm], a is crack length in [mm], h is thickness in [mm], and Δ is correction determined by generating a least-square fit to the plot of $C^{1/3}$ vs. a. The compliance, C, is the ratio of load point displacement to the applied load, namely $\frac{\delta}{P}$. Similarly, n is the slope of the least-square fit to the plot of log C vs. log a, and A_1 is the slope of the least-square fit to the plot of $\frac{a}{h}$ vs. $C^{1/3}$. The results are discussed in Section 3.4.3 and Section 3.4.4.

3.3.4 ***In-situ* damage sensing and monitoring test**

The electrical connection between the DMM and the sample in the DCB test was done with the help of crocodile clips and copper wire. The 2-point electrical resistance and its change were measured by Keithley™ 6500 DMM for a sample at the DCB test as per the schematic diagram of *in-situ* damage sensing and monitoring test shown in Figure 3.6. The change in resistance with time depends on the interleave resistivity, its width, thickness, and length as given by,

$$R(t) = \frac{\rho\, 4\, L(t)}{w\, h} \tag{3.5}$$

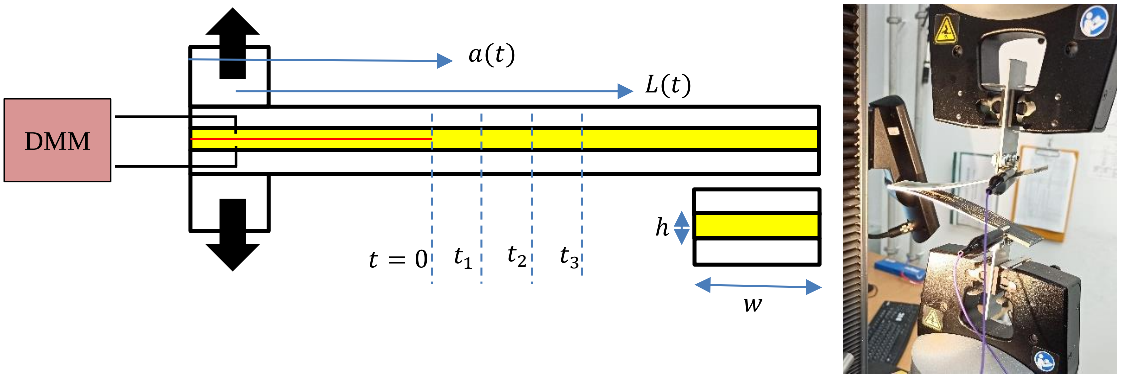

(a) (b)

Figure 3.6. Conductivity test during Mode I DCB test: (a) schematic diagram (b) experimental setup.

where ρ is the resistivity of interleave, L(t) is the effective length of the “arms” close to the crack length, which changes with time, w is the width, and h is the thickness. The length changed over time during the DCB test, hence the overall resistance measured also changed over time. Equation (3.5) assumes the exact halfway split of interleave thickness, which may not be representative in a case when the crack deflects the interleaves. Similarly, the resistivity of interleave may vary depending on the CNT content. Hence, Equation (3.7) is further deduced from Equation (3.5) by removing these unknown terms with a constant which depends on the initial values of resistance and length measured at the beginning of the test and calculated by Equation (3.6), with L(t) being not the exact crack length, but its effective length (taking into account the problem that we cannot predict whether the interleave will split into two equal halves or differently).

$$\text{At } t = 0;\ L(t) = L_0 \text{ and } R(t) = R_0;$$

$$\frac{\rho}{h} = \tilde{\rho} = \frac{R_0\, w}{4\, L_0} = \text{constant} \tag{3.6}$$

$$R(t) = \frac{\rho\ 4\ L(t)}{w\ \ h} = \frac{4\,L(t)}{w} \times \frac{R_0\ \ w}{4\,L_0} = \left(\frac{R_0}{L_0}\right) \times L(t) = K_0 \times L(t)$$

$$R(t) = K_0 \times L(t) \tag{3.7}$$

where t is time and $K_0 = \frac{R_0}{L_0}$ is a constant. Equation (3.7) demonstrates that if experimentally measured R(t) (and, together with it, the effective length L(t)) will have a near linear dependence on the observed crack size (Δa), then the predictive capabilities of the proposed method can be considered as acceptable. The results are discussed in Section 3.4.5.

The above-developed *in-situ* damage sensing and monitoring test model is a 1D model, as shown by Equation (3.5), for a standard DCB test coupon, so the electrical conductivity measured with the help of crocodile clips is sufficient. However, in case of complex composite structure or non-linear damage like in case of impact damage, a 3D model with multiple electrodes is suggested as noted in Ref. [103–105].

3.3.5 Fractography and microstructural analysis

Fractography and microstructural analysis were conducted on the Thermo Scientific™ Helios G4 PFIB scanning electron microscope. Fractography analysis was conducted to check and identify the toughening mechanism in the baseline and interleaved laminates. The analysis was performed on the fractured surface of the baseline laminate, LC interleaved laminate, and HC interleaved laminate samples after the successful completion of the DCB test. No additional treatment was applied to the fractured surface of LC and HC interleaved laminates. A gold plating was implemented on the fractured surface of the baseline laminate to make it electrically conductive. Similarly, microstructural analysis was performed to assess the dispersion quality of masterbatch in the interleaved laminates. The analysis was performed on the fractured interleaved surface of the LC interleaved laminate, HC interleaved laminate, and masterbatch for reference. The results are discussed in Section 3.4.1 and Section 3.4.6.

3.4 Results

3.4.1 Microstructural analysis

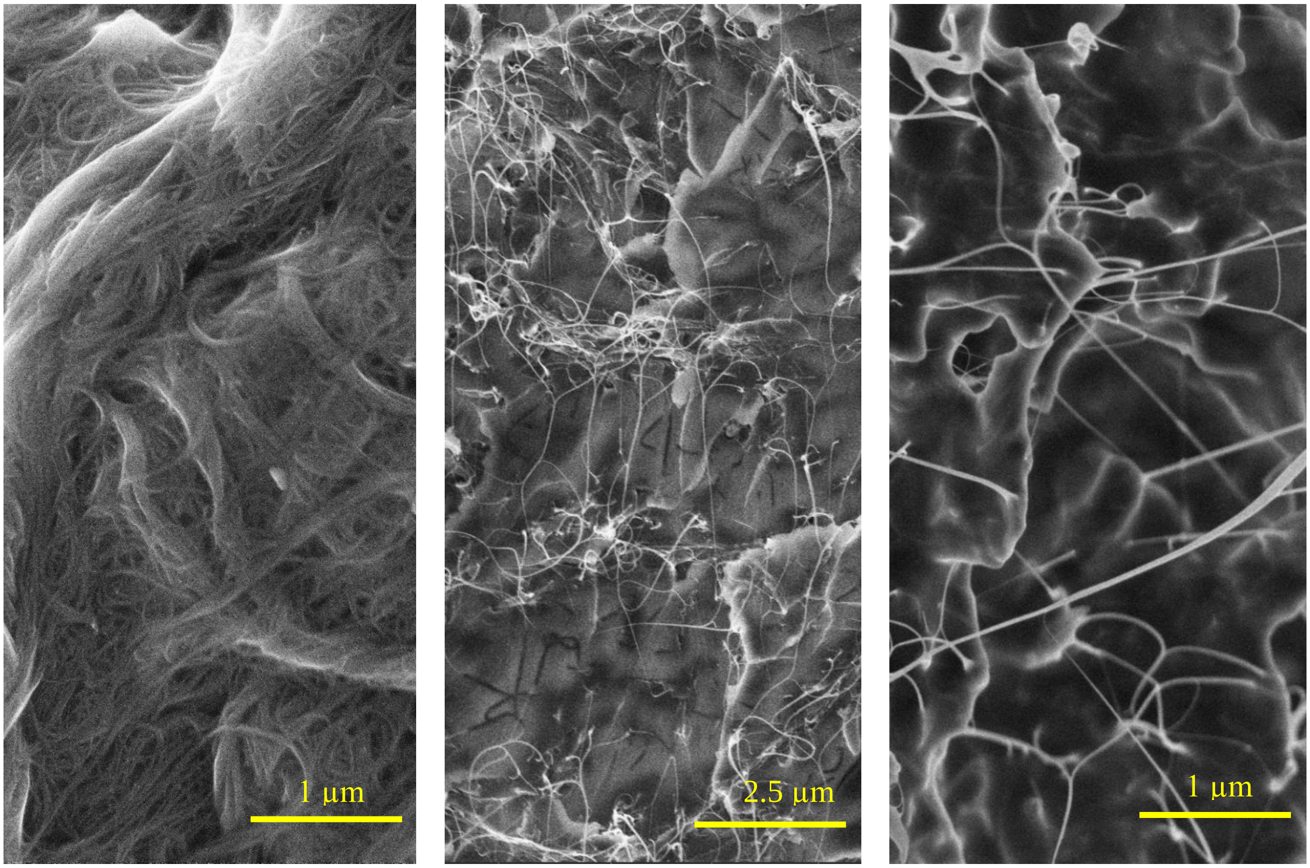

(a) (b) (c)

Figure 3.7. SEM images of (a) masterbatch, (b) LC interleave and (c) HC interleave showing the distribution of SWCNTs in the epoxy. LC interleave and HC interleave SEM scans were taken on the sample fractured in the DCB test.

Figure 3.7 shows the SEM images of the masterbatch and the fractured surface of LC interleaved, and HC interleaved laminates. SWCNTs were well dispersed in the epoxy with few bundles noted in the SEM scan of the masterbatch, as shown in Figure 3.7a. Scarcely a few straight and twisted types of bundles of SWCNTs were noted as the masterbatch is produced by three-roll milling, as detailed in Table 3.2. Similarly, an SEM scan of the fractured surface of LC and HC interleaved laminates shows the SWCNTs in the interleaves are well dispersed, exhibiting almost perfect dispersion and distribution as presented in Figure 3.7b-c. The straight and twisted bundles, as noted in masterbatch, were not observed in the interleaves however, an unusual agglomeration was noted at a few locations. Dispersion of SWCNTs in epoxy nanocomposite with the same masterbatch and similar mixing conditions was also studied and reported in [106].

3.4.2 Characterization of interleave

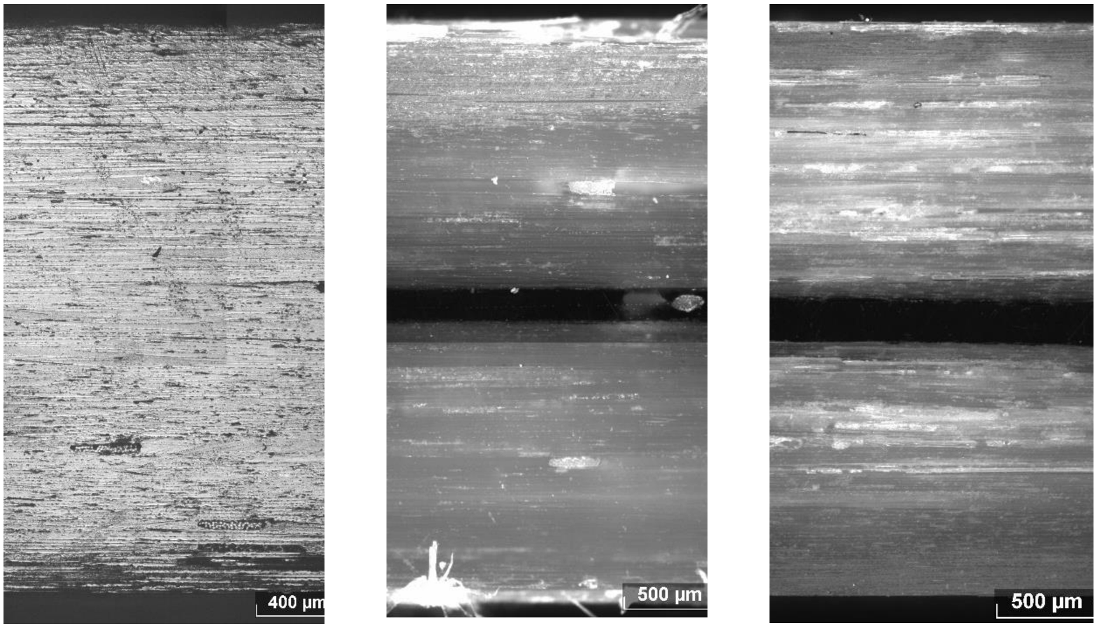

(a) (b) (c)

Figure 3.8. Optical microscopic image of (a) baseline (b) LC interleaved (c) HC interleaved laminates.

Figure 3.8 shows the optical microscopic image of baseline, LC interleaved, and HC interleaved laminates. Introduction of both types of interleaves changes the overall fiber volume fraction and thickness of laminates, as listed in Table 3.5.

The fiber volume fraction was estimated based on the areal density of fibers in the prepreg plies and the thickness of the laminate. The total thickness of the laminates increases by 14.2% and 4.7% for LC interleaved and HC interleaved laminates leading to a decrease in overall fiber volume fraction (method P, Table 3.5) by 7.4% in LC interleaved laminates and 2.7% in HC interleaved laminate, respectively. Similarly, the net fiber volume fraction, calculated after subtracting the thickness of interleave (method Q, Table 3.5) shows a reduction of 3.7% and increment of 2.3% for LC interleaved and HC interleaved laminates, respectively.

The thickness of interleaves is measured to be 200-250 µm. Such an interleave is too thick to be used in all the interlaminar positions of the laminate. It can be useful for counteracting the danger of Mode I fracture in specific dangerous positions, for example, in fork-like configuration, near noodle surfaces, or in a connection between a stiffener and a web.

A higher concentration of SWCNTs in HC interleaved laminate caused a higher entanglement of SWCNTs compared to the LC interleaved laminate, leading to a comparatively thicker interleave for HC interleaved laminate. A similar effect of thickening interleave with increasing concentration of SWCNTs in the interleave was also observed in [107].

Even after introducing a thicker interleave, the overall thickness of the HC interleaved laminate was lower than that of the LC interleaved laminate. It could be because some of the acetone did not evaporate completely and remained (even after a resting time of 3 hours), especially at the bottom of the interleave and possibly at some plies below it, which were in contact with the interleave during the resting time and could absorb acetone as well. We hypothesize that such excess acetone could reduce the viscosity of resin in the plies near the interleave, with the resin next being easier squeezed out at pressing, leading to a lower overall thickness of the HC interleaved laminate. Our hypothesis is supported by the fact that the lower part of the HC interleaved laminate (layers below the interleave which were in long contact with it) is thinner than the upper part of the HC laminate (layers that were placed on top of the stack just before putting the preform into the press), which can be easily observed from Figure 3.8c.

Table 3.5. Details of laminate thickness and fiber volume fraction.

Laminate		**Fiber volume fraction* [%]**		**Interleave thickness (t) [μm]**
Type	**Thickness* (T) [mm]**	**P**	**Q**	
Baseline	2.75 ± 0.093	59.6	59.6	-
LC interleaved	3.14 ± 0.122 (+ 14.2%)	52.2 (- 7.4%)	55.9 (- 3.7%)	206 ± 12.7
HC interleaved	2.88 ± 0.087 (+ 4.7%)	56.9 (- 2.7%)	61.9 (+ 2.3%)	231 ± 14.5

* '+' means increase and '-' means decrease in property. P and Q are two methods of fiber volume fraction estimation. P considers the overall laminate thickness with interleaf (T), whereas Q considers the laminate thickness (T_Q) obtained after subtracting the interleave thickness (t) as $T_Q = T - t$.

Continuing with this hypothesis for LC interleave, it could be possible that some of the interleave mixture moves to plies near the interleave, giving a high thickness value and low fiber volume fraction as noted in method Q of fiber volume fraction estimation in Table 3.5.

Addressing reasons behind changes in behavior, we observe, similar to other studies [107,108], that thickening of the interface zone in both LC and HC interleaved laminates was not the defining factor, rather the concentration of SWCNTs was. Weak SWCNTs bridging and weak fiber nesting in the LC interleaved laminate caused a detrimental effect relative to the strong fiber bridging in the baseline laminate. On the contrary, in the HC interleaved laminate, strong hierarchical SWCNTs bridging (more discussion on SWCNTs bridging in Section 3.4.6) allowed to obtain results better than the baseline.

3.4.3 Data reduction method

The DCB test results were processed following all three data reduction methods, as noted in the ASTM standard [102]. The obtained results, as plotted in Figure 3.9, show the comparison of the initiation fracture toughness and R-curve. The most conservative estimation of Mode I initiation fracture toughness was observed in the MBT method of data reduction, followed by the modified compliance calibration (MCC) and compliance calibration (CC) methods. This observation of the most conservative value of initiation fracture toughness is in agreement with the ASTM standard [102]. Even in the R-curve, the estimation of fracture toughness by the MBT and MCC is on the lower side when compared with the CC method, except towards the end of the test during which the CC method predicts the lowest fracture toughness.

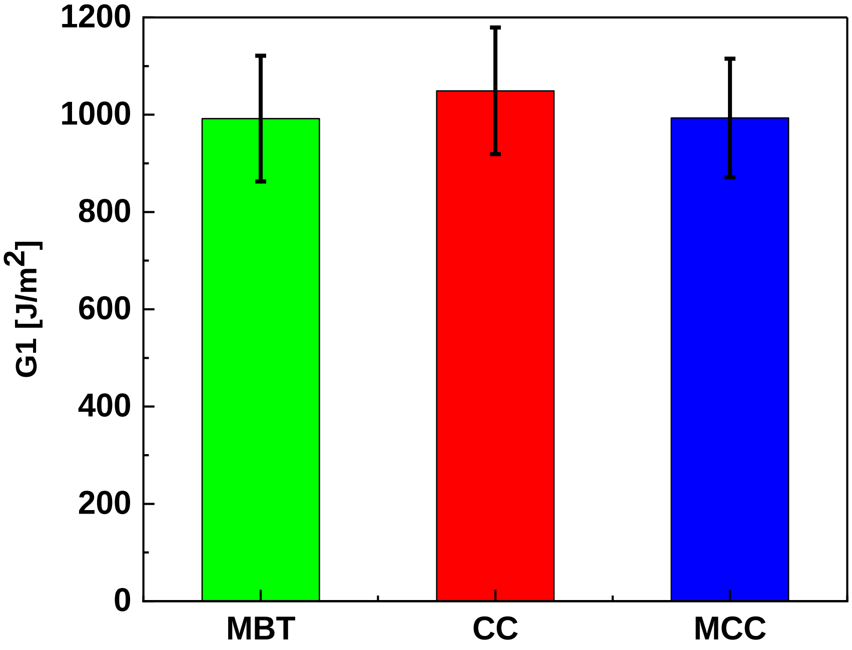

(a)

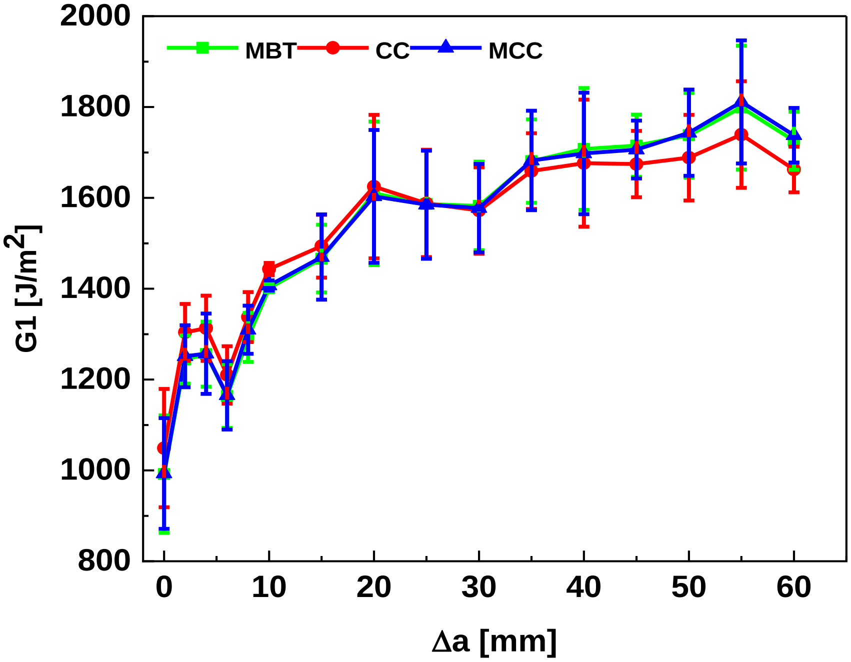

(b)

Figure 3.9. Comparison of (a) initiation fracture toughness and (b) R-curve for three different methods of data reduction of DCB test.

3.4.4 Mode I fracture toughness and R-curve

Mode I fracture toughness of the DCB specimens of baseline, LC interleaved, and HC interleaved laminates, calculated according to the MBT theory, are compared and plotted in Figure 3.10a. The initiation and propagation fracture toughness of the LC interleaved laminates decreased by ~80% relative to the baseline value, whereas an improvement of 27% and 0.5% is noted in the initiation and propagation fracture toughness of the HC interleaved laminates. The LC interleave in the laminate is richer in epoxy, rather than SWCNTs. Because of this, it shows a detrimental effect on the initiation and propagation fracture toughness of the laminate. On the contrary, the HC interleave in the laminate is rich in SWCNTs, giving them the possibility of introducing new toughening mechanisms in the laminates. The toughening mechanism will be discussed in Section 3.4.6.

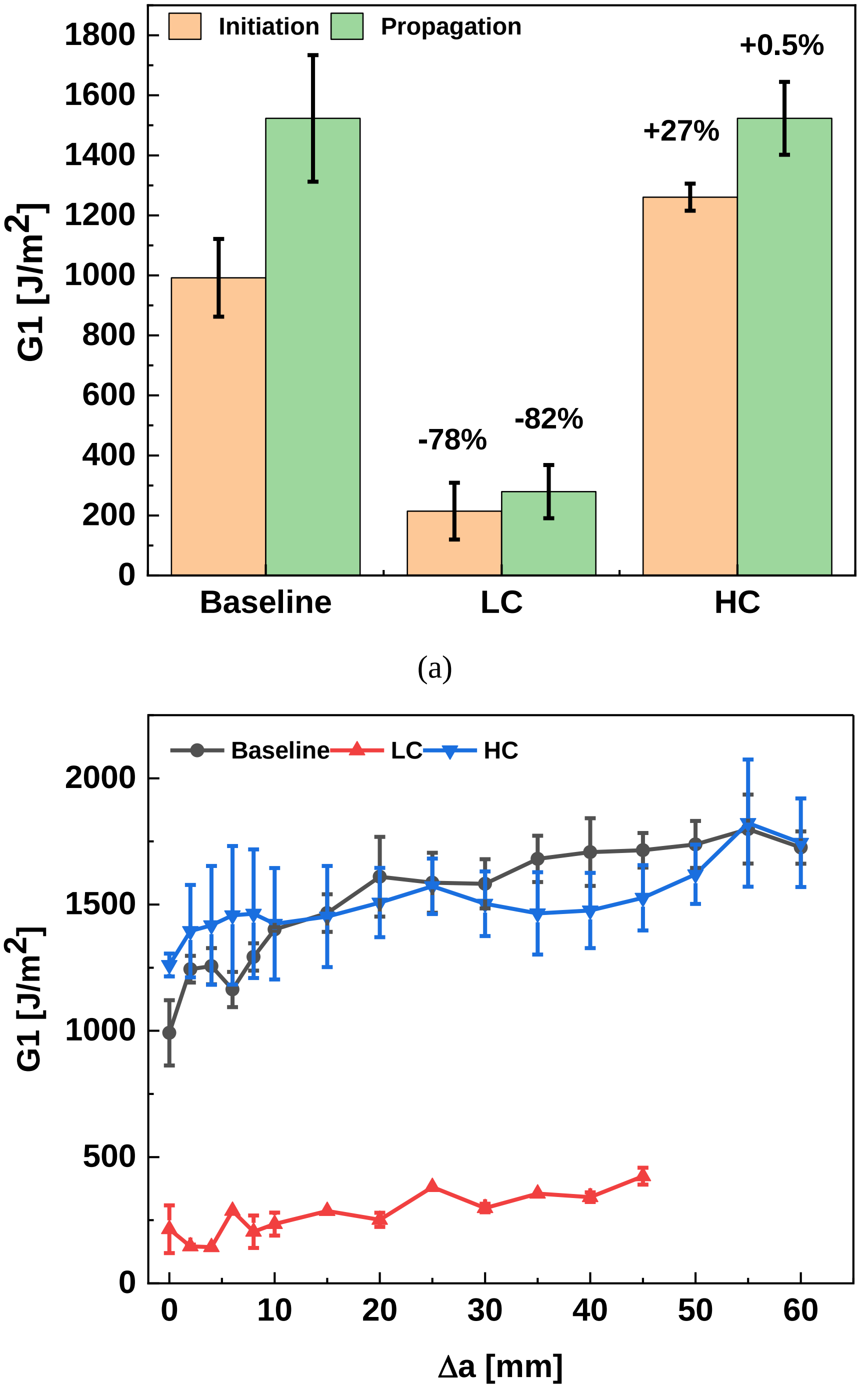

(a)

(b)

Figure 3.10. Comparison of (a) initiation, propagation fracture toughness, and (b) R-curve of the baseline LC interleaved and HC interleaved laminates.

Figure 3.10b shows the R-curve of the baseline, LC interleaved, and HC interleaved laminates. The LC interleaved laminate R-curve is very weak, whereas the R-curves of the baseline and HC interleaved laminates are strong and close to one another. It can be noted that the fracture toughness of the baseline laminate monotonically increases from the initiation point to the end of the test. The initiation fracture toughness of the HC interleaved laminates exceeds the value of the baseline laminates by 27%. It is followed by a slight decrease to the level and even below the baseline laminate, and the overall propagation fracture toughness does not change significantly but only by an increment of 0.5%. The R-curve of baseline and HC interleaved laminates show an increasing trend of Mode I fracture toughness with a change in crack length compared to the LC interleaved laminate, which shows a near-constant behavior. The effect of such a near-constant and increasing trend can be seen in the self-diagnostic ability described and discussed in detail in Section 3.4.5.

3.4.5 Self-diagnostic ability

The GFRP composite laminates are electrically insulative but the addition of thin layer interleaves in the interlaminar region transforms them into electrically conductive. The electrical conductivity of interleaves with SWCNTs concentration of as low as 0.6 wt% is in the range of 102-103 S/cm, changing to 100-101 S/cm for the 7.5 wt% interleaves [14,106]. The electrical conductivity is achieved by the percolating network of SWCNTs, which are highly sensitive to deformation, making the self-diagnostic ability of interleaves highly sensitive to even smaller deformations. It provides an opportunity for early damage detections at the phase of matrix cracking or delamination rather than the late phase of damage like fiber breakage.

Figure 3.11 shows the plot of force vs. displacement and change in resistance vs. displacement during the DCB test of interleaved laminates in comparison to the baseline laminates. There is a clear correlation between the applied force and the change in the resistance. There is no or slight change in resistance until the maximal load is reached. The point of maximum load indicates the crack initiation point. It is followed by the crack propagation phase during which a near-linear increase in resistance with the near-monotonically decreasing force for the HC interleaves. The reason is that the crack length of the HC interleaved samples increases steadily with time. In contrast, a pattern of stepwise jump is noted for the LC interleaved laminates during the crack propagation phase. Such stepwise jumps perfectly correlate with the drops in the force. After the crack initiation point, the force drops and starts to build up again until the crack propagates further, which results in successive force drops. The reason for such drops in the force is the near-constant dependence of the interlaminar fracture toughness, as noted in the R-curve (Figure 3.10b) of LC interleaved laminate. In Figure 3.11c, five force drops are noted before the completion of the test. Each force drop point is followed by a force build-up phase, which is a near-linear process with a decreasing slope from the first to the fifth build-up. Similarly, the peak force reached during the buildup also decreases with each drop and is always lower than the maximum force at the crack initiation point. Each force drop is clearly correlated to a resistance jump; after a jump, a change in resistance demonstrates attenuation due to mechanical relaxation. The described correlations between force and change in resistance can be used further for *in-situ* damage sensing and monitoring of composite laminates.

A similar pattern of step-wise jumps in the change in resistance with changing displacement, as observed in the LC interleaves in this research, was also noted in [42,44] for CNTs coated fibers. Similarly, a monotonic linear pattern of increase in the resistance with the change in displacement, as observed in this research for the HC interleaves, was also reported in [45] for polyethersulfone-carbon black film inserted in the interlaminar region.

Figure 3.12 shows the plot of the change in resistance with the change in the observed crack length for the LC and HC interleaved laminates. A linear fit to scatter data shows the linear dependence, as predicted by the theoretical model, as presented in Section 3.3.4. A similar linear fit to the plot of ΔR/R vs. Δa is also noted in [43,44,109].

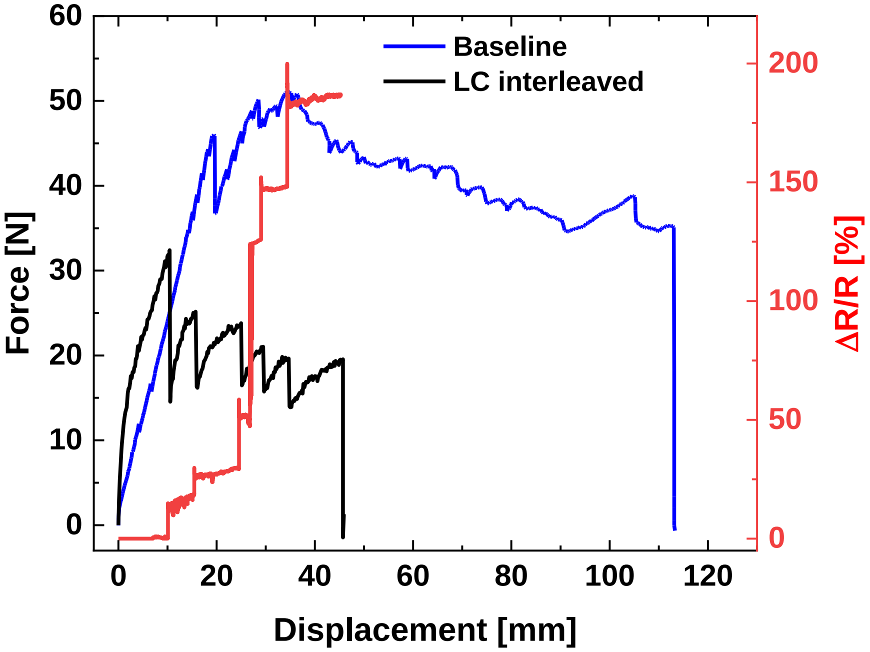

(a)

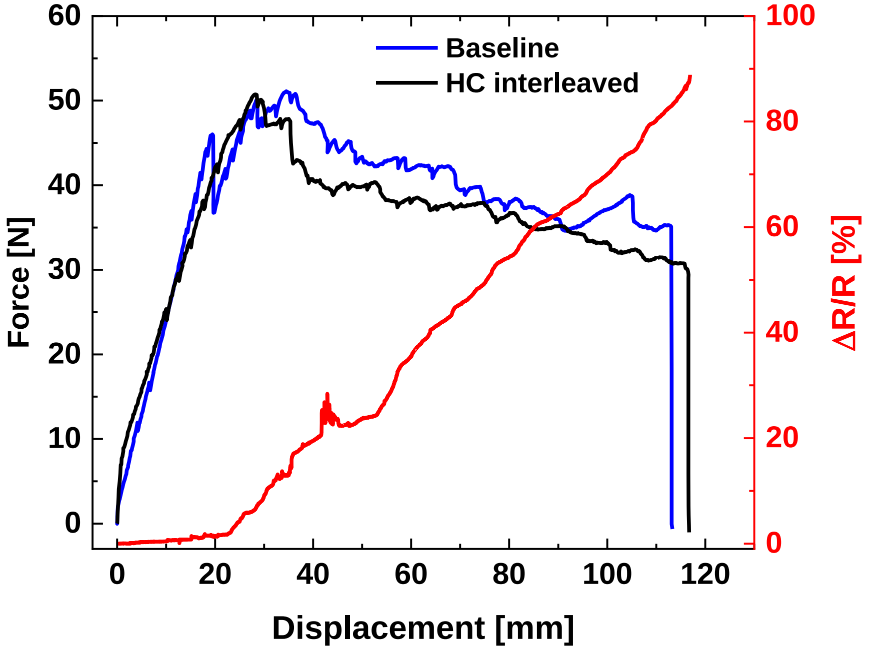

(b)

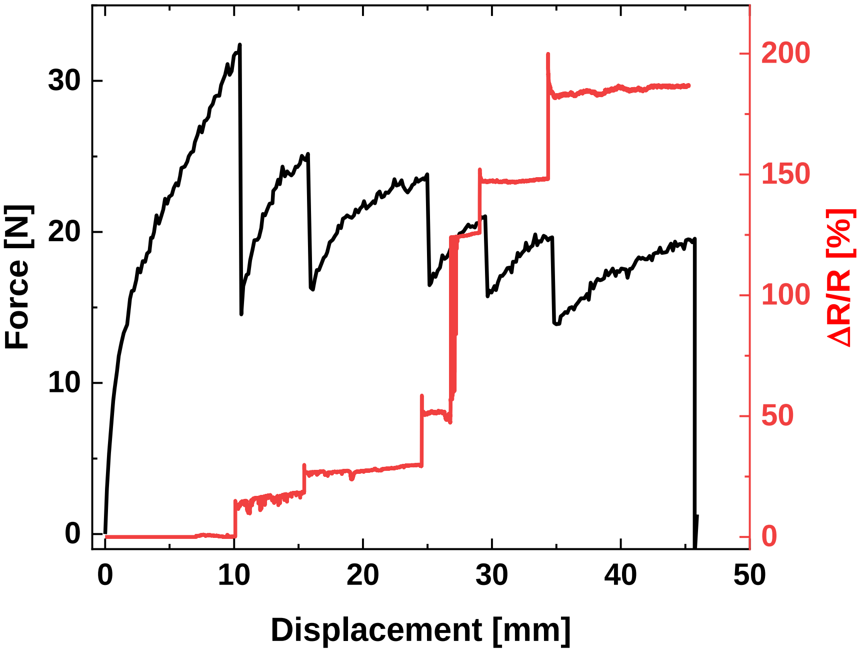

(c)

Figure 3.11. *In-situ* damage sensing and monitoring capability of (a) LC interleaved laminate and (b) HC interleaved laminate in comparison with the force-displacement of baseline laminate. (c) Magnified plot of LC interleaved laminate without baseline to show the stepwise drop in forces matches exactly with stepwise increase in resistance.

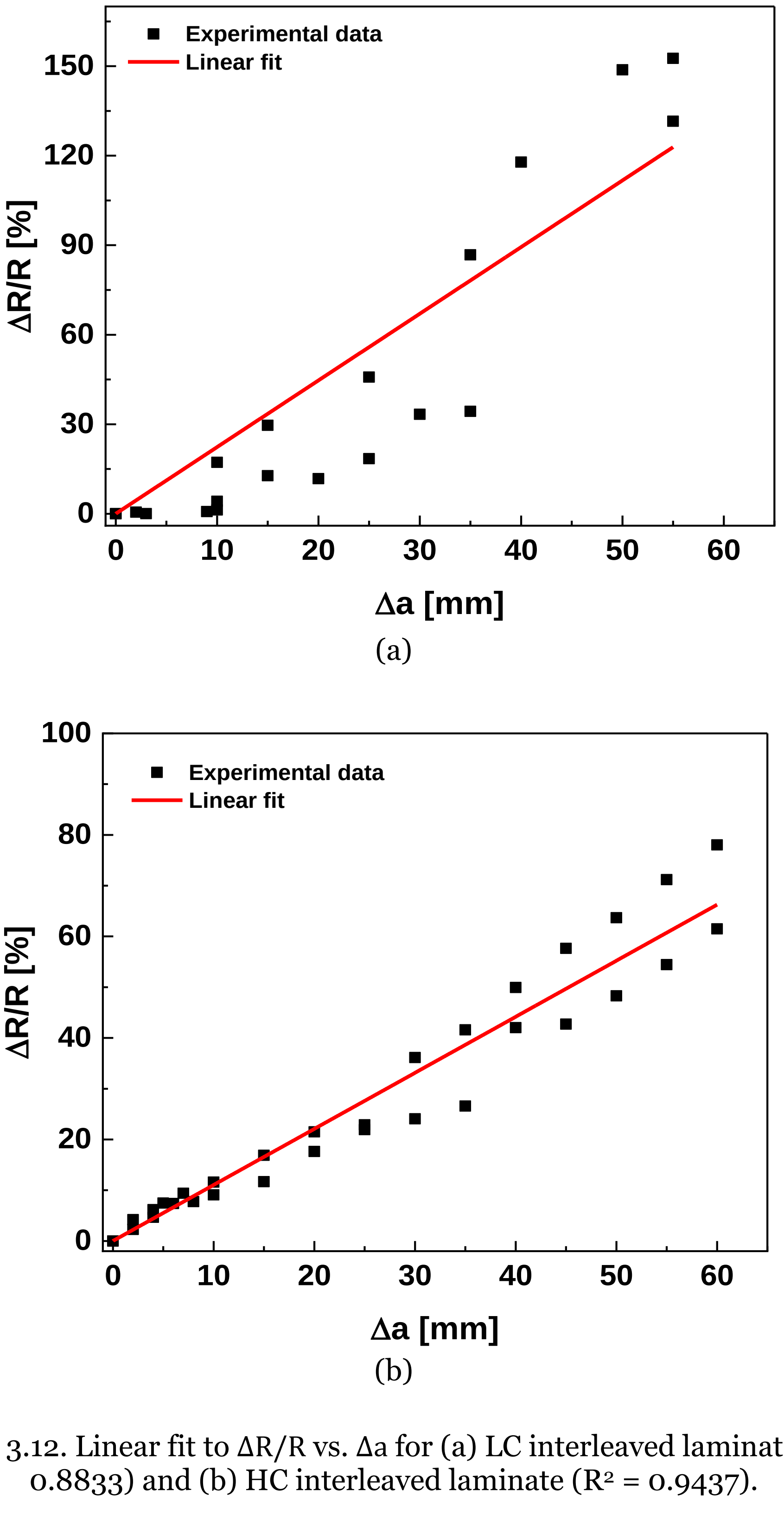

(a)

(b)

Figure 3.12. Linear fit to ΔR/R vs. Δa for (a) LC interleaved laminate (R^2 = 0.8833) and (b) HC interleaved laminate (R^2 = 0.9437).

3.4.6 Fractography

Fractured surfaces of the tested DCB specimens of the baseline, LC interleaved, and HC interleaved laminates were examined and presented in Figure 3.13, Figure 3.14, and Figure 3.15, respectively. Typical features of fiber bridging and fiber bundle crossing were noted in the baseline laminates, as shown in Figure 3.13. These are the toughening mechanisms in unidirectional fiber-reinforced composite laminate.

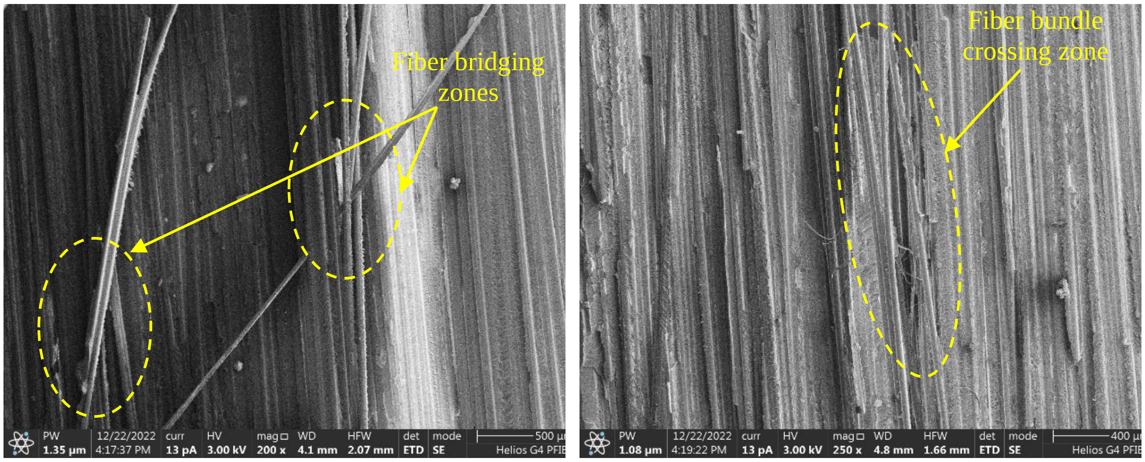

(a) (b)

Figure 3.13. Fractography of a baseline laminate.

The fractured surface of the LC interleaved laminates shows various other mechanisms at play. As the LC interleave was rich in epoxy (0.6 wt% SWCNTs only), the phenomenon of easier and earlier debonding of fibers from the interleave was noted. The riverbed-like pattern is formed in the debonded zones as shown in Figure 3.14c. At higher magnification of the corner of these riverbeds, as shown in Figure 3.14d, the interface of fibers and interleave illustrates the weaker debonding strength. Some amount of the SWCNTs were noted still covering the fibers, but these SWCNTs could not bridge the weak interaction zones. Another phenomenon of interleave tearing, as shown in Figure 3.14a, b, which is supposed to improve the fracture toughness is also noted but this effect is masked by the weak-debonding effect causing the fracture toughness of the LC interleaved laminates to be lower than that of the baseline laminates.

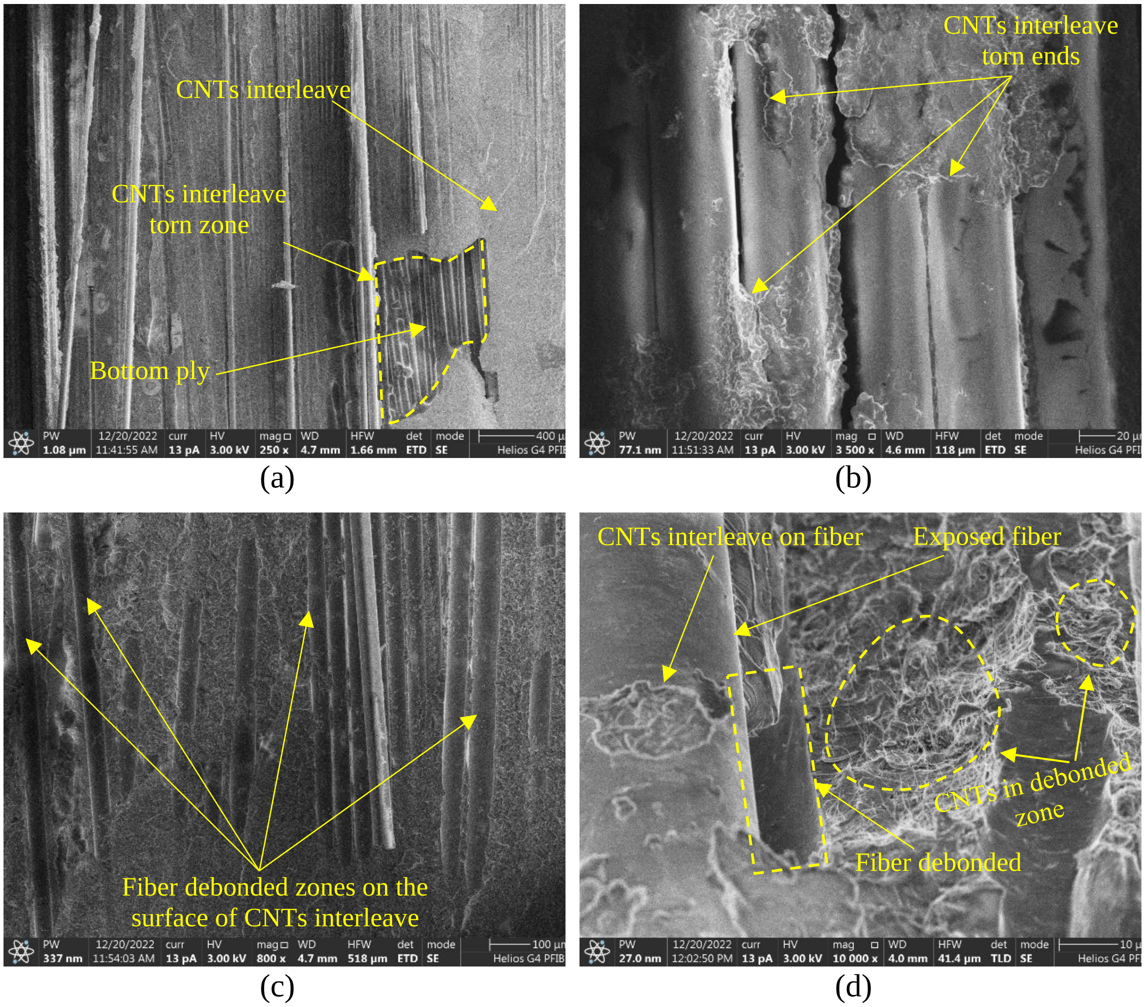

Figure 3.14. Fractography of an LC interleaved laminate. (a) - (d) fractography at micrometer level. SWCNTs in fuzzy form are visible in (d).

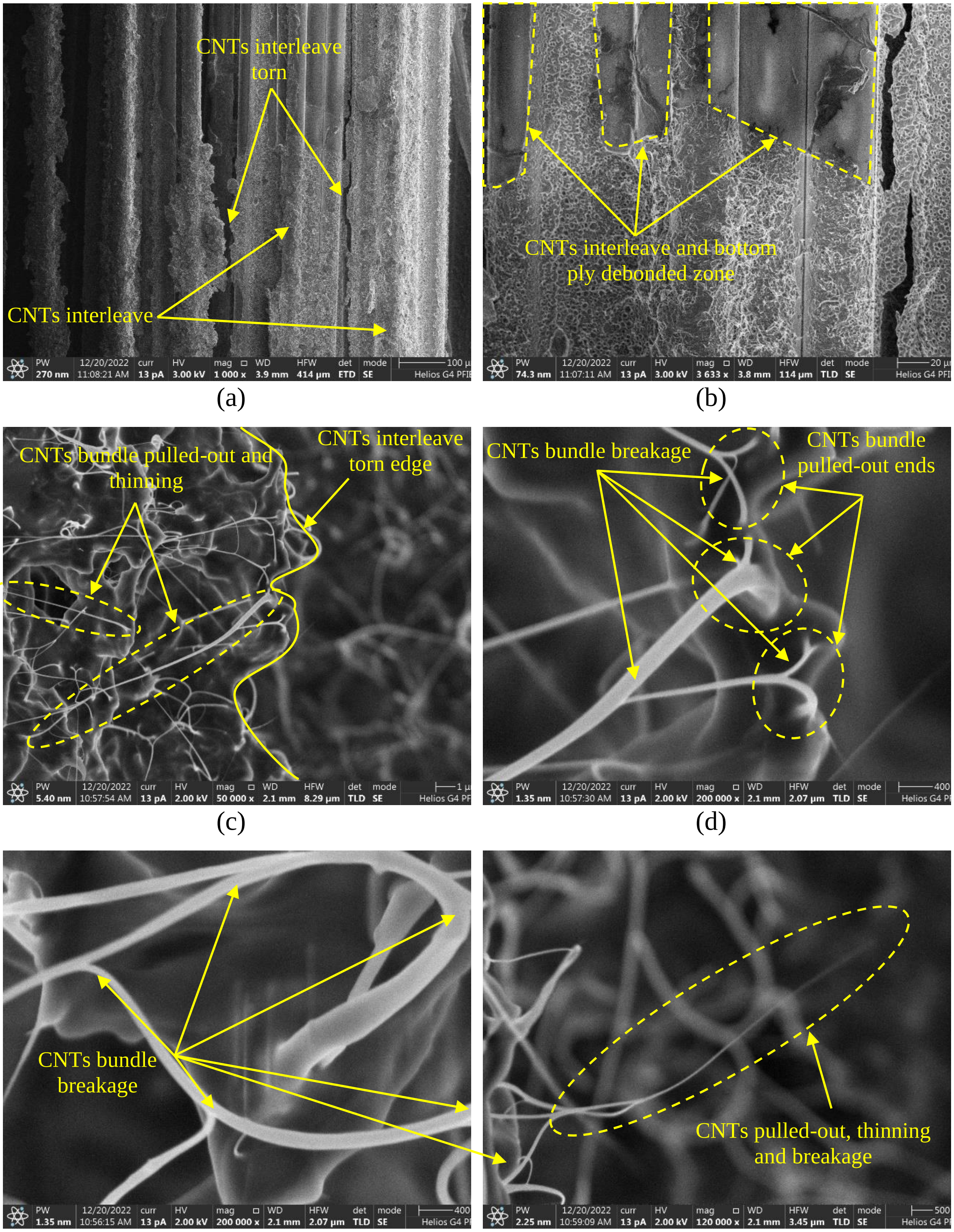

(a) (b)

(c) (d)

(e) (f)

Figure 3.15. Fractography of an HC interleaved laminate. (a) - (b) shows fractography at µm scale. (c) - (f) shows fractography at nm scale.

In the HC interleaved laminates, the tearing of interleaves, as shown in Figure 3.15a, is noted. It offers multiple sites where energy is consumed during the loading, leading to an increase in the Mode I fracture toughness. It is followed by the main toughening mechanism observed in the HC interleaved laminates, namely, SWCNTs and SWCNTs-bundles pulled-out of epoxy followed by SWCNTs bundle breakage, SWCNTs thinning, and breakage of SWCNTs. SWCNTs-bundle breakage also added SWCNTs nano bridging effect, where SWCNTs-bundle connects two parts as a bridge. All these toughening mechanisms consume energy during the test, resulting in improving the overall fracture toughness of the HC interleaved laminates. Several regions were noted with smaller missing chunks of the interleave, as shown in Figure 3.15b. It is because the interleave was torn from one half of the DCB sample and stuck to the other half of the DCB sample. It could be characterized as the 3D tearing effect. It would also consume a lot of fracture energy during the test, resulting in an overall improvement in the Mode I fracture toughness of the HC interleaved laminates.

We argue that the good performance of the HC interleaved laminates was because of the contribution of various SWCNT-related hierarchical toughening mechanisms at play. On the contrary, for the LC interleaved laminates, SWCNTs were not involved at most in toughening due to the premature failure of the fiber/interleave interface, as it is rich in epoxy. Thereby, interleaving destroyed the fiber-bridging effect by preventing nesting and simultaneously did not introduce new toughening mechanisms, leading to poor performance of the LC interleaved laminates.

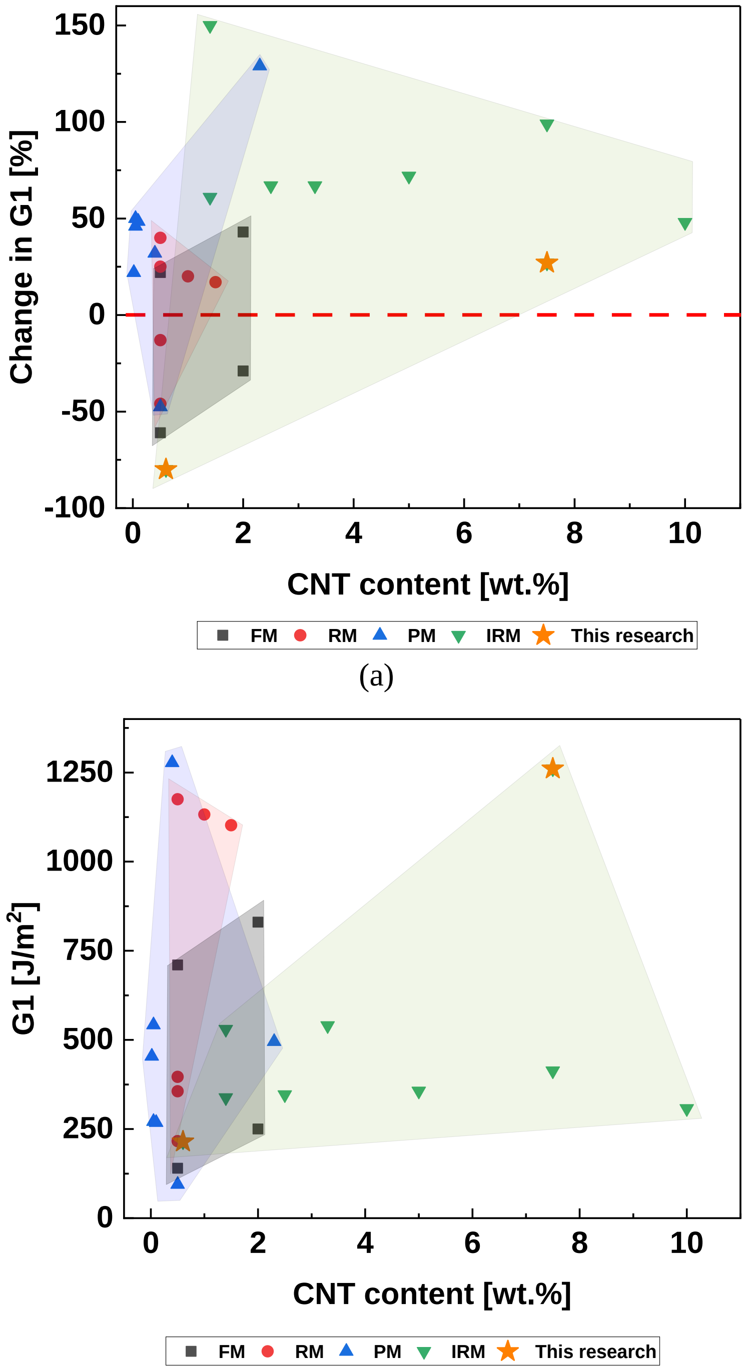

(a)

(b)

Figure 3.16. Effect of CNTs addition by various modification methods on Mode I fracture toughness (a) compared by improvement in G1 [%] and (b) compared by G1 [J/m^2]. The reference to the data points and acronyms can be found in Table 3.1.

3.5 Discussion

The factual data on Mode I fracture toughness and improvement over the baseline, as listed in Table 3.1, were plotted, as shown in Figure 3.16. The data points were joined to form a region of effect for each modification method, which includes fiber, resin, prepreg/fabric, and interlaminar region modification. On top of thus obtained plot, the fracture toughness results found in this research are also plotted for comparison. It is noted that the results obtained in this research are within the bounds created by the data points reported in the literature when compared in terms of percentage improvement over the baseline. In Figure 3.16a, it is worthy to note that all four methods of modification show a positive impact on Mode I fracture toughness along with some level of detrimental effects in some conditions. Similar patterns are also observed in this research, a detrimental effect for the LC interleave and an improving effect for the HC interleave. However, when compared in terms of the absolute value, the achieved Mode I fracture toughness lies at the upper limit of the range reported in the literature, as shown in Figure 3.16b.

3.6 Conclusion

Interlaminar region modification of composite laminate by nanoscale modification method of introducing industrially available SWCNTs masterbatch is demonstrated. Various problems like CNTs filtration, agglomeration of CNTs, and health concerns related to handling the CNTs powder do not appear in this method of introducing CNTs in the composite laminate. The SWCNTs masterbatch is available at an industrial scale so it can be recommended for large composite structures, hence providing the surety of scalability. This method of modification shows an improvement in Mode I fracture toughness by 27% for initiation, with the propagation fracture toughness unchanged, and provides a possibility of *in-situ* damage sensing and monitoring suitable for structural health monitoring applications. The toughening mechanisms causing such improvements are identified and discussed.

3.7 Publications

The results were published as a journal article in the Composite Science and Technology Journal as,

B. Mahato, S.V. Lomov, M. Jafarypouria, M. Owais, S.G. Abaimov, Hierarchical Toughening and Self-diagnostic Interleave for Composite Laminates Manufactured from Industrial Carbon Nanotube Masterbatch, Composite Science and Technology, 2023, doi.org/10.1016/j.compscitech.2023.110241.

The authors' contributions to this journal article are as follows: Conceptualization, B.M., S.V.L and S.G.A.; methodology, B.M., S.V.L and S.G.A.; software, B.M.; validation, B.M.; formal analysis, B.M., S.V.L and S.G.A.; investigation, B.M.; resources, B.M., S.V.L and S.G.A.; data curation, B.M.; writing–original draft preparation, B.M.; writing–review and editing, B.M., S.V.L, M.J, M.O. and S.G.A.; visualization, B.M.; supervision, S.G.A.; project administration, S.G.A.; funding acquisition, S.G.A.; corresponding author, B.M.

It was also presented as a poster during the IOCN 2023 conference as,

B. Mahato, S.V. Lomov, S.G. Abaimov, Toughening and Self-diagnostic Carbon Nanotubes Interleave Manufactured from Industrial Masterbatch, 4th International Online Conference on Nanomaterials (IOCN2023), Online, 2023.

The authors' contributions to this poster publication are as follows: Conceptualization, B.M., S.V.L and S.G.A.; methodology, B.M., S.V.L and S.G.A.; software, B.M.; validation, B.M.; formal analysis, B.M., S.V.L and S.G.A.; investigation, B.M.; resources, B.M., S.V.L and S.G.A.; data curation, B.M.; writing–original draft preparation, B.M.; writing–review and editing, B.M., S.V.L, and S.G.A.; design and visualization, B.M.; supervision, S.G.A.; project administration, S.G.A.; funding acquisition, S.G.A.; corresponding author, B.M.; presentation, B.M.

It was also presented as an oral presentation during the ICKEM 2023 conference as,

B. Mahato, S.V. Lomov, S.G. Abaimov, Multifunctional Interleave Manufactured from Industrial Carbon Nanotubes Masterbatch, 13th International Conference on Key Engineering Materials (ICKEM2023), Istanbul, Türkiye, 2023.

The authors' contributions to this oral presentation are as follows: Conceptualization, B.M., S.V.L and S.G.A.; methodology, B.M., S.V.L and S.G.A.; software, B.M.; validation, B.M.; formal analysis, B.M., S.V.L and S.G.A.; investigation, B.M.; resources, B.M., S.V.L and S.G.A.; data curation, B.M.; writing–original draft preparation, B.M.; writing–review and editing, B.M., S.V.L, and S.G.A.; design and visualization, B.M.; supervision, S.G.A.; project administration, S.G.A.; funding acquisition, S.G.A.; corresponding author, B.M.; presentation, B.M.

Chapter 4

Cure Monitoring

An alternative and promising technique to create a low-cost, efficient, easy-to-operate, and interpret nanocomposite sensor system for monitoring the degree of cure of thermoset matrices is presented. The nanocomposite is produced by introducing carbon-based nanoparticles, specifically SWCNTs, into epoxy precursors and matrices. The addition of these particles to an epoxy matrix allows the matrix to become electrically conductive [14]. The electric conductivity on the nano-modified matrix may depend on the matrix state, for example, change with thermal aging [110], and is affected by matrix curing [48]. Thus, the electrical conductivity of the material can be used to ascertain the degree of curing without the use of external testing techniques leading to quality control, *in-situ* tuning of the manufacturing process to optimal temperature regime, and reduction in production time and cost. At the same time, the addition of carbon nanotubes at reasonable weight fractions to epoxy matrices has been shown to improve the mechanical properties [111,112]. Thus, the proposed method not only allows epoxy properties to be monitored during manufacturing and curing but also allows the resulting epoxy to be multifunctional, which offers more value for the same input, as discussed in Chapter 1.

For composite manufacturing industries, such a material and monitoring method can lead to important economic advantages, cutting down on monitoring and quality assurance overheads, reducing part rejections, and producing new, multifunctional composites [113]. Furthermore, the design of heating cycles for in- and out-of-autoclave processes and active feedback loops during processing will streamline current production methods, further reducing the cost of production. It will improve and advance the quality control and productivity of composite manufacturing.

4.1 Materials

The SWCNTs were purchased from OCSiAl - Tuball™ matrix 301. The details of the masterbatch are listed in Table 3.2. The SWCNTs masterbatch was diluted by the DGEBA-based epoxy (EPOLAM 2031) taken as the base thermoset material. It was chosen for dilution because of its low viscosity and its compatibility with the SWCNTs masterbatch polymer. No additional solvents or dispersants were added during mixing. EPOLAM 2031 and Tuball™ matrix 301 were used as received.

4.2 Methodology

4.2.1 Sample production

Table 4.1. Steps for production of nanocomposites.

Materials	**Step 1**		**Step 2**	
Epoxy + Masterbatch	Low RPM Heating (40°C) 20 min	15 min of vacuum degassing	High RPM Heating (40°C) 60 min	15 min of vacuum degassing
	Step 3			
Epoxy + Masterbatch + Hardener	High RPM No heating 20 min.		15 min of vacuum degassing	

Nanocomposite was produced by shear mixing SWCNTs masterbatch with epoxy to obtain 0.6 wt% at a temperature of 40°C and relative humidity of 30%.

The mixing was performed by ECROSTM overhead stirrer PE-8300. Three different stirring settings were used with varying speeds and duration, as presented in Table 4.1. Step 1 and Step 2 were used to mix masterbatch with epoxy, whereas Step 3 was used to mix the obtained mixture with hardener. Each of the steps was followed by 15 minutes of vacuum degassing at a low pressure of 0.1 mbar. After Step 3, the nanocomposite was ready for molding and was transferred into a silicone mold with copper contacts on the two opposite faces of the mold. The size of the gap where the nanocomposite is transferred in the mold is 25×25×25 mm. The copper wire insulated with heat resistance polymer (Melting temperature: 300°C) was soldered to the copper contact on one end and to the 2-point electrical resistance measurement unit on another end, as shown in the schematic diagram in Figure 4.1a.

4.2.2 Pre-cure and cure Cycle

The setup was left to pre-cure for 2 hours at room temperature of 25°C and relative humidity of 30%. Later, it was transferred into an electrical heating oven BINDERTM BD (E2) for curing at a temperature of 130°C for 3 hours. The heating ramp of 5°C/min was used. The plot of temperature-time variation during the pre-cure and cure cycle can be seen in Figure 4.5.

4.2.3 Electrical resistivity measurement and mechanism

The direct current (DC) 2-point electrical resistance was measured and recorded for all the samples during the pre-cure and cure cycle using the Tektronix™ Keithley DMM 6500–TSCAN-2001 multichannel digital multimeter, as shown in Figure 4.1a. The resistance of the connection wire and contact point was measured separately by a 4-point probe and subtracted from the base reading for all the samples. The electrical resistivity (ρ) was calculated using Equation (4.1) where R is the corrected 2-point electrical resistance, A is the cross-sectional area of the sample, and L is the distance between the measuring probes of 2-point measurement. The temperature inside the oven air was measured by a K-type thermocouple and simultaneously recorded by a Keithley DMM 6500 unit. Other details of electrical resistivity and temperature measurement can be found in Ref. [106]. The electrical resistance and temperature variation measured during the pre-cure and cure cycles are discussed in Section 4.3.2.

$$\rho = \frac{\mathrm{R\,A}}{\mathrm{L}} = \frac{\mathrm{R\,L}^2}{\mathrm{L}} = \mathrm{R.L} \tag{4.1}$$

$$\mathrm{R} = \mathrm{R}_{\mathrm{SWCNTs}} + \mathrm{R}_{\mathrm{tunneling}} \tag{4.2}$$

$$\mathrm{R}_{\mathrm{tunneling}} = \mathrm{f}(\delta) \tag{4.3}$$

$$\delta_{\mathrm{I}} < \delta_{\mathrm{II}} < \delta_{\mathrm{III}} \tag{4.4}$$

$$\delta_{\mathrm{III}} > \delta_{\mathrm{IV}} > \delta_{\mathrm{V}} \tag{4.5}$$

$$\rho_{\mathrm{I}} < \rho_{\mathrm{II}} < \rho_{\mathrm{III}} \tag{4.6}$$

$$\rho_{\mathrm{III}} > \rho_{\mathrm{IV}} > \rho_{\mathrm{V}} \tag{4.7}$$

Epoxy is an electrically insulative polymer that can be converted into electrically conductive by mixing SWCNTs. The electrical resistivity of such a nanocomposite depends on the concentration of filler. The new functionality of conductivity is added to the epoxy because of the percolation network built by the SWCNTs, as shown in the schematic diagram in Figure 4.1b. The electrical resistance of the nanocomposite, in this case, depends on the sum of intrinsic resistance offered by each SWCNTs ($\mathrm{R}_{\mathrm{SWCNTs}}$) and the tunneling resistance of CNT-CNT contact ($\mathrm{R}_{\mathrm{tunneling}}$) in the percolating network, as noted in Equation (4.2). In Figure 4.2a, the schematic diagram of three types of CNT-CNT contact (A, B, and C) present in the percolating network formed in the nanocomposite is shown. The conduction of electrons happens by a phenomenon known as quantum tunneling at those contacts. The tunneling resistance depends on the tunneling distance (δ) between two CNTs [114] at the contact, as noted in Equation (4.3).

The tunneling distance changes during the process of pre-cure and cure of nanocomposite, as shown in Figure 4.2b. Type A is an end-to-end CNT contact, Type B curved surface-to-curved surface contact, and Type C is an end-to-curved surface contact. Phase I-V consists of five different phases during the curing process, as detailed in Section 4.4. The effect of such changing tunneling distance on the overall electrical resistivity of the nanocomposite, as given by Equation (4.4) – Equation (4.7), is discussed in Section 4.4.

4.2.4 Microstructural analysis

Microstructural analysis was conducted on the Thermo Scientific™ Helios G4 PFIB SEM to check and verify the dispersion of SWCNTs masterbatch in the epoxy. Analysis was performed on the fractured surface of the electrical conductivity sample. No additional treatment was applied to the fractured surface. The results are presented in Section 4.3.1.

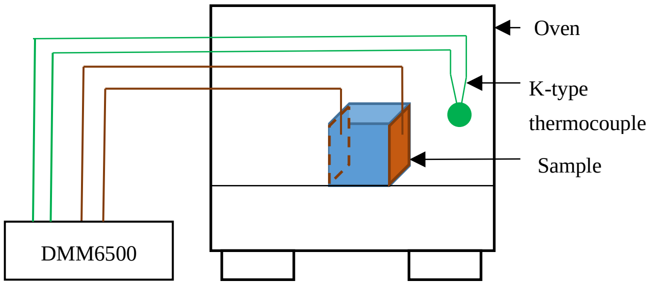

(a)

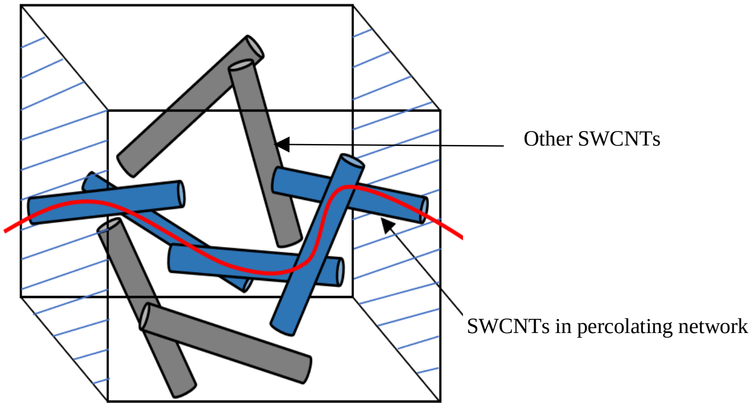

(b)

Figure 4.1. Schematic diagram showing (a) DC 2-point electrical resistance and temperature measurement and (b) simplistic view of SWCNTs percolating network needed for electrical conductivity.

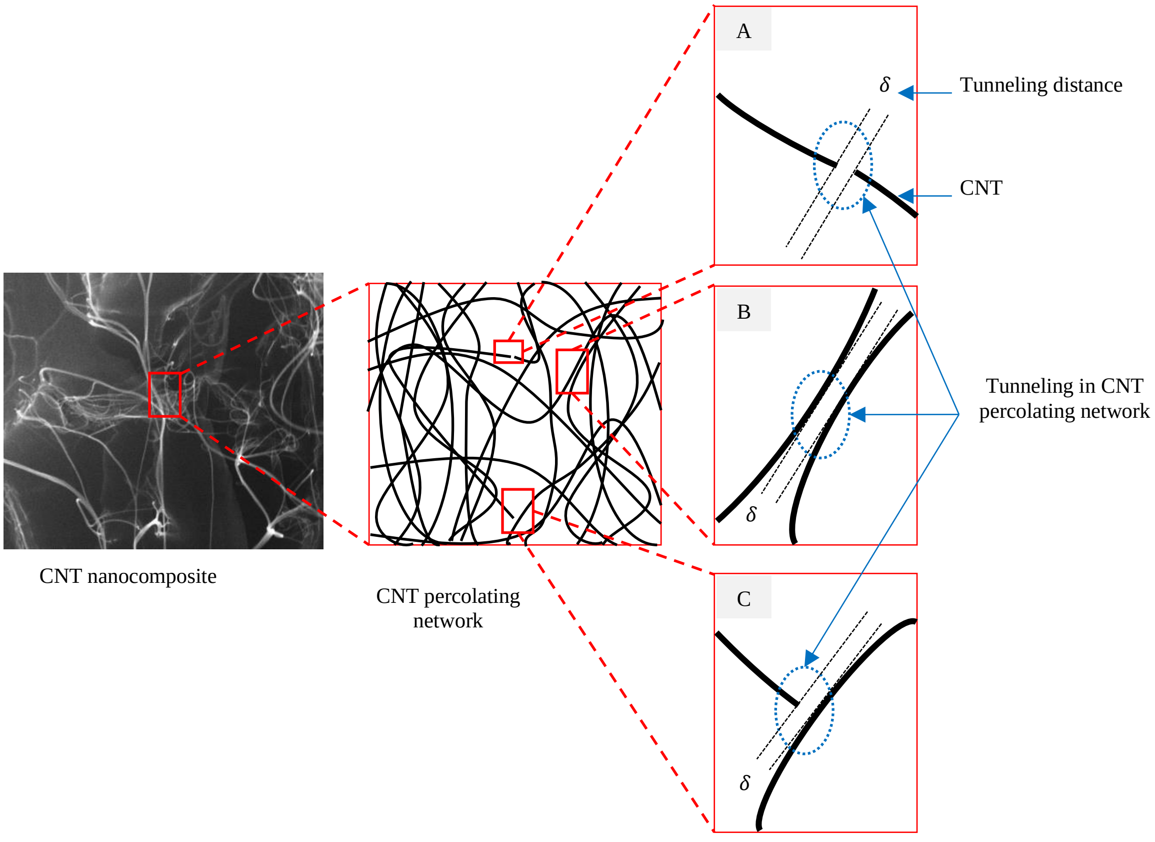

(a)

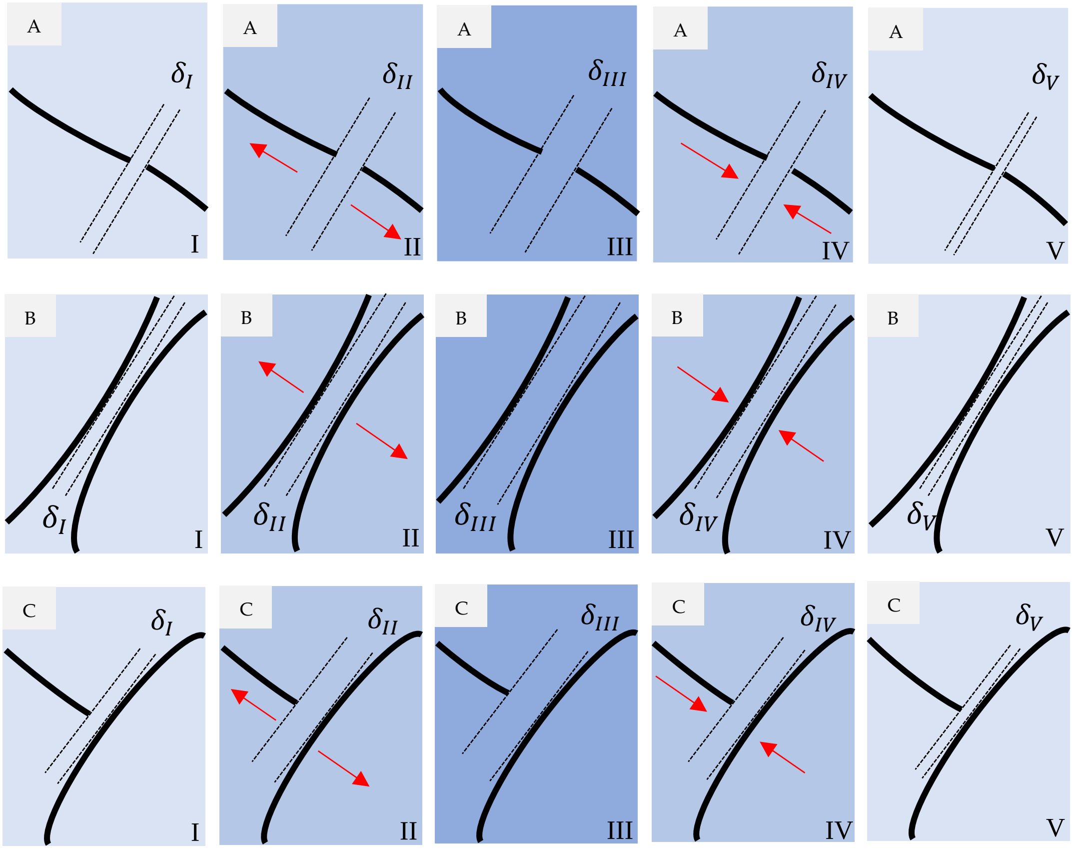

(b)

Figure 4.2. Schematic diagram showing (a) three types of CNT-CNT contact for tunneling conduction of electron in nanocomposite, and (b) variation in tunneling distance during curing of nanocomposite.

4.2.5 Degree of cure measurement

The degree of cure was evaluated using Shimadzu™ DSC-60 (TA instruments) DSC of the cured and uncured epoxy. To calculate the degree of cure over the pre-cure and curing cycle, two DSC scanning cycles were run. In the first DSC scanning cycle, the uncured epoxy was subjected to the same temperature-time cycle as the nanocomposite sample to measure the total heat flux to full curing. It included a pre-cure cycle of 2 hours followed by a heating ramp of

5°C/min reaching the maximum temperature of 130°C followed by an isothermal cycle of 130°C for a total duration of 3 hours. In the second DSC scanning cycle, the cured neat epoxy and nanocomposite samples were considered for dynamic DSC scanning from 30°C to 300°C at a heating ramp of 10°C/min. The degree of cure growth with time, as presented in Section 4.3.3, was calculated using Equation (4.8) where DoC ($\alpha(t)$) is the degree of cure, $H_{iso.}$ is the heat of reaction measured during isothermal DSC scanning, H_{total} is the total heat of reaction considering the $H_{iso.}$ as well as the residual heat measured in the dynamic DSC scanning and t is time. The details of data processing are presented in Appendix A.

$$\mathrm{DoC}\ [\alpha\ (t)] = \frac{H_{iso.}(t)}{H_{total}} \tag{4.8}$$

4.3 Results

4.3.1 Microstructural analysis

Figure 4.3 shows the SEM images of the SWCNTs masterbatch and the fractured surface of the nanocomposite. The bundles of SWCNTs in masterbatch were well dispersed, demonstrating near-perfect distribution and dispersion in the base epoxy with few exceptional agglomerations and bundling present. The mixing can be considered isotropic and homogeneous as the masterbatch used here is produced by three-roll milling, which makes it easier to attain the homogeneous state of mixing [115].

The electrical resistivity of the nanocomposite measured at the end of the cure cycle, as shown in Figure 4.4, matches exactly with the reported electrical resistivity values in Ref. [14]. This further proves the mixing of SWCNTs masterbatch in epoxy was consistent and homogeneous.

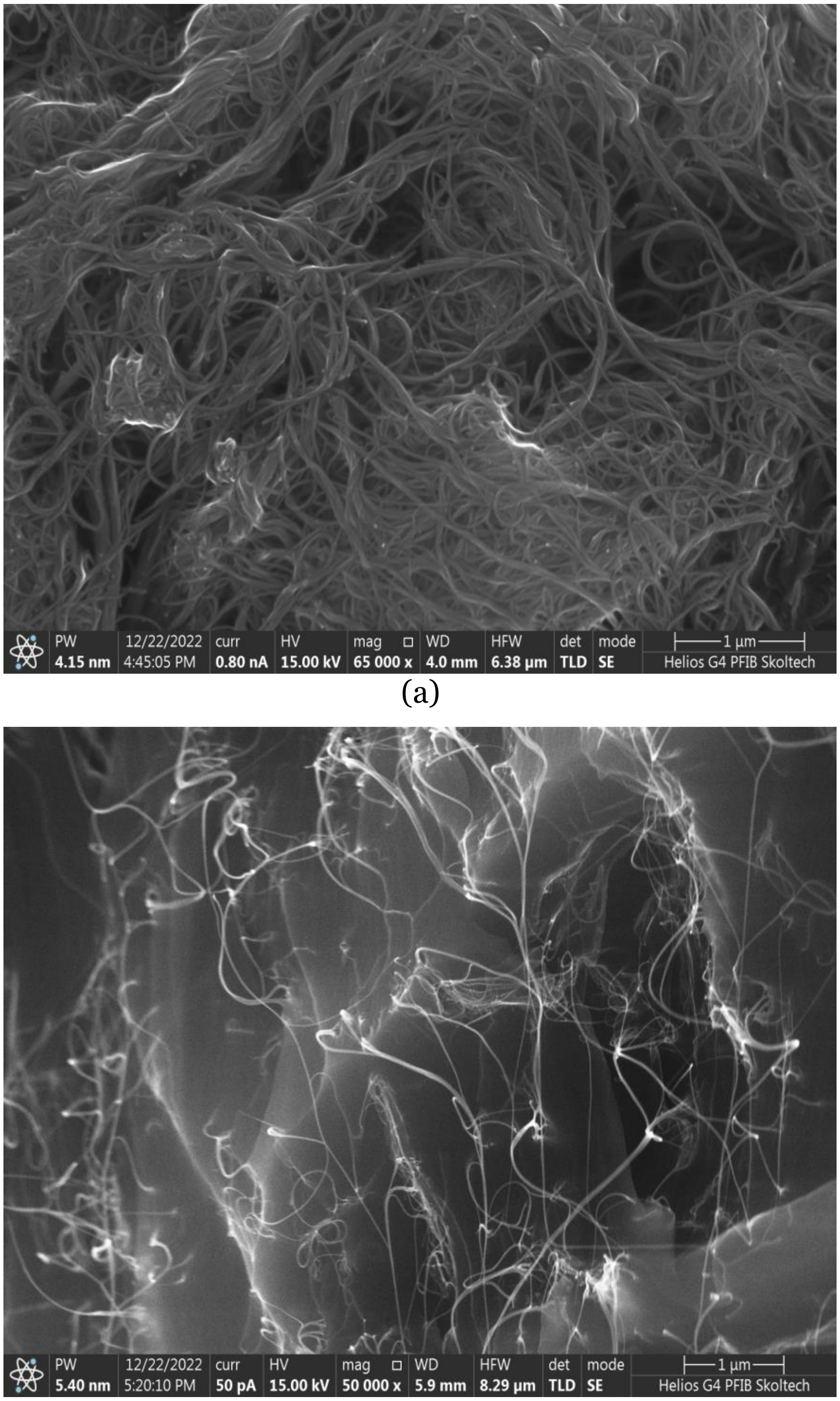

(a)

(b)

Figure 4.3. SEM image of (a) SWCNTs masterbatch and (b) epoxy nanocomposite with 0.6 wt% SWCNTs.

4.3.2 Electrical resistivity

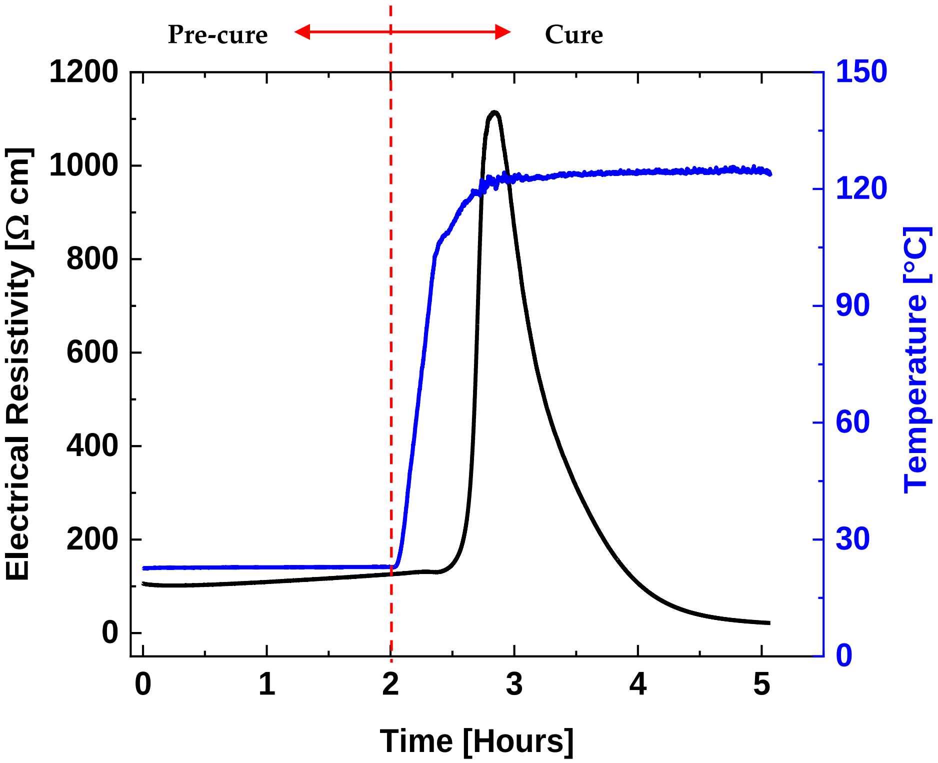

Figure 4.4. Variation of electrical resistivity and temperature during pre-cure and cure stage.

Figure 4.4 shows the change in the electrical resistivity and temperature of the nanocomposite during its pre-cure and cure stages. The pre-cure was performed at room temperature of 25-27°C for 2 hours and the cure was performed at the maximum temperature of 130°C with a heating ramp of 5°C/min for 3 hours followed by natural unaided cooling in the oven as shown in Figure 4.4. It was observed that the electrical resistivity of the nanocomposite increases slightly during the pre-cure stage, which further increases monotonically with increasing temperature up to a maximal value. During the isothermal phase, the electrical resistivity decreases monotonically and reaches a steady-state value. Further details on the reason for above noted behavior of electrical resistivity during pre-cure and cure are present in Section 4.4.

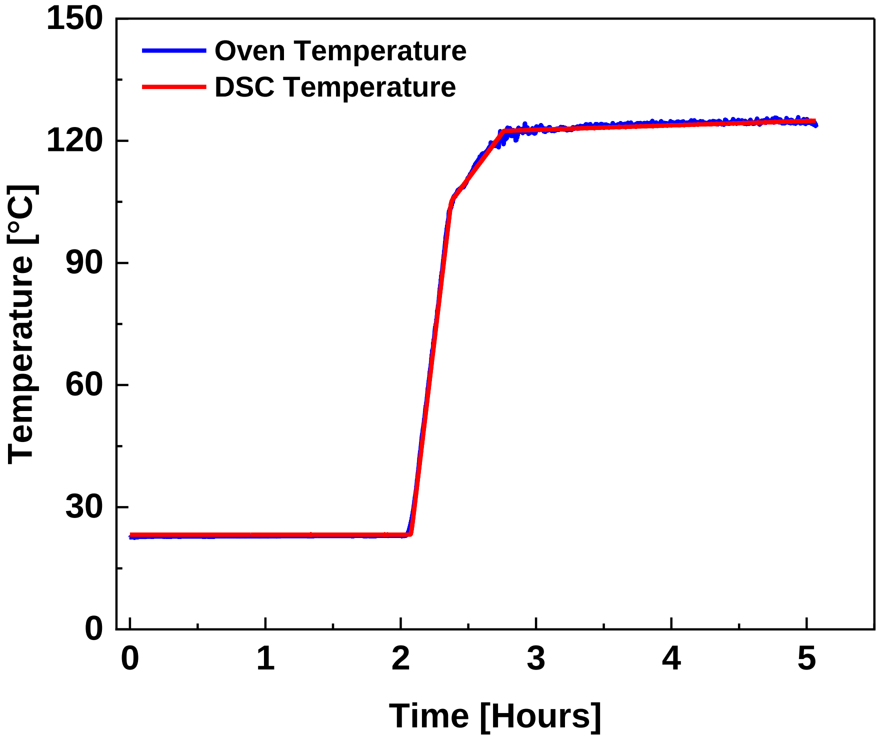

Figure 4.5. Linear fit to oven temperature to be used in DSC test.

During room temperature pre-cure of the nanocomposite, the polymeric cross-linking heat is released by epoxy, which increases the temperature slightly. This slight increase in temperature is responsible for a slight increase in the electrical resistivity, as noted in the pre-cure phase of Figure 4.4. It is clear from this explanation that the measurement of the temperature is very crucial. Hence, the temperature was measured inside the oven where curing was taking place, as presented in the schematic diagram in Figure 4.1a. Instead of set temperature at the oven controller, the temperature inside the oven was considered as shown in Figure 4.4 (right vertical axis). A piecewise-linear fit to this temperature was obtained as shown in Figure 4.5, for further processing and calculation of the degree of cure in DSC.

4.3.3 Degree of cure

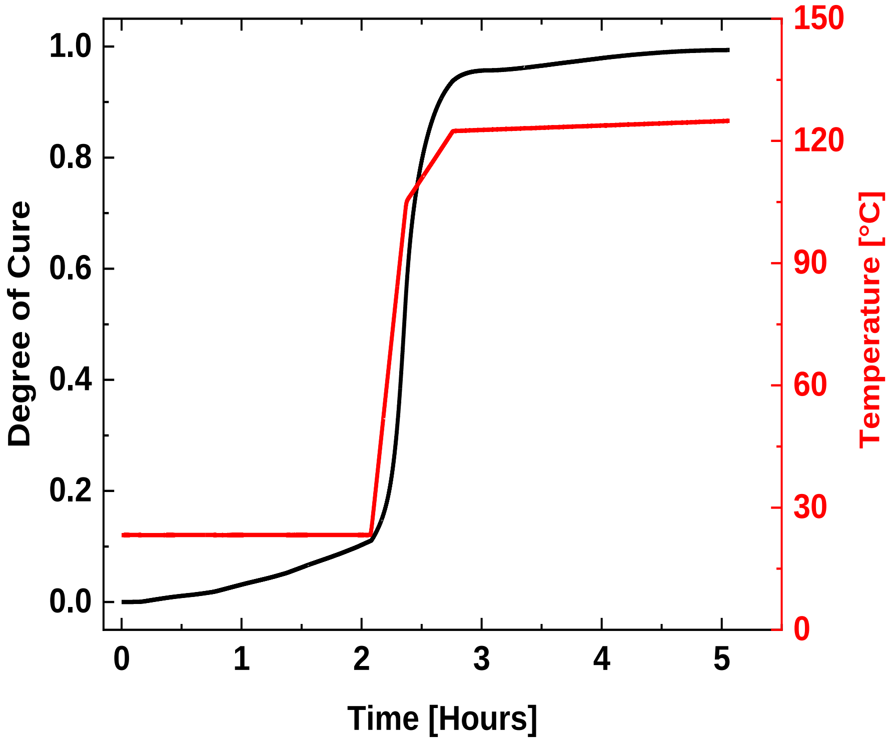

Figure 4.6. Growth of degree of cure with time measured by DSC.

The degree of cure of thermoset polymer indicates how well the polymer is cured and the highest possible degree of cure of 95-99% is desired for structural and functional applications of thermosets. The degree of cure of the nanocomposite was measured in two steps. First, the isothermal heat was measured for the uncured epoxy, followed by the residual heat in the cured sample. The temperature-time data obtained from linear fit, as shown in Figure 4.5, were used as input for the DSC dynamic run. It measures the dynamic change in the DSC heat used to calculate the growth of the degree of cure with change in time using Equation (4.2) and as plotted in Figure 4.6.

It shows the nanocomposite was cured ~10% during the first two hours of pre-cure and the rest of the curing occurred during the curing stage when elevated temperature was used. A monotonic increase in the degree of cure is noted during the heat ramp reaching close to ~95% and increases further linearly during the temperature isothermal phase. The inclusion and mixing of low concentrations of one-dimensional fillers like SWCNTs in the thermoset resin does not affect the curing kinetics behavior with respect to the neat epoxy [116].

4.3.4 Electrical resistivity vs. degree of cure

The variation of electrical resistivity with time, as shown in Figure 4.4, and the variation of degree of cure with time, as shown in Figure 4.6, are mapped onto one another to remove the time variable. Thus obtained was the variation in electrical resistivity with the degree of cure, as presented in Figure 4.7. It shows a surge in the electrical resistivity of the nanocomposite when a degree of cure of higher than ~90% is reached. It is followed by a decrease in the electrical conductivity monotonically again to reach its minimal value.

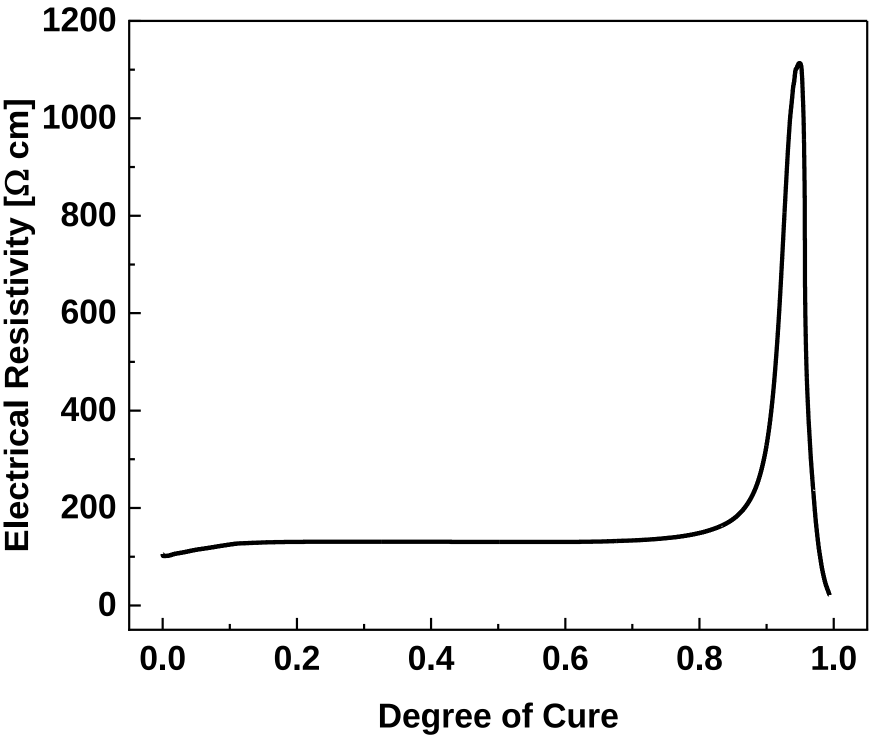

Figure 4.7. Electrical resistivity plotted against degree of cure.

4.4 Discussion

During the curing of the nanocomposite, the temperature rises because of which the viscosity of the epoxy in the nanocomposite which is not yet fully cured decreases. Such a decrease in the viscosity of the epoxy initiates the epoxy to flow and infiltrates the CNTs network further due to vacuum and capillary pressure (applicable profoundly to Type B contact over Type A or Type C contact, as shown in Figure 4.2).

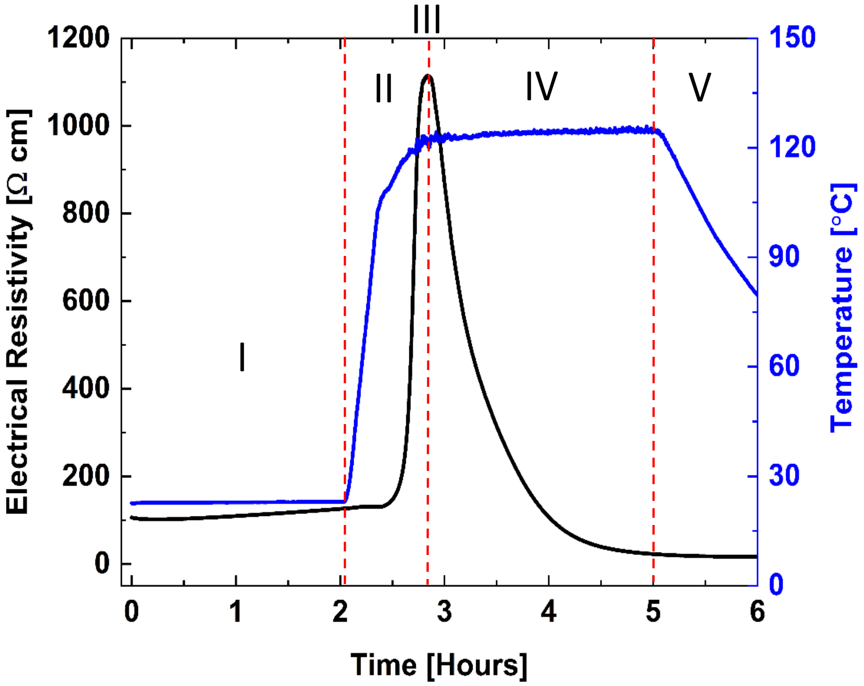

Figure 4.8. Electrical resistivity changes during pre-cure and cure. Phase I, II, III, IV, and V in the plot denote different phases of curing in view of varying tunneling distances, as shown in Figure 4.2.

Polymer molecules infiltrating CNT junctions change tunneling barriers to higher values as well as pushing CNTs apart. Due to the general temperature rise, thermal expansion also increases inter-CNT distances. This causes an overall increase in the resistance of the CNTs network as the conductivity at the CNT-CNT junction happens by the quantum tunneling effect (phase II in Figure 4.2). Upon reaching the maximum resistivity, the flow and infiltration of epoxy in the CNTs network stop (phase III in Figure 4.2) and the epoxy starts cross-linking. During cross-linking, the disoriented epoxy molecules start to orient themselves and form polymeric chains. During such orientation, the mobility of ions in the liquid epoxy gives rise to new conductivity and decreases the overall electrical resistivity (initial part of phase IV in Figure 4.2). After proper orientations, gelation (solidification) of epoxy begins followed by a chemical cure shrinkage (phase IV in Figure 4.2). A shrinkage of up to 7% was noted in thermoset polymers [117,118]. Such shrinkage decreases the CNT-CNT contact junction distance, causing an overall decrease in the resistance of the CNTs network, reaching afterward a steady-state value (phase V in Figure 4.2).

The “infiltration – shrinkage” mechanism for change of resistivity in a cure cycle was proposed in Ref. [48] for aligned MWCNTs nanocomposite. We have observed the same behavior for randomly oriented SWCNTs. A detailed analysis of temperature effect on electrical conductivity of the CNTs network (without epoxy) was presented in Ref. [119].

4.5 Conclusion

The inclusion of as low as 0.6 wt% of one-dimensional filler like SWCNTs converted the non-conductive epoxy into a conductive nanocomposite. This new functional property has been successfully used for monitoring the cure status of composite materials using a thermoset polymer as a matrix. The variation in the electrical resistivity of the nanocomposite with time has been used as a sensor parameter not only to determine but also to monitor the curing process. This behavior of the nanocomposite can be used as a sensor to determine and continuously monitor the curing process of thermoset matrix materials, leading to improvement and advancement in the quality control and productivity of composite manufacturing.

4.6 Publications

The research findings were presented as an oral presentation during the IEEE NANO 2023 conference and published as a conference proceeding in IEEE Xplore journal as,

B. Mahato, S.V. Lomov, S.G. Abaimov, Quality Control and Cure Status Monitoring Sensor based on Industrial Carbon Nanotube Masterbatch, IEEE Xplore, 2023, doi.org/10.1109/NANO58406.2023.10231314.

The authors' contributions to this conference presentation and proceeding article are as follows: Conceptualization, B.M., S.V.L and S.G.A.; methodology, B.M., S.V.L and S.G.A.; software, B.M.; validation, B.M.; formal analysis, B.M., S.V.L and S.G.A.; investigation, B.M.; resources, B.M., S.V.L and S.G.A.; data curation, B.M.; writing–original draft preparation, B.M.; writing–review and editing, B.M., S.V.L, and S.G.A.; visualization, B.M.; supervision, S.G.A.; project administration, S.G.A.; funding acquisition, S.G.A.; corresponding author, B.M.; presentation, B.M.

It was also submitted as a patent for consideration in Russia. Application for Russian patent was considered, and patent was granted and published as,

B. Mahato, S.G. Abaimov, S.V. Lomov, Method for Determining or Monitoring the Degree of Hardening of Thermosetting Polymers, patent no. RU 2 796 241 C1, granted on May 18, 2023.

The authors' contributions to this patent publication are as follows: Conceptualization, B.M., S.V.L and S.G.A.; methodology, B.M., S.V.L and S.G.A.; software, B.M.; validation, B.M.; formal analysis, B.M., S.V.L and S.G.A.; investigation, B.M.; resources, B.M., S.V.L and S.G.A.; data curation, B.M.; writing–original draft preparation, B.M., S.V.L. and S.G.A.; writing–review and editing, B.M. and S.G.A.; visualization, B.M.; supervision, S.G.A.; project administration, S.G.A.; funding acquisition, S.G.A.

It was also submitted as a patent for consideration in China. Application for Russian patent was considered, and patent was granted and published as,

B. Mahato, S.G. Abaimov, S.V. Lomov, The Method for Determining or Monitoring the Degree of Cure of Thermoset Polymers, patent no. CN 117233243 A, published on December 15, 2023.

The authors' contributions to this patent application submission are as follows: Conceptualization, B.M., S.V.L and S.G.A.; methodology, B.M., S.V.L and S.G.A.; software, B.M.; validation, B.M.; formal analysis, B.M., S.V.L and S.G.A.; investigation, B.M.; resources, B.M., S.V.L and S.G.A.; data curation, B.M.; writing–original draft preparation, B.M., S.V.L. and S.G.A; writing–review and editing, B.M. and S.G.A.; visualization, B.M.; supervision, S.G.A.; project administration, S.G.A.; funding acquisition, S.G.A.

Chapter 5

Conclusion and Outlook

FRP composite laminates are widely used in various applications where high strength at a low weight is desired. These laminates offer high in-plane mechanical properties, determined by the fibers. However, they suffer from poor out-of-plane properties. It makes a composite laminate highly susceptible to failure by out-of-plane loads, leading to delamination. In this research, a nanoscale modification of the interlaminar region is explored, which not only improves the out-of-plane property but also makes the laminate electrically conductive providing an opportunity for application for structural health monitoring. Such multifunctionality is highly desired as it adds extra benefits apart from its primary function for the same or slight increase in initial cost.

This research studied and demonstrated a method for introduction of industrially available CNTs masterbatch in the composite laminate for making them multifunctional. The multifunctionality of the laminate has been demonstrated as reinforcing CNTs introduced a hierarchical toughening mechanism, improved the electrical conductivity of laminate, and made it suitable for damage detection and monitoring in view of structural health monitoring applications. Similarly, along with the primary toughening mechanism of fiber bridging effect in unidirectional composite laminates, CNTs add micro- and nanoscale toughening, creating a hierarchical toughening. Such hierarchical toughening provides damage dissipation, leading to high fracture toughness. The primary advantage of this method is that it can be scaled to any large composite structure as the CNT masterbatches are available at an industrial scale in dispersed form, giving advantages over the dry form of CNTs.

Along with this, a new method of cure monitoring has been developed and demonstrated using the cure monitoring capability of CNTs nanocomposite. Compared to the conventional methods, which were either sampling where the samples were taken destructively from the main structure for testing or existing *in-situ* methods which come at the expense of a mismatch of diameter of reinforcing fibers and the sensor elements, creating a weak spot for future damages initiations, needs expensive equipment, and highly trained expert. This new CNTs nanocomposite-based sensor and method is developed and presented as an alternative and promising technique to create a low-cost, efficient, easy-to-operate, interpret, suitable for continuous and *in-situ* monitoring sensor system for monitoring the degree of cure of thermoset matrices. The methodology has been patented and is ready for commercialization.

5.1 Outlook

This research successfully demonstrated the production of the PAN veil with addition of CNTs. Being within the limitation of collaboration, all the tests possible for measuring the electrical conductivity were performed. However, the desired electrical conductivity of PAN veil modified with CNTs was not achieved. It is advised to revisit the manufacturing process of PAN veil with CNTs to future researchers with access to the electrospinning setup.

Fracture toughness improvement for Mode I has been demonstrated along with the capability of structural health monitoring, which could be further extended for Mode II fracture toughness test. Future researchers are advised to conduct the Mode II test with the capability of structural health monitoring. Mode II test demonstrating improvement in fracture toughness has been reported for various methods of introducing CNTs in the laminate; however, Mode II test demonstrating the structural health monitoring capability to the best of our knowledge has not been reported so far in literature and would be interesting. Similarly, the fatigue test under Mode I fracture toughness test with a possibility of structural health monitoring would be another interesting extended application that requires further investigations.

In the manufacturing process of CNTs mixture for interleave or for nanocomposite for cure monitoring sensor, it can be noted that the degassing steps are multi-step, long, and important. It was because degassing helped to remove the trapped air bubbles from the materials during processing and improve the electrical conductivity of resulting nanocomposite. There is a need for the development of methods that could quantify and measure such air bubbles in nanocomposite. X-ray computed tomography image-based modeling as listed here in studies 2, 3, and 4 has demonstrated usefulness for microscale study and could be extended for the above-mentioned nanocomposites problems.

Similarly, design of composite laminates with thinner interleaves (than as demonstrated herein in Section 3.4.2) manufactured from CNTs masterbatch and their effect on fracture toughness could also be the topic of further investigation.

Bibliography

[1] Curtis, P. T.: Multifunctional polymer composites. Advanced Performance Materials, **3**, 279–293 (1996). http://doi:10.1007/BF00136792.

[2] Malakooti, M. H.; Patterson, B. A.; Hwang, H.-S.; Sodano, H. A.: Development of multifunctional fiber reinforced polymer composites through ZnO nanowire arrays. In *Behavior and Mechanics of Multifunctional Materials and Composites 2016*; Goulbourne, N. C., Ed.; (2016); Vol. 9800, p. 98000L.

[3] Ashrafi, B.; Jakubinek, M. B.; Martinez-Rubi, Y.; Rahmat, M.; Djokic, D.; Laqua, K.; Park, D.; Kim, K. S.; Simard, B.; Yousefpour, A.: Multifunctional fiber reinforced polymer composites using carbon and boron nitride nanotubes. Acta Astronautica, **141**, 57–63 (2017). http://doi:10.1016/j.actaastro.2017.09.023.

[4] Forintos, N.; Czigany, T.: Multifunctional application of carbon fiber reinforced polymer composites: Electrical properties of the reinforcing carbon fibers – A short review. *Compos. Part B Eng.* (2019), *162*, 331–343.

[5] Luan, C.; Movva, S.; Wang, K.; Yao, X.; Zhang, C.; Wang, B.: Towards next-generation fiber-reinforced polymer composites: a perspective on multifunctionality. Functional Composites and Structures, **1**, 042002 (2019). http://doi:10.1088/2631-6331/ab47f9.

[6] A. Butt, H.; V. Rogozhkin, G.; Starkov, A.; V. Krasnikov, D.; G. Nasibulin, A.: Multifunctional Carbon Nanotube Reinforced Polymer/Fiber Composites: Fiber-Based Integration and Properties. In *Next Generation Fiber-Reinforced Composites - New Insights*; IntechOpen, (2023); Vol. 11, p. 13 ISBN 0000957720.

[7] Wang, Z.; Hu, T.; Liang, R.; Wei, M.: Application of Zero-Dimensional Nanomaterials in Biosensing. Frontiers in Chemistry, **8**, 1–19 (2020). http://doi:10.3389/fchem.2020.00320.

[8] Talebian, S.; Rodrigues, T.; das Neves, J.; Sarmento, B.; Langer, R.; Conde, J.: Facts and Figures on Materials Science and Nanotechnology Progress and Investment. ACS Nano, **15**, 15940–15952 (2021). http://doi:10.1021/acsnano.1c03992.

[9] Byakodi, M.; Shrikrishna, N. S.; Sharma, R.; Bhansali, S.; Mishra, Y.; Kaushik, A.; Gandhi, S.: Emerging 0D, 1D, 2D, and 3D nanostructures for efficient point-of-care biosensing. Biosensors and Bioelectronics: X, **12**, 100284 (2022). http://doi:10.1016/j.biosx.2022.100284.

[10] Paras; Yadav, K.; Kumar, P.; Teja, D. R.; Chakraborty, S.; Chakraborty, M.; Mohapatra, S. S.; Sahoo, A.; Chou, M. M. C.; Liang, C.-T.; Hang, D.-R.: A Review on Low-Dimensional Nanomaterials: Nanofabrication, Characterization and Applications. Nanomaterials, **13**, 160 (2022). http://doi:10.3390/nano13010160.

[11] Siqueira, J. R.; Oliveira, O. N.: Carbon-Based Nanomaterials. In *Nanostructures*; Elsevier, (2017); pp. 233–249 ISBN 9780323497831.

[12] Díez-Pascual, A. M.: Carbon-Based Nanomaterials 3.0. International Journal of Molecular Sciences, **23**, 9321 (2022). http://doi:10.3390/ijms23169321.

[13] Wang, Y.; Weng, G. J.: Electrical Conductivity of Carbon Nanotube- and Graphene-Based Nanocomposites. In *Micromechanics and Nanomechanics of Composite Solids*; Meguid, S. A., Weng, G. J., Eds.; Springer International Publishing: Cham, (2018); pp. 123–156 ISBN 978-3-319-52793-2.

[14] Butt, H. A.; Lomov, S. V.; Akhatov, I. S.; Abaimov, S. G.: Self-diagnostic carbon nanocomposites manufactured from industrial epoxy masterbatches. Composite Structures, **259**, 113244 (2021). http://doi:10.1016/j.compstruct.2020.113244.

[15] Chermoshentseva, A. S.; Pokrovskiy, A. M.; Bokhoeva, L. A.: The behavior of delaminations in composite materials - experimental results. IOP Conference Series: Materials Science and Engineering, **116**, 012005 (2016). http://doi:10.1088/1757-899X/116/1/012005.

[16] Sun, J.; Ma, Z.; Zhang, Z.; Weng, F.; Chen, R.: The delamination of carbon fiber reinforced composites during cutting by flexible linear shaped charge. Journal of Mechanical Science and Technology, **34**, 1515–1522 (2020). http://doi:10.1007/s12206-020-0313-2.

[17] Palazzetti, R.; Zucchelli, A.: Electrospun nanofibers as reinforcement for composite laminates materials – A review. Composite Structures, **182**, 711–727 (2017). http://doi:10.1016/j.compstruct.2017.09.021.

[18] Li, J.; Wang, J.; Zhang, L.; Huang, X.; Yu, Y.: Study on the Effect of Different Delamination Defects on Buckling Behavior of Spar Cap in Wind Turbine Blade. Advances in Materials Science and Engineering, **2020**, 1–10 (2020). http://doi:10.1155/2020/6979636.

[19] Zhang, Y.; Huang, K.; Sun, R.; Liao, F.; Guo, L.; Zhang, L.: Effect of embedded delamination on the compression performance of carbon fiber reinforced composites. Composite Structures, **281**, 1–13 (2022). http://doi:10.1016/j.compstruct.2021.115063.

[20] Riccio, A.; Castaldo, R.; Palumbo, C.; Russo, A.: Delamination Effect on the Buckling Behaviour of Carbon–Epoxy Composite Typical Aeronautical Panels. Applied Sciences, **13**, 4358 (2023). http://doi:10.3390/app13074358.

[21] Mouritz, A. P.: Review of z-pinned composite laminates. Composites Part A: Applied Science and Manufacturing, **38**, 2383–2397 (2007). http://doi:10.1016/j.compositesa.2007.08.016.

[22] Mouritz, A. P.; Cox, B. N.: A mechanistic interpretation of the comparative in-plane mechanical properties of 3D woven, stitched and pinned composites. Composites Part A: Applied Science and Manufacturing, **41**, 709–728 (2010). http://doi:10.1016/j.compositesa.2010.02.001.

[23] Swolfs, Y.; Gorbatikh, L.; Verpoest, I.: Fibre hybridisation in polymer composites: A review. Composites Part A: Applied Science and Manufacturing, **67**, 181–200 (2014). http://doi:10.1016/j.compositesa.2014.08.027.

[24] Wang, Y.; Wang, Z.; Zhu, L.: A Short Review of Recent Progress in Improving the Fracture Toughness of FRP Composites Using Short Fibers. Sustainability, **14**, 6215 (2022). http://doi:10.3390/su14106215.

[25] Lomov, S. V.; Molnár, K.: Compressibility of carbon fabrics with needleless electrospun PAN nanofibrous interleaves. Express Polymer Letters, **10**, 25–35

(2016). http://doi:10.3144/expresspolymlett.2016.4.
[26] Beckermann, G. W.; Pickering, K. L.: Mode I and Mode II interlaminar fracture toughness of composite laminates interleaved with electrospun nanofibre veils. Composites Part A: Applied Science and Manufacturing, **72**, 11–21 (2015). http://doi:10.1016/j.compositesa.2015.01.028.
[27] Meireman, T.; Daelemans, L.; Rijckaert, S.; Rahier, H.; Van Paepegem, W.; De Clerck, K.: Delamination resistant composites by interleaving bio-based long-chain polyamide nanofibers through optimal control of fiber diameter and fiber morphology. Composites Science and Technology, **193**, 108126 (2020). http://doi:10.1016/j.compscitech.2020.108126.
[28] García-Rodríguez, S. M.; Costa, J.; Rankin, K. E.; Boardman, R. P.; Singery, V.; Mayugo, J. A.: Interleaving light veils to minimise the trade-off between mode-I interlaminar fracture toughness and in-plane properties. Composites Part A: Applied Science and Manufacturing, **128**, 105659 (2020). http://doi:10.1016/j.compositesa.2019.105659.
[29] Quan, D.; Bologna, F.; Scarselli, G.; Ivankovic, A.; Murphy, N.: Interlaminar fracture toughness of aerospace-grade carbon fibre reinforced plastics interleaved with thermoplastic veils. Composites Part A: Applied Science and Manufacturing, **128**, 105642 (2020). http://doi:10.1016/j.compositesa.2019.105642.
[30] Garcia, E. J.; Wardle, B. L.; John Hart, A.: Joining prepreg composite interfaces with aligned carbon nanotubes. Composites Part A: Applied Science and Manufacturing, **39**, 1065–1070 (2008). http://doi:10.1016/j.compositesa.2008.03.011.
[31] Shirodkar, N.; Cheng, S.; Seidel, G. D.: Enhancement of Mode I fracture toughness properties of epoxy reinforced with graphene nanoplatelets and carbon nanotubes. Composites Part B: Engineering, **224**, 109177 (2021). http://doi:10.1016/j.compositesb.2021.109177.
[32] Zeng, Y.; Liu, H.-Y.; Mai, Y.-W.; Du, X.-S.: Improving interlaminar fracture toughness of carbon fibre/epoxy laminates by incorporation of nano-particles. Composites Part B: Engineering, **43**, 90–94 (2012). http://doi:10.1016/j.compositesb.2011.04.036.
[33] Ning, N.; Wang, M.; Zhou, G.; Qiu, Y.; Wei, Y.: Effect of polymer nanoparticle morphology on fracture toughness enhancement of carbon fiber reinforced epoxy composites. Composites Part B: Engineering, **234**, 109749 (2022). http://doi:10.1016/j.compositesb.2022.109749.
[34] Sun, J.; Zhai, P.; Chen, Y.; Zhao, J.; Huang, Z.: Hierarchical toughening of laminated nanocomposites with three-dimensional graphene/carbon nanotube/SiC nanowire. Materials Today Nano, **18**, 100180 (2022). http://doi:10.1016/j.mtnano.2022.100180.
[35] Kim, J.-W.; Gardner, J. M.; Sauti, G.; Wincheski, R. A.; Jensen, B. D.; Wise, K. E.; Siochi, E. J.: Multi-scale hierarchical carbon nanotube fiber reinforced composites towards enhancement of axial/transverse strength and fracture toughness. Composites Part A: Applied Science and Manufacturing, **167**, 107449 (2023). http://doi:10.1016/j.compositesa.2023.107449.

[36] Quaresimin, M.; Schulte, K.; Zappalorto, M.; Chandrasekaran, S.: Toughening mechanisms in polymer nanocomposites: From experiments to modelling. Composites Science and Technology, **123**, 187–204 (2016). http://doi:10.1016/j.compscitech.2015.11.027.

[37] Gnidakouong, J. R. N.; Roh, H. D.; Kim, J.-H.; Park, Y.-B.: In situ assessment of carbon nanotube flow and filtration monitoring through glass fabric using electrical resistance measurement. Composites Part A: Applied Science and Manufacturing, **90**, 137–146 (2016). http://doi:10.1016/j.compositesa.2016.07.005.

[38] Park, S. J.; Moyer-Vanderburgh, K.; Buchsbaum, S. F.; Meshot, E. R.; Jue, M. L.; Wu, K. J.; Fornasiero, F.: Synthesis of wafer-scale SWCNT forests with remarkably invariant structural properties in a bulk-diffusion-controlled kinetic regime. Carbon, **201**, 745–755 (2023). http://doi:10.1016/j.carbon.2022.09.068.

[39] Zhang, C.; Wu, L.; de Perrot, M.; Zhao, X.: Carbon Nanotubes: A Summary of Beneficial and Dangerous Aspects of an Increasingly Popular Group of Nanomaterials. Frontiers in Oncology, **11**, 1–12 (2021). http://doi:10.3389/fonc.2021.693814.

[40] Wicks, S. S.; Wang, W.; Williams, M. R.; Wardle, B. L.: Multi-scale interlaminar fracture mechanisms in woven composite laminates reinforced with aligned carbon nanotubes. Composites Science and Technology, **100**, 128–135 (2014). http://doi:10.1016/j.compscitech.2014.06.003.

[41] Burkov, M.; Eremin, A.: Evaluation of fracture toughness of hybrid CNT/CFRP composites. Mechanics of Advanced Materials and Structures, **0**, 1–10 (2022). http://doi:10.1080/15376494.2022.2064569.

[42] Zhang, H.; Liu, Y.; Kuwata, M.; Bilotti, E.; Peijs, T.: Improved fracture toughness and integrated damage sensing capability by spray coated CNTs on carbon fibre prepreg. Composites Part A: Applied Science and Manufacturing, **70**, 102–110 (2015). http://doi:10.1016/j.compositesa.2014.11.029.

[43] Wan, Y.; Yang, H.; Tian, Z.; Yang, B.; Xian, G.; Weng, J.; Chen, S.; Ding, X.; Luo, W.: Mode I interlaminar crack length prediction by the resistance signal of the integrated MWCNT sensor in WGF/epoxy composites during DCB test. Journal of Materials Research and Technology, **9**, 5922–5933 (2020). http://doi:10.1016/j.jmrt.2020.03.119.

[44] Tzounis, L.; Zappalorto, M.; Panozzo, F.; Tsirka, K.; Maragoni, L.; Paipetis, A. S.; Quaresimin, M.: Highly conductive ultra-sensitive SWCNT-coated glass fiber reinforcements for laminate composites structural health monitoring. Composites Part B: Engineering, **169**, 37–44 (2019). http://doi:10.1016/j.compositesb.2019.03.070.

[45] Liu, H.; Qu, P.; Yu, S.; Xu, Y.; Jia, Y.: Low-cost carbon black-loaded functional films for interlaminar toughening and in-situ delamination monitoring of carbon fiber/epoxy composites. Journal of Applied Polymer Science, **139**, 52170 (2022). http://doi:10.1002/app.52170.

[46] Lionetto, F.; Maffezzoli, A.: Monitoring the Cure State of Thermosetting Resins by Ultrasound. Materials, **6**, 3783–3804 (2013). http://doi:10.3390/ma6093783.

[47] Hudson, T. B.; Yuan, F.-G.: Automated In-Process Cure Monitoring of Composite Laminates Using a Guided Wave-Based System With High-Temperature Piezoelectric Transducers. Journal of Nondestructive Evaluation, Diagnostics and Prognostics of Engineering Systems, **1**, 021008-021008–8 (2018). http://doi:10.1115/1.4039230.
[48] Lee, J.; Wardle, B. L.: Nanoengineered in situ cure status monitoring technique based on carbon nanotube network. AIAA Scitech 2019 Forum, , 1–14 (2019). http://doi:10.2514/6.2019-1199.
[49] Mitchell, G. R.: *Electrospinning: Principles, Practice and Possibilities Edited*; Tang, B. Z., Abd-El-Aziz, A. S., Craig, S., Dong, J., Masuda, T., Weder, C., Eds.; The Royal Society of Chemistry, Thomas Graham House, Science Park, Milton Road, Cambridge CB4 0WF, UK; ISBN 978-1849735568.
[50] Molnar, K.; Nagy, Z. K.: Corona-electrospinning: Needleless method for high-throughput continuous nanofiber production. European Polymer Journal, **74**, 279–286 (2016). http://doi:10.1016/j.eurpolymj.2015.11.028.
[51] Molnár, K.; Vas, L. M.: Electrospun Composite Nanofibers and Polymer Composites. In *Synthetic Polymer-Polymer Composites*; Carl Hanser Verlag GmbH & Co. KG: München, (2012); pp. 301–349.
[52] ASTM D5528-01: Standard test method for mode I interlaminar fracture toughness of unidirectional fiber-reinforced polymer matrix composites. American Standard of Testing Methods, **03**, 1–12 (2014). http://doi:10.1520/D5528-13.
[53] ASTM D7905: Standard test method for determination of the mode II interlaminar fracture toughness of unidirectional fiber-reinforced polymer matrix composites. Astm, , 1–18 (2014). http://doi:10.1520/D7905.
[54] Tzetzis, D.; Hogg, P. J.; Jogia, M.: Double cantilever beam Mode-I testing for vacuum infused repairs of GFRP. Journal of Adhesion Science and Technology, **17**, 309–328 (2003). http://doi:10.1163/156856103762864642.
[55] Tzetzis, D.; Hogg, P. J.: Bondline toughening of vacuum infused composite repairs. Composites Part A: Applied Science and Manufacturing, **37**, 1239–1251 (2006). http://doi:10.1016/j.compositesa.2005.09.008.
[56] Kuwata, M.; Hogg, P. J.: Interlaminar toughness of interleaved CFRP using non-woven veils: Part 2. Mode-II testing. Composites Part A: Applied Science and Manufacturing, **42**, 1560–1570 (2011). http://doi:10.1016/j.compositesa.2011.07.017.
[57] Kuwata, M.; Hogg, P. J.: Interlaminar toughness of interleaved CFRP using non-woven veils: Part 1. Mode-I testing. Composites Part A: Applied Science and Manufacturing, **42**, 1551–1559 (2011). http://doi:10.1016/j.compositesa.2011.07.016.
[58] Quan, D.; Mischo, C.; Li, X.; Scarselli, G.; Ivanković, A.; Murphy, N.: Improving the electrical conductivity and fracture toughness of carbon fibre/epoxy composites by interleaving MWCNT-doped thermoplastic veils. Composites Science and Technology, **182**, 107775 (2019). http://doi:10.1016/j.compscitech.2019.107775.
[59] Quan, D.; Bologna, F.; Scarselli, G.; Ivanković, A.; Murphy, N.: Mode-II fracture

behaviour of aerospace-grade carbon fibre/epoxy composites interleaved with thermoplastic veils. Composites Science and Technology, **191**, 108065 (2020). http://doi:10.1016/j.compscitech.2020.108065.

[60] Fitzmaurice, K.; Ray, D.; McCarthy, M. A.: PET interleaving veils for improved fracture toughness of glass fibre/low-styrene-emission unsaturated polyester resin composites. Journal of Applied Polymer Science, **133**, 1–8 (2016). http://doi:10.1002/app.42877.

[61] Del Saz-Orozco, B.; Ray, D.; Stanley, W. F.: Effect of thermoplastic veils on interlaminar fracture toughness of a glass fiber/vinyl ester composite. Polymer Composites, **38**, 2501–2508 (2017). http://doi:10.1002/pc.23840.

[62] Quan, D.; Mischo, C.; Binsfeld, L.; Ivankovic, A.; Murphy, N.: Fracture behaviour of carbon fibre/epoxy composites interleaved by MWCNT- and graphene nanoplatelet-doped thermoplastic veils. Composite Structures, **235**, 111767 (2020). http://doi:10.1016/j.compstruct.2019.111767.

[63] Ramirez, V. A.; Hogg, P. J.; Sampson, W. W.: The influence of the nonwoven veil architectures on interlaminar fracture toughness of interleaved composites. Composites Science and Technology, **110**, 103–110 (2015). http://doi:10.1016/j.compscitech.2015.01.016.

[64] Ramji, A.; Xu, Y.; Yasaee, M.; Grasso, M.; Webb, P.: Delamination migration in CFRP laminates under mode I loading. Composites Science and Technology, **190**, 108067 (2020). http://doi:10.1016/j.compscitech.2020.108067.

[65] Saghafi, H.; Zucchelli, A.; Palazzetti, R.; Minak, G.: The effect of interleaved composite nanofibrous mats on delamination behavior of polymeric composite materials. Composite Structures, **109**, 41–47 (2014). http://doi:10.1016/j.compstruct.2013.10.039.

[66] Saghafi, H.; Palazzetti, R.; Zucchelli, A.; Minak, G.: Influence of electrospun nanofibers on the interlaminar properties of unidirectional epoxy resin/glass fiber composite laminates. Journal of Reinforced Plastics and Composites, **34**, 907–914 (2015). http://doi:10.1177/0731684415584635.

[67] Nash, N. H.; Ray, D.; Young, T. M.; Stanley, W. F.: The influence of hydrothermal conditioning on the Mode-I, thermal and flexural properties of Carbon/Benzoxazine composites with a thermoplastic toughening interlayer. Composites Part A: Applied Science and Manufacturing, **76**, 135–144 (2015). http://doi:10.1016/j.compositesa.2015.04.023.

[68] Nash, N. H.; Young, T. M.; Stanley, W. F.: The influence of a thermoplastic toughening interlayer and hydrothermal conditioning on the Mode-II interlaminar fracture toughness of Carbon/Benzoxazine composites. Composites Part A: Applied Science and Manufacturing, **81**, 111–120 (2016). http://doi:10.1016/j.compositesa.2015.11.010.

[69] Guo, M.; Yi, X.; Liu, G.; Liu, L.: Simultaneously increasing the electrical conductivity and fracture toughness of carbon-fiber composites by using silver nanowires-loaded interleaves. Composites Science and Technology, **97**, 27–33 (2014). http://doi:10.1016/j.compscitech.2014.03.020.

[70] Chen, G.; Zhang, J.; Liu, G.; Chen, P.; Guo, M.: Controlling the crack propagation

path of the veil interleaved composite by fusion-bonded dots. Polymers, **11**, 1–12 (2019). http://doi:10.3390/polym11081260.

[71] Ognibene, G.; Latteri, A.; Mannino, S.; Saitta, L.; Recca, G.; Scarpa, F.; Cicala, G.: Interlaminar Toughening of Epoxy Carbon Fiber Reinforced Laminates: Soluble Versus Non-Soluble Veils. Polymers, **11**, 1029 (2019). http://doi:10.3390/polym11061029.

[72] Pozegic, T. R.; King, S. G.; Fotouhi, M.; Stolojan, V.; Silva, S. R. P.; Hamerton, I.: Delivering interlaminar reinforcement in composites through electrospun nanofibres. Advanced Manufacturing: Polymer & Composites Science, **5**, 155–171 (2019). http://doi:10.1080/20550340.2019.1665226.

[73] Beylergil, B.; Tanoğlu, M.; Aktaş, E.: Experimental and statistical analysis of carbon fiber/epoxy composites interleaved with nylon 6,6 nonwoven fabric interlayers. Journal of Composite Materials, **54**, 4173–4184 (2020). http://doi:10.1177/0021998320927740.

[74] Beylergil, B.; Tanoğlu, M.; Aktaş, E.: Effect of polyamide-6,6 (PA 66) nonwoven veils on the mechanical performance of carbon fiber/epoxy composites. Composite Structures, **194**, 21–35 (2018). http://doi:10.1016/j.compstruct.2018.03.097.

[75] Beylergil, B.; Tanoğlu, M.; Aktaş, E.: Enhancement of interlaminar fracture toughness of carbon fiber-epoxy composites using polyamide-6,6 electrospun nanofibers. Journal of Applied Polymer Science, **134**, 45244 (2017). http://doi:10.1002/app.45244.

[76] Alessi, S.; Di Filippo, M.; Dispenza, C.; Focarete, M. L.; Gualandi, C.; Palazzetti, R.; Pitarresi, G.; Zucchelli, A.: Effects of Nylon 6,6 nanofibrous mats on thermal properties and delamination behavior of high performance CFRP laminates. Polymer Composites, **36**, 1303–1313 (2015). http://doi:10.1002/pc.23035.

[77] Barjasteh, E.; Sutanto, C.; Reddy, T.; Vinh, J.: A graphene/graphite-based conductive polyamide 12 interlayer for increasing the fracture toughness and conductivity of carbon-fiber composites. Journal of Composite Materials, **51**, 2879–2887 (2017). http://doi:10.1177/0021998317705707.

[78] Monteserín, C.; Blanco, M.; Murillo, N.; Pérez-Márquez, A.; Maudes, J.; Gayoso, J.; Laza, J. M.; Hernáez, E.; Aranzabe, E.; Vilas, J. L.: Novel antibacterial and toughened carbon-fibre/epoxy composites by the incorporation of TiO2 nanoparticles modified electrospun nanofibre veils. Polymers, **11** (2019). http://doi:10.3390/polym11091524.

[79] Monteserín, C.; Blanco, M.; Murillo, N.; Pérez-Márquez, A.; Maudes, J.; Gayoso, J.; Laza, J.; Aranzabe, E.; Vilas, J.: Effect of Different Types of Electrospun Polyamide 6 Nanofibres on the Mechanical Properties of Carbon Fibre/Epoxy Composites. Polymers, **10**, 1190 (2018). http://doi:10.3390/polym10111190.

[80] Daelemans, L.; van der Heijden, S.; De Baere, I.; Rahier, H.; Van Paepegem, W.; De Clerck, K.: Nanofibre bridging as a toughening mechanism in carbon/epoxy composite laminates interleaved with electrospun polyamide nanofibrous veils. Composites Science and Technology, **117**, 244–256 (2015). http://doi:10.1016/j.compscitech.2015.06.021.

[81] Daelemans, L.; van der Heijden, S.; De Baere, I.; Rahier, H.; Van Paepegem, W.;

De Clerck, K.: Using aligned nanofibres for identifying the toughening micromechanisms in nanofibre interleaved laminates. Composites Science and Technology, **124**, 17–26 (2016). http://doi:10.1016/j.compscitech.2015.11.021.

[82] Daelemans, L.; Van Der Heijden, S.; De Baere, I.; Rahier, H.; Van Paepegem, W.; De Clerck, K.: Damage-Resistant Composites Using Electrospun Nanofibers: A Multiscale Analysis of the Toughening Mechanisms. ACS Applied Materials and Interfaces, **8**, 11806–11818 (2016). http://doi:10.1021/acsami.6b02247.

[83] De Schoenmaker, B.; Van der Heijden, S.; De Baere, I.; Van Paepegem, W.; De Clerck, K.: Effect of electrospun polyamide 6 nanofibres on the mechanical properties of a glass fibre/epoxy composite. Polymer Testing, **32**, 1495–1501 (2013). http://doi:10.1016/j.polymertesting.2013.09.015.

[84] O'Donovan, K.; Ray, D.; McCarthy, M. A.: Toughening effects of interleaved nylon veils on glass fabric/low-styrene-emission unsaturated polyester resin composites. Journal of Applied Polymer Science, **132**, 1–9 (2015). http://doi:10.1002/app.41462.

[85] Hamer, S.; Leibovich, H.; Green, A.; Intrater, R.; Avrahami, R.; Zussman, E.; Siegmann, A.; Sherman, D.: Mode I interlaminar fracture toughness of Nylon 66 nanofibrilmat interleaved carbon/epoxy laminates. Polymer Composites, **32**, 1781–1789 (2011). http://doi:10.1002/pc.21210.

[86] Guo, M.; Yi, X.; Rudd, C.; Liu, X.: Preparation of highly electrically conductive carbon-fiber composites with high interlaminar fracture toughness by using silver-plated interleaves. Composites Science and Technology, **176**, 29–36 (2019). http://doi:10.1016/j.compscitech.2019.03.014.

[87] VanderVennet, J. A.; Duenas, T.; Dzenis, Y.; Peterson, C. T.; Bakis, C. E.; Carter, D.; Roberts, J. K.: Fracture toughness characterization of nanoreinforced carbon-fiber composite materials for damage mitigation. In *Behavior and Mechanics of Multifunctional Materials and Composites 2011*; Ounaies, Z., Seelecke, S. S., Eds.; (2011); Vol. 7978, p. 797823.

[88] Zhang, J.; Yang, T.; Lin, T.; Wang, C. H.: Phase morphology of nanofibre interlayers: Critical factor for toughening carbon/epoxy composites. Composites Science and Technology, **72**, 256–262 (2012). http://doi:10.1016/j.compscitech.2011.11.010.

[89] Chiu, K. R.; Duenas, T.; Dzenis, Y.; Kaser, J.; Bakis, C. E.; Roberts, J. K.; Carter, D.: Comparative study of nanomaterials for interlaminar reinforcement of fiber-composite panels. In *Behavior and Mechanics of Multifunctional Materials and Composites 2013*; Goulbourne, N. C., Naguib, H. E., Eds.; (2013); Vol. 8689, p. 86891D.

[90] Razavi, S. M. J.; Neisiany, R. E.; Khorasani, S. N.; Ramakrishna, S.; Berto, F.: Effect of neat and reinforced polyacrylonitrile nanofibers incorporation on interlaminar fracture toughness of carbon/epoxy composite. Theoretical and Applied Mechanics Letters, **8**, 126–131 (2018). http://doi:10.1016/j.taml.2018.02.008.

[91] Molnár, K.; Szebényi, G.; Szolnoki, B.; Marosi, G.; Vas, L. M.; Toldy, A.: Enhanced conductivity composites for aircraft applications: Carbon nanotube

inclusion both in epoxy matrix and in carbonized electrospun nanofibers. Polymers for Advanced Technologies, **25**, 981–988 (2014). http://doi:10.1002/pat.3339.

[92] Eskizeybek, V.; Yar, A.; Avcı, A.: CNT-PAN hybrid nanofibrous mat interleaved carbon/epoxy laminates with improved Mode I interlaminar fracture toughness. Composites Science and Technology, **157**, 30–39 (2018). http://doi:10.1016/j.compscitech.2018.01.021.

[93] Cohades, A.; Daelemans, L.; Ward, C.; Meireman, T.; Van Paepegem, W.; De Clerck, K.; Michaud, V.: Size limitations on achieving tough and healable fibre reinforced composites through the use of thermoplastic nanofibres. Composites Part A: Applied Science and Manufacturing, **112**, 485–495 (2018). http://doi:10.1016/j.compositesa.2018.07.002.

[94] van der Heijden, S.; Daelemans, L.; De Schoenmaker, B.; De Baere, I.; Rahier, H.; Van Paepegem, W.; De Clerck, K.: Interlaminar toughening of resin transfer moulded glass fibre epoxy laminates by polycaprolactone electrospun nanofibres. Composites Science and Technology, **104**, 66–73 (2014). http://doi:10.1016/j.compscitech.2014.09.005.

[95] Bakis, G.; Wendel, J.-F.; Zeiler, R.; Aksit, A.; Häublein, M.; Demleitner, M.; Benra, J.; Forero, S.; Schütz, W.; Altstädt, V.: Mechanical Properties of the Carbon Nanotube Modified Epoxy–Carbon Fiber Unidirectional Prepreg Laminates. Polymers, **13**, 770 (2021). http://doi:10.3390/polym13050770.

[96] Borowski, E.; Soliman, E.; Kandil, U.; Taha, M.: Interlaminar Fracture Toughness of CFRP Laminates Incorporating Multi-Walled Carbon Nanotubes. Polymers, **7**, 1020–1045 (2015). http://doi:10.3390/polym7061020.

[97] Kumar, M.; Kumar, P.; Bhadauria, S. S.: Experimental characterization and numerical study on the interlaminar fracture toughness of carbon fibre reinforced polymer laminates reinforced with carbon nanotubes. Materialwissenschaft und Werkstofftechnik, **53**, 1561–1574 (2022). http://doi:10.1002/mawe.202200115.

[98] Li, H.; Xu, X.; Yu, Y.; Qu, S.; Chen, T.; Yao, M.; Lyu, W.: Aligned carbon nanotube composite belts stitching of laminated composites for enhanced fracture toughness and enriched functionalities. Polymer Composites, **44**, 823–832 (2023). http://doi:10.1002/pc.27134.

[99] Mohd Sabri, F. N. A.; Zakaria, M. R.; Md Akil, H.; Abidin, M. S. Z.; Ab Rahman, A. A.; Omar, M. F.: Interlaminar fracture toughness properties of hybrid glass fiber-reinforced composite interlayered with carbon nanotube using electrospray deposition. Nanotechnology Reviews, **10**, 1766–1775 (2021). http://doi:10.1515/ntrev-2021-0103.

[100] Ouyang, Q.; Liu, L.; Wu, Z.: Electrothermally Self-Healing Delamination Cracks in Carbon/Epoxy Composites Using Sandwich and Tough Carbon Nanotube/Copolymer Interleaves. Polymers, **14**, 4313 (2022). http://doi:10.3390/polym14204313.

[101] Falzon, B. G.; Hawkins, S. C.; Huynh, C. P.; Radjef, R.; Brown, C.: An investigation of Mode I and Mode II fracture toughness enhancement using aligned carbon nanotubes forests at the crack interface. Composite Structures, **106**, 65–73 (2013). http://doi:10.1016/j.compstruct.2013.05.051.

[102] Standard test method for mode I interlaminar fracture toughness of unidirectional fiber-reinforced polymer matrix composites. American Standard of Testing Methods, **03**, 1–12 (2014).

[103] Lemartinel, A.; Castro, M.; Fouche, O.; De Luca, J. C.; Feller, J. F.: Impact and strain monitoring in glass fiber reinforced epoxy laminates with embedded quantum resistive sensors (QRSs). Composites Science and Technology, **221**, 109352 (2022). http://doi:10.1016/j.compscitech.2022.109352.

[104] Sannamani, M.; Gao, J.; Chen, W. W.; Tallman, T. N.: Damage detection in non-planar carbon fiber-reinforced polymer laminates via electrical impedance tomography with surface-mounted electrodes and directional sensitivity matrices. Composites Science and Technology, **224**, 109429 (2022). http://doi:10.1016/j.compscitech.2022.109429.

[105] Lee, I. Y.; Roh, H. D.; Park, Y.-B.: Novel structural health monitoring method for CFRPs using electrical resistance based probabilistic sensing cloud. Composites Science and Technology, **213**, 108812 (2021). http://doi:10.1016/j.compscitech.2021.108812.

[106] Jafarypouria, M.; Mahato, B.; Abaimov, S. G.: Separating Curing and Temperature Effects on the Temperature Coefficient of Resistance for a Single-Walled Carbon Nanotube Nanocomposite. Polymers, **15**, 433 (2023). http://doi:10.3390/polym15020433.

[107] Shin, Y. C.; Lee, W. Il; Kim, H. S.: Mode II interlaminar fracture toughness of carbon nanotubes/epoxy film-interleaved carbon fiber composites. Composite Structures, **236**, 111808 (2020). http://doi:10.1016/j.compstruct.2019.111808.

[108] Sela, N.; Ishai, O.; Banks-Sills, L.: The effect of adhesive thickness on interlaminar fracture toughness of interleaved cfrp specimens. Composites, **20**, 257–264 (1989). http://doi:10.1016/0010-4361(89)90341-8.

[109] Zappalorto, M.; Panozzo, F.; Carraro, P. A.; Quaresimin, M.: Electrical response of a laminate with a delamination: modelling and experiments. Composites Science and Technology, **143**, 31–45 (2017). http://doi:10.1016/j.compscitech.2017.02.023.

[110] Li, Z.; Moon, K. S.; Yao, Y.; Hansen, K.; Watkins, K.; Morato, L.; Wong, C. P.: Carbon nanotube/polymer nanocomposites: Sensing the thermal aging conditions of electrical insulation components. Carbon, **65**, 71–79 (2013). http://doi:10.1016/j.carbon.2013.07.105.

[111] Li, M.; Gu, Y.; Liu, Y.; Li, Y.; Zhang, Z.: Interfacial improvement of carbon fiber/epoxy composites using a simple process for depositing commercially functionalized carbon nanotubes on the fibers. Carbon, **52**, 109–121 (2013). http://doi:10.1016/j.carbon.2012.09.011.

[112] Yourdkhani, M.; Liu, W.; Baril-Gosselin, S.; Robitaille, F.; Hubert, P.: Carbon nanotube-reinforced carbon fibre-epoxy composites manufactured by resin film infusion. Composites Science and Technology, **166**, 169–175 (2018). http://doi:10.1016/j.compscitech.2018.01.006.

[113] Vertuccio, L.; Guadagno, L.; Spinelli, G.; Lamberti, P.; Tucci, V.; Russo, S.: Piezoresistive properties of resin reinforced with carbon nanotubes for health-

monitoring of aircraft primary structures. Composites Part B: Engineering, **107**, 192–202 (2016). http://doi:10.1016/j.compositesb.2016.09.061.

[114] Lomov, S. V.; Gudkov, N. A.; Abaimov, S. G.: Uncertainties in Electric Circuit Analysis of Anisotropic Electrical Conductivity and Piezoresistivity of Carbon Nanotube Nanocomposites. Polymers, **14**, 4794 (2022). http://doi:10.3390/polym14224794.

[115] Butt, H. A.; Owais, M.; Sulimov, A.; Ostrizhiniy, D.; Lomov, S. V; Akhatov, I. S.; Abaimov, S. G.; Popov, Y. A.: CNT/Epoxy-Masterbatch Based Nanocomposites: Thermal and Electrical Properties. In *2021 IEEE 21st International Conference on Nanotechnology (NANO)*; IEEE, (2021); Vol. 2021-July, pp. 417–420.

[116] Vertuccio, L.; Russo, S.; Raimondo, M.; Lafdi, K.; Guadagno, L.: Influence of carbon nanofillers on the curing kinetics of epoxy-amine resin. RSC Advances, **5**, 90437–90450 (2015). http://doi:10.1039/C5RA14343H.

[117] Li, C.; Potter, K.; Wisnom, M. R.; Stringer, G.: In-situ measurement of chemical shrinkage of MY750 epoxy resin by a novel gravimetric method. Composites Science and Technology, **64**, 55–64 (2004). http://doi:10.1016/S0266-3538(03)00199-4.

[118] Khoun, L.; Hubert, P.: Cure shrinkage characterization of an epoxy resin system by two in situ measurement methods. Polymer Composites, **31**, 1603–1610 (2010). http://doi:10.1002/pc.20949.

[119] Lomov, S. V.; Akmanov, I. S.; Liu, Q.; Wu, Q.; Abaimov, S. G.: Negative Temperature Coefficient of Resistance in Aligned CNT Networks: Influence of the Underlying Phenomena. Polymers, **15**, 678 (2023). http://doi:10.3390/polym15030678.

Appendix

A. DSC data processing

Figure A1 shows the DSC isothermal raw and processed data along with the temperature measured during the isothermal DSC experiment. The peak and the base of the raw heat flow data are shifted such that the base of the plot is at zero to obtain the processed data. The processed data was further integrated for measured time intervals to obtain the heat of reaction of isothermal run. Figure A2 shows the DSC dynamic data and data processing applied to obtain the dynamic heat of reaction. Both heats were considered to calculate the degree of cure as detailed in Section 4.2.5.

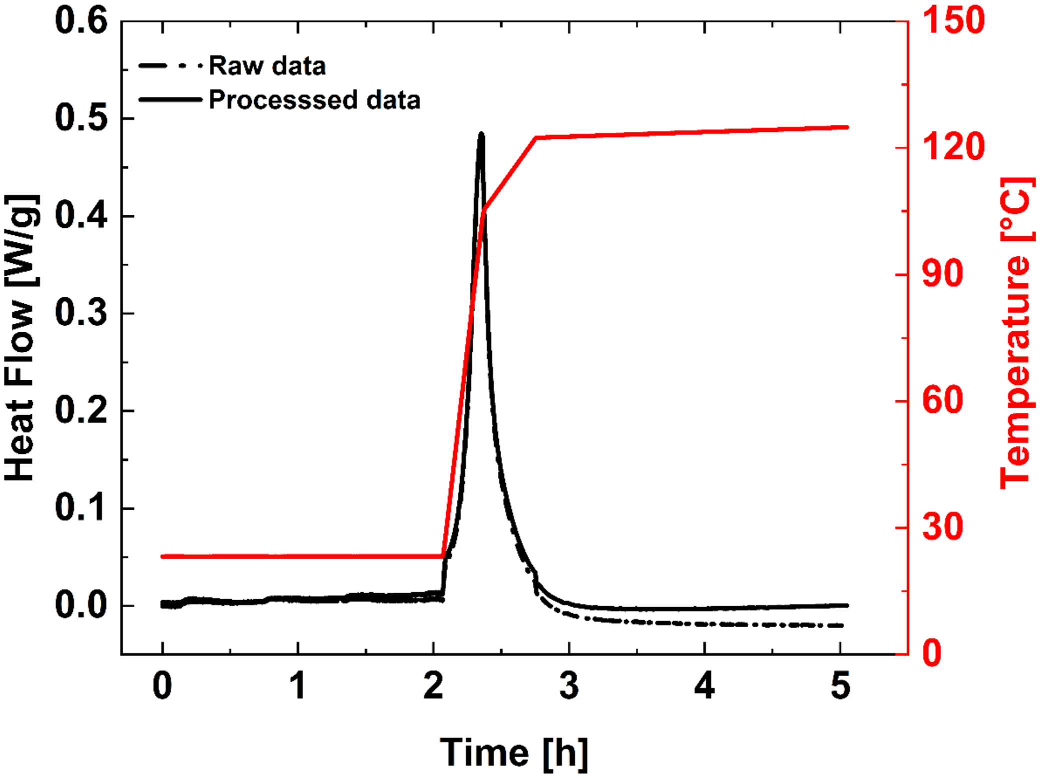

Figure A1. Isothermal DSC experimental data showing raw and processed data plots along with temperature on secondary axis.

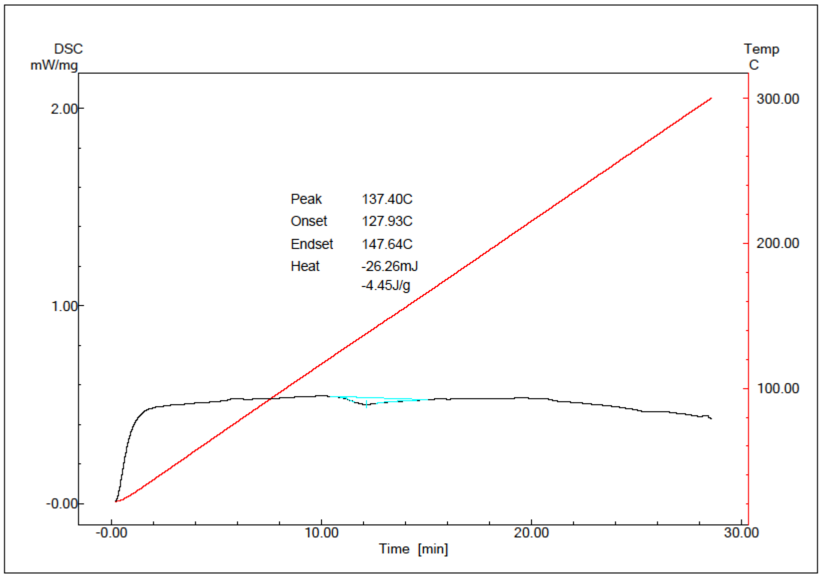

Figure A2. Dynamic DSC experimental data to obtain dynamic heat along with temperature on secondary axis.